A Computational and Experimental Analysis of Impact to Aircraft Structures

By

Pierce Kennedy, B. Eng.

This thesis is submitted to Dublin City University as the fulfilment of the requirement for the award of

Master of Engineering

Supervisor: Dr. Bryan J. MacDonald, Ph. D

School of Mechanical and Manufacturing Engineering
Dublin City University

July 2005

Declaration

I hereby certify that this material, which I now submit for assessment on the programme of study leading to the award of Master of Engineering, is entirely my own work and has not been taken from work of others save and to the extent that such work has been cited and acknowledged within the text of my work.

Signed: P. Kennedy Date: 25 Aug 2005

Pierce Kennedy

99284111

Acknowledgements

I would like to express my sincere gratitude to Dr. Bryan MacDonald for his guidance and help over the past two years. I would also like to thank my school technician, Mr. Liam Domican, and my workshop technician, Mr. Cian Merne, for their help throughout the project.

A Computational and Experimental Analysis of Impact to Aircraft Structures

Pierce Kennedy B. Eng

Abstract

The modelling and analysis of high energy impact on aircraft structures is highly complex. Traditional methods give only a limited understanding of what occurs and it is evident from the continuing problem of uncontained engine failure and other debris impact that a more accurate way of predicting the results of such impacts is needed. Finite element techniques can provide that solution.

This work attempts to model accurately impacts to existing aircraft structures. Of particular interest is the behaviour at the ballistic velocity as this is where the problem is most difficult to predict. Initially the model consisted of a simple sheet subject to impact by a cylindrical projectile. This was used to develop the modelling techniques for the more complex model. Issues that arose included the mesh density, the material model and the penalty stiffness factor used. Experimental testing was carried out using a gas fired projectile launcher to validate the finite element model. The geometry of the second model was more complex, a right angled stringer was riveted to a plate using four rivets. Two different approaches were used in modelling here, that of modelling the rivets in 3D and that of modelling the rivets using 2D approximations. Modelling the rivets in 3D proved to be impractical and of the 2D approximations the model where the rivets were not allowed to fail proved the most accurate. Experimental testing was again used for validation.

Finally a new gas powered projectile launcher was designed and built. Improvements over its predecessor included the ability to accommodate a half metre squared test plate, impact this plate anywhere on its surface and tilt the plate through 45°. Also included were modifications to the barrel so that projectiles of any shape or size up to a maximum of 50mm in diameter could be used.

Contents

Nomenclature

Symbol	Definition	Dimension
	(Used in Impact Theory)	
x	deflection in x-direction	m
y	deflection in y-direction	m
z	deflection in z-direction	m
A	Cross-sectional beam area	m^2
H	Beam height	m
B	Beam breath	m
L	Beam length	m
Q	Shear Force	N
M	Bending Moment	Nm
N	Membrane Force	N
p	external pressure load	Pa
F	Set of external loads	N
m	mass	Kg
t	time	seconds
W	Displacement at centre of beam	m
D	Cowper-Symonds Constant	s^{-1}
q	Cowper-Symonds Constant	-
v	projectile velocity	m/s^2
Greek		
σ	Stress	N/m^2
ε	Strain	-
κ	Beam curvature	m
γ	Curvature in other direction for plates	m
ω	Beam displacement at plastic hinge	m
θ	Angle at plastic hinges in beam	radians
φ	Second angle describing plastic	radians

	hinge in plate	
λ	multiplier	-
τ	Specific time	seconds
η	ratio of dynamic pulse pressure	-
ζ	position of travelling plastic hinges	m
μ	mass per unit area	Kg/m^2

Subscript

x	in x-direction	-
y	in y-direction	-
z	in z-direction	-
xy	in xy plane	-
xz	in xz plane	-
yz	in yz plane	-
0	at time zero	-
i	at i locations	-
j	at j locations	-
c	collapse	-
eq	equivalent	-
s	slug	-
p	projectile	-
b	ballistic	-

Superscript

·	First derivative	-
··	Second derivative	-
s	static	-
u	upper	-
k	kinematic	-
_	stationary	-
‘	dynamic	-

	(impact rig design)	
V	Volume	m^3

r	radius	m
l	length	m
m	mass	Kg
v	velocity	m/s^2
E	energy	J
P	pressure	Pa
t	thickness	m
W	seal load	N
b	gasket width	m
G	gasket seal diameter	m
y	seating stress	N/m^2
F	force	N
k	gasket factor	-

Greek

ρ	density	Kg/m^3

Subscript

r	reservoir	-
b	barrel	-
s	sabot	-
t	tension	-
i	internal	-
ut	ultimate tensile	-
a	available	-
y	at yield	-

List of Figures

List of Tables

1. Introduction

1.1 Impact on Aircraft Structures

Impacts to aircrafts are regular occurrences and thin aircraft structures are particularly vulnerable to failure through impact damage. These impacts come from many source both during flight, and on takeoff and landing. Uncontained engine failure, bird strike, hail and tyre rubber are just some of the sources of debris that aircraft encounter and there are many reports of such events available in literature. Uncontained engine failure remains one of the major causes of aircraft crashes outside of takeoff and landing. The Society for Automotive Engineers produced a report [1] stating that 315 uncontained rotor failures occurred between the years 1976-1983 and a further investigation by the Federal Aviation Authority in the US [2] described 676 uncontained engine failures occurring in the 28 year period between 1969 and 1997. One particular case [3] on July 6, 1996, saw Delta Airlines Flight 1288 experience an uncontained failure of the left engine resulted in pieces of the hub and attached fan section being flung out at high speed and tearing into the fuselage (see figure 1.1).

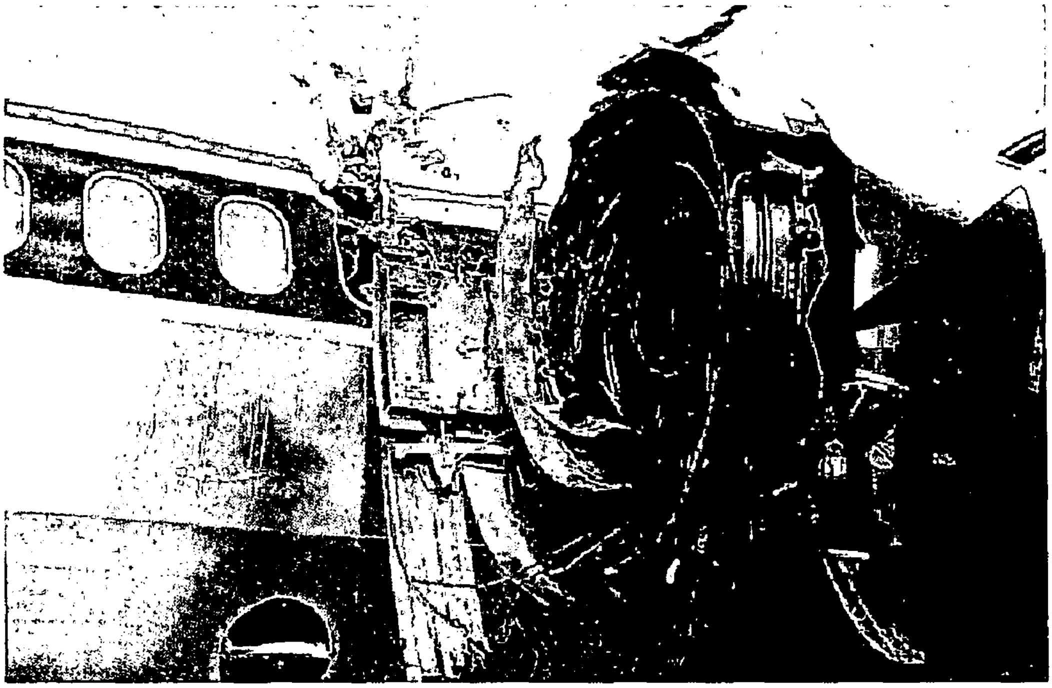

Figure 1.1: Damage to Delta Airlines Flight 1288 [3]

A mother and her 12-yr-old son died instantly as blades and fragments penetrated the cabin.

Bird strike is one of the main causes of uncontained engine failure as well as direct damage to other parts of the aircraft fuselage. Between 1990 and 2002, 46,514 wildlife strikes were reported to the FAA [4] with bird strikes accounting for 97% of these. The most common aircraft components struck by birds were nose, windshield, engine, wing/rotor, and fuselage with engines suffering the most frequent damage at 34% of all damaged components.

Engine failure is not the only cause of catastrophic damage caused by debris impact. An obvious example of this was the Air France Concorde flight 4590 crash near Paris Charles de Gaulle airport in 2000, figure 1.2 [5]. The inquest determined that the major cause of the accident was a tyre blow out caused by debris on the runway. This piece of tyre rubber impacted the underside of the left wing causing a mechanical reaction to form a shock wave in the fuel tank which appears to have ruptured the tank. The leak caused an engine fire and subsequently caused the plane to crash.

Figure 1.2: Engine fire in Air France Concorde flight 4590 [5]

1.2 The Finite Element Method and the Analysis of Impact Events

The finite element method was first developed in the 1960's with the appearance of digital computers. In the late 1960's the problem of plasticity was introduced to finite element analysis when an elastic-plastic constitutive model was incorporated into a commercially available code. Initial applications were restrained to problems containing plastic strains in the order of 0.1% but in the 1970's limited nonlinear solvers were developed that could handle problems with higher strains. Since then the advances in computer technology, both hardware and software, has resulted in advanced implicit and explicit solvers becoming available with the capabilities to analyse and reproduce the complex behaviour encountered during impact events. One such application involves simulating the response of a fuselage skin when impacted by uncontained aircraft engine debris. Developing accurate finite element models and analysis of this event has the potential of significantly improving the design, reliability, and safety of engines and primary aircraft structures, especially for commercial transport applications. Two potential hazards involving turbine-engine debris are:

- Containing failed engine debris within the engine housing - contained failure. Examples of research in this area include an FAA report on uncontained engine failure [2] and the work of Carney et al. [6].
- The potential impact of uncontained failed engine debris on other parts of the aircraft - uncontained failure. Examples of research in this area include the work of Lundin [7], Frankenberger [8] and Knight et al [9].

Most of these studies have used simple plates to simulate the aircraft skins behaviour during impact, with some then attempting to introduce new materials such as CFRP to improve behaviour. Analysis of more complex aircraft geometries has however been limited. The European program entitled "IMT crashworthiness for commercial aircraft" [10] concluded that although finite element methods could accurately predict failure to aircraft structures when the mode of failure included plastic hinge development, the accuracy of models predicting failure through plate or fastener failure was unsatisfactory. Rivet modeling in particular has been seen to be a problem due to their nonlinear behaviour and the effects induced in the plate during the riveting process [10].

1.3 Thesis Objectives

The objectives of this thesis are as follows:

- To obtain an accurate finite element model of the impact of a blunt, cylindrical projectile on an aircraft skin material (Al 2014 T4)
- To use the modelling knowledge gained in the first task to model a more complex aircraft geometry including rivets and stringers.
- To investigate the different modelling techniques available for rivets and to compare them with regards to accuracy and cost
- To design and develop a new impact testing rig with the knowledge gained from the tasks above

1.4 Summary of Chapter 1

Chapter 1 introduced the concepts and causes of impacts to aircraft structures. An overview was given of the accidents that may occur when debris impacts an aircraft and some of the consequences of such impacts were seen. A brief history of the finite element method was presented along with its application to highly dynamic deformations and failures such as those seen in high energy impact events.

2. Literature Survey

2.1 Introduction

This thesis seeks to examine impact to aircraft structures using finite element analysis. As aircraft structures are essentially thin skins with support structures the literature survey presented here looks initially at impacts to general plates and plate structures before examining aircraft structures in more detail. Both experimental and analytical studies along with finite element analyses are investigated with the purpose of identifying common areas of research and reoccurring problems.

2.2 General Experimental and Analytical Studies

The field of impact dynamics covers an extremely wide range of situations and is of interest to engineers from a number of different disciplines. Indeed whenever two bodies collide or risk collision the subject of impact dynamics arises. The studies that have been undertaken of impact on plates and plate structures have various aims and application ranging from armour to metal forming to debris protection and the materials under study have ranged from titanium alloys to aluminium alloys to composites such as CFRP. The field also covers a large range of loading conditions such as hypervelocity impact, blast loading, jet impact, projectile penetration, dropped-object loading, structural crushing etc. This literature review concentrates primarily on the impact of metallic targets with thicknesses of the order of magnitude of the impinging projectile (plates) subject to sub-ordnance velocities (up to approximately 300m/s) from the viewpoint of investigating the penetration and perforation processes involved.

There are several different mechanisms by which a target can fail and these may occur singly or in combinations of two or more. The eight most commonly occurring types of failure of thin or intermediately thick targets have been identified as those shown in figure 2.1 [11]

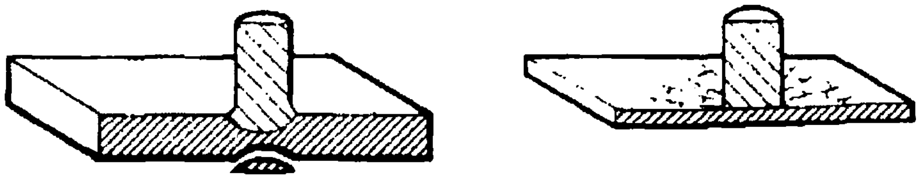

(a) Fracture due to initial stress wave (b) Radial fracture behind initial wave in a brittle target

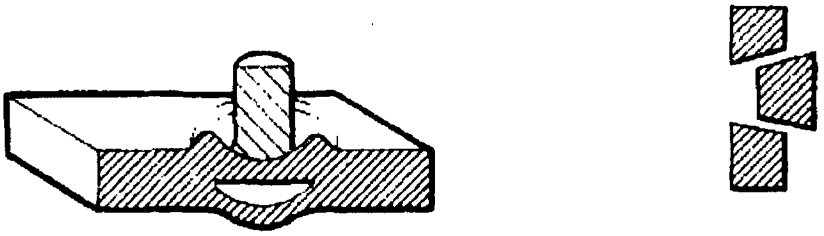

(c) Spall failure (scabbing) (d) Plugging

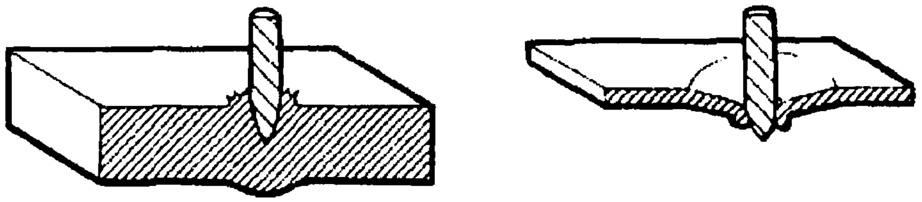

(e) Petaling (frontal) (f) Petaling (rearwards)

(g) Fragmentation (h) Ductile hole enlargement

Figure 2.1: Perforation mechanisms in plate failure [11]

Extensive investigations into the loading of thin metal plates have shown that the piercing load, the energy absorbed during perforation and the dominant failure mechanisms are all strongly dependent on the nose shape of the projectile. Borvik et al. [12] examined the effect of three different nose shapes (blunt, hemispherical and conical) on the ballistic limit for 12mm thick Weldox 460E steel plates. The ballistic limit is defined as the velocity required to obtain perforation of the plate. The ballistic limit was seen to be similar for the conical and hemispherical tipped projectile, approximately 300m/s, where as it was much lower for the blunt projectiles at 185m/s. The study also showed that the residual velocity was influenced by nose shape with the blunt and hemispherical projectile's velocity coinciding as the impact velocity becomes high compared with the ballistic velocity. The residual velocity (the velocity of the projectile after the impact event) for the conical nosed projectile in this case is much higher and approaches the residual velocity line (i.e. the residual velocity for a plate of zero thickness). The differences in the ballistic velocities for the different projectiles are attributed to the change in energy absorption and failure mode of the target for each nose shape. The variation in residual velocities is partly caused by projectile deformation with the deformation of the blunt projectiles increasing linearly with impact velocity whereas conical projectiles hardly deform at all. It was also seen that sliding friction effects can be neglected for blunt projectiles but not for the conical or hemispherical projectiles.

The energy required for perforation of steel plates under impact loading conditions was also shown to be dependent on projectile nose shape by Corran et al. [13]. Blunt nosed projectiles of different radii were fired and the critical impact energy (the energy required to reach the ballistic limit) for each radius was recorded. The effect of increasing the nose radius was to change the mechanism of penetration from ductile hole enlargement to tensile thinning to shear failure each of which related to a change in the critical impact energy. The energy absorption mechanisms encountered when impacting a flat plate with a blunt projectile were analysed by dividing the energy into the four components as in figure 2.2. Corran et al. [13] also investigated the effects of clamp pressure on the ballistic limit of the target and found a steady increase in the velocity needed for ballistic penetration with decreasing clamp load. This runs contrary to claims of previous authors who have tended to disregard changes in clamp conditions [11]. Shen et al. [14] also found that nose radius affected the energy needed for perforation. It was observed that deformation consisted of local indentation and a global deformation and that the local indentation played a significant role and should not be neglected.

Goldsmith and Finnegan [15] investigated impact on aluminium and steel plates by projectiles (hard steel spheres) travelling between sub-ordnance (150m/s) and ultra-ordnance (2,700m/s) velocities.

1. Elastic energy:

$$E_e = \frac{3\pi r_c^2 h_0 (1 - v^2)\sigma_y^2}{8E}$$

2. Plastic energy:

$$E_p = \int_{r_p}^{r_c} (N_0 \varepsilon_r + M_0 \kappa_r + M_0 \kappa_\theta) 2\pi r \cdot dr$$

3. Plugging energy:

$$E_{pl} = 2\pi r_p e h_0 \tau_y \gamma_f$$

4. Projectile mushrooming:

$$E_m = \frac{2\pi \sigma_y H a^3}{9(b-a)} \left(3\left(\frac{b}{a}\right)^3 \ln\left[\frac{b}{a} - \left(\frac{b}{a}\right)^3 + 1\right]\right).$$

r_c = clamp radius, h_0 = initial thickness, v = velocity, σ_y = material yield stress, E = Young's modulus, r_p = projectile radius, N_0 = full plastic membrane force, ε_r = radial strain, M_0 = full plastic yield moment, κ_r = radial curvature, κ_θ = circumferential curvature, e = width of intense shear zone around projectile edge, τ_y = shear yield stress, γ_f = shear strain to failure, a = projectile nose radius before mushrooming, b = projectile nose radius after mushrooming

Figure 2.2: Absorption energies associated with deformation mechanisms for impact of blunt projectile on flat plate [13]

Measurements taken included the initial and residual projectile velocities, the strain histories at several points, and the dimensions of the final deformation of the impact area and projectile. The velocity drop between the initial and residual velocities was seen to decrease to a minimum just above the ballistic limit and then increase steadily thereafter. A dishing in the plug ejected by thin targets was observed similar to that shown in figure 2.3 and was shown to be at a maximum at the ballistic velocity. High speed photographs of the impact event showed that the terminal plug and projectile velocities were very similar.

Levy and Goldsmith [16] investigated the impact of hemispherical, conical and blunt nosed projectiles on aluminium alloy and steel plates, measuring the forces, strains, permanent deflections and plug shapes produced. The projectiles contained a piezoelectric crystal which enabled it to measure the force of the impact directly. The paper's main conclusions were that plug formation is concurrent with other deformations occurring to the plate, that permanent deflections and peak force increase up to the ballistic velocity and drop thereafter and that permanent hoop and radial strains in the plates are significant in the impact zone but decrease rapidly with increasing radius from the impact. Force-time histories obtained for different projectile shapes indicate that hemispherical and blunt projectiles tend to produce shorter impact force duration times but higher peak loads than conically-ended projectiles.

Deya et al. [17] examined the effect of conical, ogival and blunt nosed projectiles on steel of varying strengths. The experimental analysis found that the ballistic velocity for the ogival and conical projectiles was much greater. It also found that an increase in strength of the material caused an increase in the ballistic velocity of the plates for the conical and ogival projectiles while the same increase in strength in the blunt nosed case resulted in a decrease in the ballistic velocity. One reason for this may have been a change in the micro-structure of the material in the shear bands caused by the plugging failure.

Borvik et al. [18] performed a series of tests on impact to aluminium alloy (AA5083-H116) plates between 15mm and 30mm thick. For each target thickness, the initial projectile velocity was adjusted so that the projectile impacted the target at velocities well above and just below the ballistic limit of the target. Conical and ogival projectiles were used and all of the plates failed through ductile hole enlargement. The projectile opened a hole in the plate at the point of impact and the hole was enlarged as the projectile passes through due to high radial pressure. The plate material surrounding the hole was thickened as a result. It was noted that the time taken for the projectile to pierce the plate increased almost linearly as a function of target thickness even though different impact velocities were involved. The impact resistance of the aluminium was compared with some previous tests carried out on steel and concrete targets and it was seen that for equal perforation resistance a smaller weight of aluminium was needed than either steel or concrete.

The effects of plate thickness were again investigated in Chen et al. [19] with thin, intermediate and thick plate being impacted by a blunt projectile. An analytical model used to predict the ballistic limit and residual velocity was developed. Three separate models were presented for thin, intermediate and thick plates with assumptions such as perfectly plastic material for the plate and perfectly rigid material for the projectile. It was also assumed that the projectile and the plug travel at the same velocity once the plug is formed. The model is valid for the perforation of plates by shear plugging failure with or without structural bending response and local penetration. The model was compared with experimental results from several sources and gives good correlation. Another analytical model developed by Chen et al. [20] based on the Johnson-Cook flow law shows that when the thickness of the plate increases, penetration may become a distinct stage and in this case, a two-stage model should be introduced for thick plates (i.e. penetration/indention and shear plugging via the dynamic cavity expansion model and the rigid-plastic model).

Leppin and Woodward [21] also examined the effects of plate thickness and projectile geometry, this time on thin titanium alloy plates. Titanium was chosen because of its known susceptibility to plugging. Blunt projectiles produced a similar deformation through shear plugging as seen in other materials. Conical projectiles, however, produced a result unique to titanium. The mechanisms by which the plate allowed projectile passage, once the initial plug was formed, was seen to change as the plate thickness and/or nose cone angle were increased, figure 2.3. At low velocities a plug smaller than the projectile diameter was ejected with no penetration of the projectile through the plate. When the projectile velocity was increased the formation of the small plug was followed by the formation of an annulus as the projectile passed through the pate.

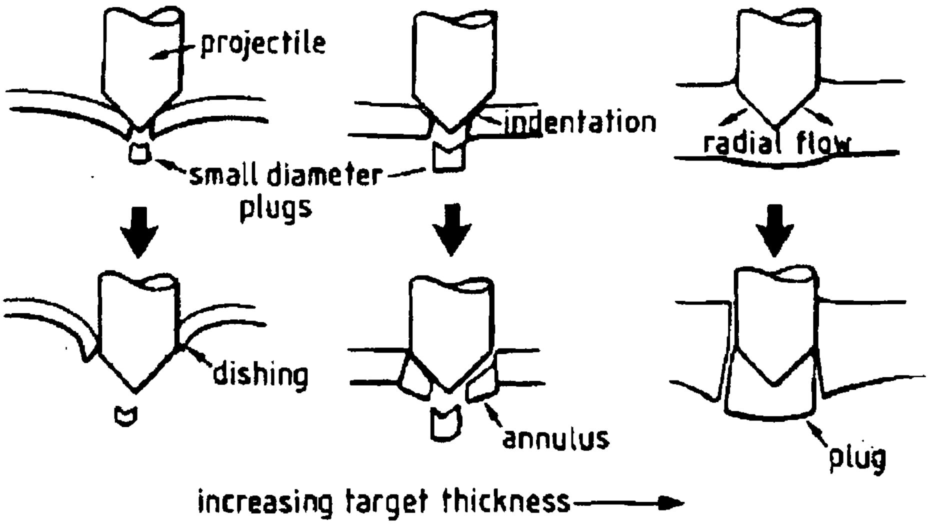

Figure 2.3: Schematic illustration of the effect of target thickness on failure mode of titanium alloy targets [21].

This mode of deformation only occurred for the thicker plate with the 1mm plates failing through local bending and petalling. With a further increase in thickness the failure mode changed again to that observed in other metals with material undergoing radial flow before the occurrence of plug formation.

Titanium alloys were again investigated by Nesterenko et al. [22] who compared the ballistic performance of hot isostatically pressed (HIPed) Ti–6Al–4V targets to targets made from commercially available Ti–6Al–4V alloy. The main purpose of this comparison of ballistic behaviour was to investigate the feasibility of using powder for processing of armour-related materials. Two projectiles were used, blunt ended and conical, against 10mm and 30mm plates respectively. It was seen that shear localization dominated the deformation in the baseline material whereas in the powder-based material fracture also played an important role. Extensive fracturing of the plate was observed in the penetration behaviour observed for the latter case which was totally different from the common modes seen in the first case. The HIPed targets from Ti–6Al–4V powders exhibit a good ballistic performance against perforation and plugging in comparison with the baseline material

Langseth and Larsen [23] carried out an in-depth investigate into the plugging capacity of dropped objects on steel plates. The analysis was performed to simulate dropped drill housings onto oil rig platforms. Similitude analysis was used to construct 1:4 scale model of a typical offshore deck panel being struck by a falling drill collar. The projectiles used in the tests were flat-faced and had masses ranging from 18 to 50 kg. The effects of target thickness, projectile mass and in-plane target stiffness on the energy required to perforate the panels were investigated. It was found that the critical plugging energy increased with plate thickness, decreased with increasing projectile mass and decreased with increasing in-plane panel stiffness over the velocity and mass range tested. The effect of stringers attached to the mid span on the critical plugging energy was investigated and found to be negligible as were strain rate effects.

The influence of the obliqueness of the impact angle on the penetration and perforation of steel and aluminium target is discussed by Goldsmith and Finnegan [24]. The investigation concluded that projectile nose shape and mass had little effect on the ballistic limit and that the impact on a plate is not overly sensitive to increases in obliquity with the ballistic limit rising from 97m/s at normal incidence to only 130m/s at 53° incidence for 3.175mm aluminium plates struck by hardened steel projectiles. The deformations seen for the oblique impacts were similar to those noted for normal impacts with petalling and plugging both present. However the pattern of the petalling differed for different angles of incidence and petals on one side were often sheared off as the projectile penetrated the plate. The perforations became more oval-shaped as the obliquity increased. The exit obliquity angle was also examined and it was noted that it increased more rapidly with initial angle of incidence for the 3.175mm aluminium plates but varied linearly for the thicker aluminium plates and both the steel plates as seen in figure 2.4.

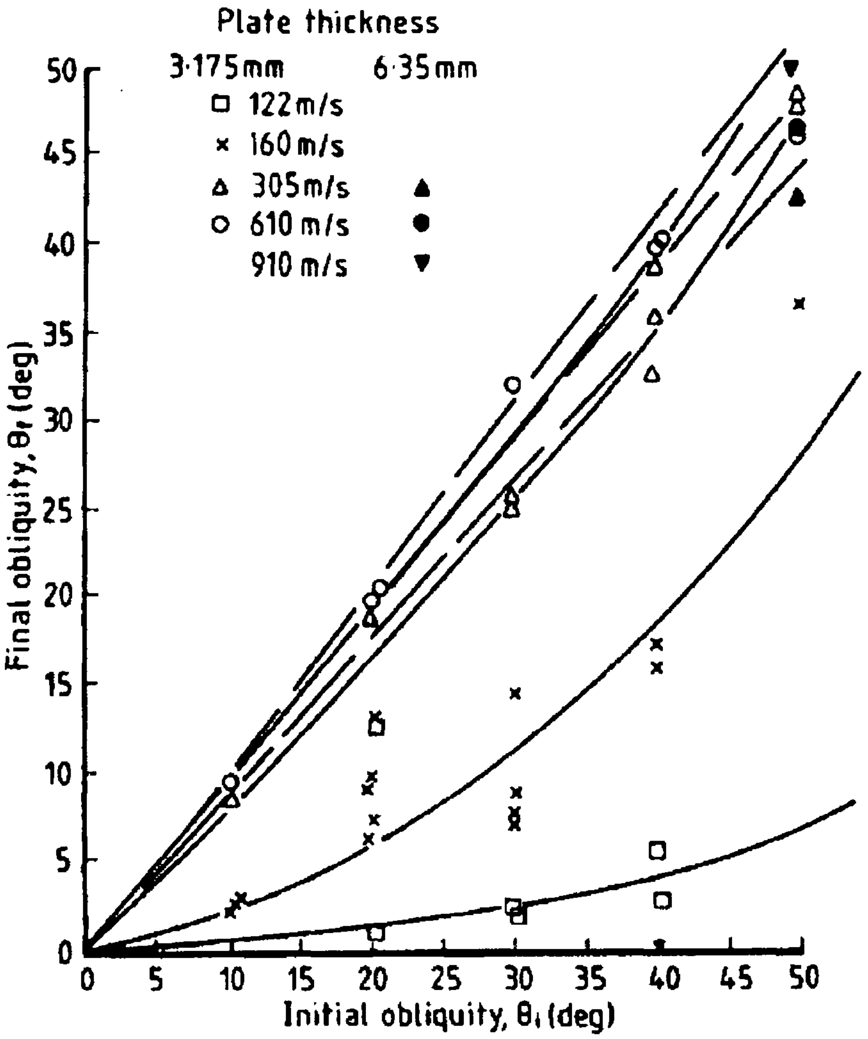

Figure 2.4: Final obliquity as a function of initial obliquity for 3.175mm and 6.35mm thick 2024-0 aluminium targets struck by hard steel conical nosed projectiles [24].

Li and Goldsmith [25] took the problem of oblique impact a further step with the addition of a tumbling projectile. A phenomenological model was presented for the perforation of moderately thick aluminium alloy plates by tumbling projectiles. The perforation process was seen to consist of four stages: erosion, plugging, hole enlargement and petalling. The plugging stage was then further broken up into cratering, plug formation, plug separation, plug slipping and post perforation deformation. The model also considers bulging and voids created by projectile rotation. The numerical model was programmed in FORTRAN and compared with experimental results. Good correlation was found between the two for both the residual velocity and oblique angle for the projectile. This is also true for the computed and observed final velocities of the plug, however, good correlation for the final oblique angle of the plug was not seen. It was explained that the forces acting on the plug were not axi-symmetric and that the direction of the plug was strongly effected by the last portion of the shear process, which was very hard to predict. The model also failed to predict accurately any perforation with an impact angle over 25° as the dominant failure model changed from plugging to petalling.

2.3 General Numerical Studies

Finite element and other numerical methods have been accepted these days as general computational tools in all areas of engineering and have been observed to simulate non-linear events accurately. Even so, some behaviour such as perforation of plates, which involves material instabilities and highly dynamic responses, remains difficult to reproduce. Borvik et al. [26] noted that the complexity of the fracture process in shear plugging has limited both numerical and analytical studies in the area, with the problem being mostly treated experimentally. With this in mind a computational model for visco-plasticity and ductile damage was developed and implemented in the explicit finite element code LS-DYNA. A study was conducted varying parameters such as strain-rate and temperature dependence in the Johnson-Cook constitutive model to investigate their importance. Element size was found to be a vital parameter in numerical simulations involving adiabatic shear localization and strain-rate sensitivity, temperature and stress states (tension, compression or shear) were all found to be significant. The model gave good agreement between plugging failure observed in the experimental analysis and the numerical analysis, see figure 2.5. It was noted that no discussion was made in the paper of contact algorithms or adaptive meshing and while these issues were not significant in the modelling of plugging failure they may have large effects in other cases such as ductile hole enlargement.

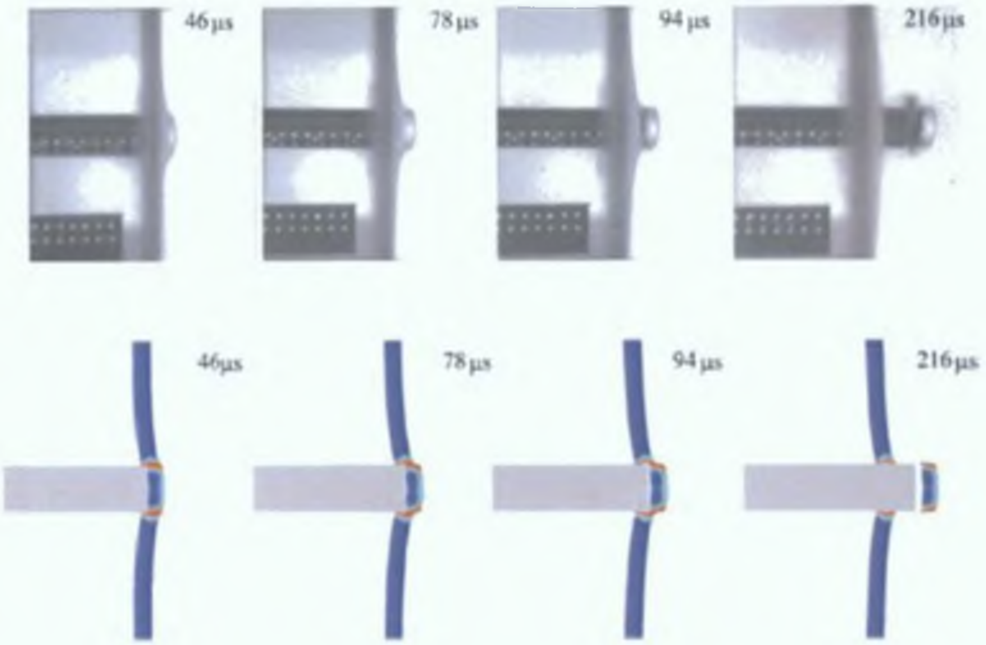

Figure 2.5: High speed camera images compared with numerical simulation from Borvik et al. [26]

A further study by Borvik et al. [27] involved the modelling of impact with blunt, conical and hemispherical nosed projectiles. Again the simulation was conducted using the LS-DYNA explicit code and the Johnson-Cook constitutive equation. The projectile was modelled with a simpler bilinear elastic-plastic model. Severe element distortions were experienced when modelling the impact of the conical nosed projectile resulting in the termination of the simulation. Adaptive meshing was used to overcome the problem. In general, close correlation between numerical and experimental results was achieved. Important parameters in the penetration problem such as ballistic limit velocity, residual projectile velocity, shape of residual velocity curve, maximum target deformation, perforation time and energy absorption, were all well predicted using numerical simulations.

Shi et al. [28] investigated the different finite element modelling techniques of panel-like targets in perforation simulations. The performances of eight-node brick element, four-node quadrilateral thin shell element and eight-node solid shell element were discussed. In general it was observed that the accuracy of the shell modelling of targets in the simulations was controlled by the influence of the transverse normal stress and the wave propagation in the target. This influence, in turn, was controlled by the aspect ratio of projectile diameter to target thickness and the stiffness/strength ratio of projectile to target. The following conclusions were drawn from the study: when the target panels satisfy certain conditions (when normal stress through the plate could be neglected), the thin panel targets can be modelled by shell elements and the model can predict residual velocities of plate perforations. The shell element models of the targets can save computation time and computer memory while still yielding reasonable results compared to the solid element modelling of the targets. In general, the thick (solid) shell element modelling of the target gives better results than the thin shell element. Therefore, the thick shell element is an efficient alternative for the modelling of target materials in the perforation simulations of projectiles against thin panel targets.

The static and dynamic behaviour of plate structures subject to axial compressive loading using the finite element method (FEM) was investigated by Webb et al. [29] using the ABAQUS finite element code. The analysis examines the effects of inertia and strain-rate effects and five distinct phases are seen:

- a pre-compression wave – leading to the establishment of a combined incident and reflected stress wave pattern
- a compression phase
- mechanism formation – and the dissipation of energy by the rotation of the plastic hinges
- separation of the striker from the model brought on by elastic recovery of the deformed plates

The computed FE results were in good agreement, with regard to force, moment and energy considerations, to the experimental results presented.

Kurtaran et al. [30] examined the behaviour of a GT model military jeep door subject to impacts by a bullet at velocities of 500m/s, 1000m/s and 1500m/s using the explicit finite element code LS-DYNA. A comparison was made between two material models commonly used in impact analyses, the plastic kinematic hardening model, which is an elastic-plastic model using the Cowper-

Symonds model to describe strain rate, and the Johnson-Cook model, which is a strain-rate and temperature dependent visco-plastic model. The Johnson-Cook model was used with the Mie-Gruneisen equation of state to describe the pressure-volume relationship in compression and expansion. Finite element simulations were carried out on a single plate 7.62mm in diameter and 2mm thick using the two material models and the results from the two models show a noticeable difference in the deformation of both plate and projectile. According to the authors this is evidence that thermal softening effects are significant in this case although no experimental analysis is presented as validation. Subsequently, the JC model was used and the effects of adding a 2mm plate, a 20mm plate and a 2mm plate angled at 10° to the back of the present plate were investigated.

Park et al. [31] presented what is described as the first trial regarding the optimal design of multi-plate targets under ballistic impact. An optimal design for multi-plate targets subject to ballistic impact was sought using finite element methods, namely the NET2D Langrangian finite element code. The Johnson-Cook constitutive model was used in the simulation to account for strain-rate hardening and thermal softening effects. The response surface method based on the design of experiments was used to obtain the optimal design. The average temperature or the equivalent plastic strain was introduced as a response for the optimisation of the impact problem. The optimised thickness of each layer for which perforation did not occur and for which the strength of the multi-layer plate is maximized is obtained for a constant projectile velocity. As an optimum condition in a two-plate structure, the thickness of the upper aluminium layer increases to 1.34mm from 1.0mm. The thickness of the lower steel layer decreases to 0.66mm from 1.0mm. As a result the total mass is decreased, because the density of aluminium is lower than that of steel, and the strength of the entire structure is improved.

2.4 Aircraft Experimental and Analytical Studies

As mentioned in section 2.1 impacts to aircraft structures can be essentially described as impacts to thin plates and plate structures. Some of the projectiles involved in impacts on aircraft are commonly seen in other areas with debris from unconstrained engine failure producing blunt, conical and spherical shapes. Another area to consider however is the unique range of projectiles that impinge on aircraft including birds and hail.

A series of Federal Aviation Authority (FAA) reports detailed experimental studies into some of the common debris impacts and their effects. Gogolowski and Morgan [32] conducted experiments to test the ballistic capabilities of two commonly used aircraft materials, Al 2024 – T3 and Ti 6AL – 4V. Plates of different thicknesses were impacted with blunt cylinders and fragment stimulant projectiles (FSP) with chiselled noses see figure 2.6. Little difference was seen between the modes of failure for the two projectiles. The modes of failure for the aluminium plates included plugging and petalling depending on the impact velocity. No deformation of the projectile was seen. In the test for the titanium plates, failure occurred by plugging with some mushrooming of the projectile. The results of the tests were used to validate the DYNA-3D finite element code.

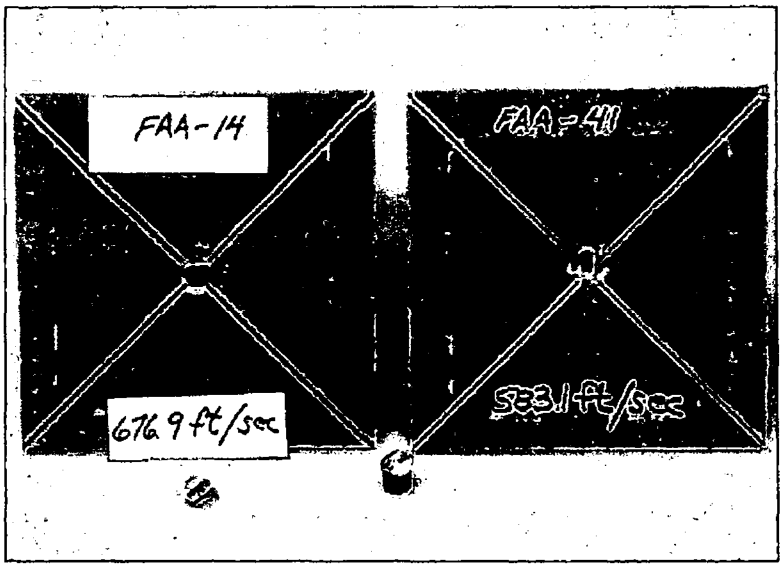

Figure 2.6: Plugging failure in 0.15 inch thick aluminium plates struck with FSP projectile [32].

A second FAA report saw Frankenberger [8] conduct an analysis to identify the characteristics of uncontained engine failure experienced by large commercial aircraft. The objective of the analysis was to define the debris size, weight, exit velocity, and trajectory. The effort was conducted by gathering historical data from uncontained engine failures. This data included, when available, phase of flight, engine operating condition, the failed engine component, aircraft damage location, and damage size. With this basic information, debris size was correlated to damage size. A methodology was developed to estimate debris exit velocity. Representative engine cases and cowls were defined and existing ballistic penetration equations used to calculate debris exit velocity. This analysis was conducted for disk and blade failures on fan, compressor, and turbine components. The analysis showed that present trajectories, defined in FAA regulations, are too narrow and should be expanded. The analysis also highlighted the fact that during an uncontained event the aircraft is subjected to multiple small fragment impacts, not just a single impact. It is the combined effects from the small fragments that pose the highest hazard potential to the aircraft.

A further analysis by Lundin [7] concerned a series of simulated uncontained engine failure tests into aircraft fuselage. A large gas gun was used to fire turbine blade segments of various sizes and impact and residual projectile velocity were noted. An empirical methodology called the joint Technical Coordinating Group for Munitions Effectiveness (JTCG/ME) penetration equations, figure 2.7, which were originally developed to predict the penetration and residual velocity of ballistic weapon projectiles upon impact with various materials, were used to try and predict the residual projectile velocity. The data showed that the penetration equations produce excellent agreement to the actual residual energies for the skin only structure. There is a reduced agreement for the complex structures where the aircraft skin was supported by a stringer.

Liu and Stronge [33] noted impacts by soft or deformable objects, such as birds, result in a shape change for the projectile on impact and the deformation increased the area of the contact surface.

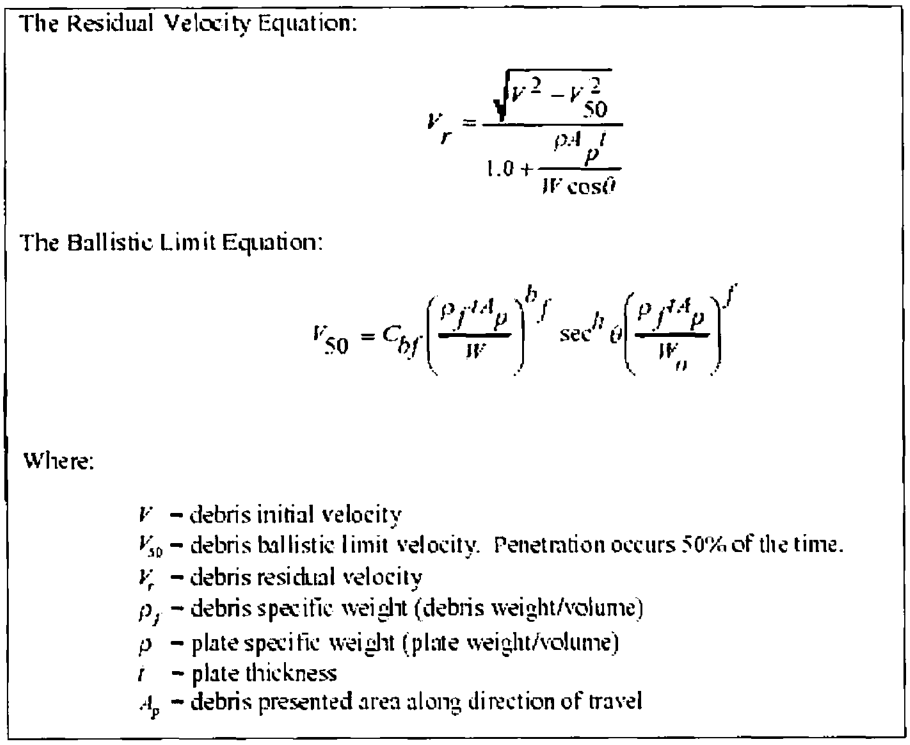

The Residual Velocity Equation:

$$V_r = \frac{\sqrt{V^2 - V_{50}^2}}{1.0 + \frac{\rho A_p t}{W \cos\theta}}$$

The Ballistic Limit Equation:

$$V_{50} = C_{bf}\left(\frac{\rho_f t A_p}{W}\right)^{b_f} \sec^h \theta \left(\frac{\rho_f t A_p}{W_0}\right)^f$$

Where:

V – debris initial velocity
V_{50} – debris ballistic limit velocity. Penetration occurs 50% of the time.
V_r – debris residual velocity
ρ_f – debris specific weight (debris weight/volume)
ρ – plate specific weight (plate weight/volume)
t – plate thickness
A_p – debris presented area along direction of travel

Figure 2.7: Technical Coordinating Group for Munitions Effectiveness (JTCG/ME) penetration equations [7].

The paper investigated the effects of relative deformability of missile and plate on the ballistic limit for thin aluminium plates stuck at normal incidence. A missile deformability index, $\rho_m V_{bl}^2/Y$, was developed where ρ_m is the missile density, V_{bl} is the plates ballistic velocity and Y is the missile dynamic yield stress. It was found that if the index is less than 0.45, the mushrooming of the projectile hardly affects the deformation and failure behaviour but for values greater than 0.45 the effects are significant and the failure is more likely to occur by discing than by plugging.

2.5 Aircraft Numerical Studies

The same problem with complexity noted in section 2.3 for plate structures are true for aircraft structure modelling when using finite element and other numerical methods. Here several specific cases are presented with their analysis of the difficulties and solutions. Knight et al. [9] examined the modelling of uncontained engine failure debris impact on aircraft fuselage-like panels. This was simulated by the impact of a blunt titanium projectile on thin aluminium 2024 – T3 plates. The simulations used the LS-DYNA nonlinear transient dynamics finite element analysis code, and comparisons with available test data were made. The modelling parameters were varied to include different mesh densities, contact options and elements, see table 2.1. An analysis of mesh density showed that highly refined model is needed in the vicinity of the impactor. Element size in this region should be 20% to 25% of the smallest dimension of the contact surface on the impactor. Modelling the penetration process using the tied-nodes-with-failure contact approach provided a capability to tear nodes and elements during the event. This approach, while requiring additional modelling effort and computing, provides a way to simulate the petalling observed in some penetration tests. The element-erosion approach was an alternative penetration modelling approach that did not require any additional modelling effort. It was used in conjunction with solid elements. Particular attention was focused on providing accurate parameters for the element erosion approach as incorrect values of the sliding interface penalty factor (SIPF) would result in the projectile passing through the plate without causing any damage. The results from both damage approaches matched well with the test data for the three mode shapes observed; dishing with no penetration, partial penetration with petalling or full penetration with petalling or plugging.

Table 2.1: Table of different SIPF's used with ratios of sliding interface energy, E_s, to total energy, E_t, and internal energy, E_I [9].

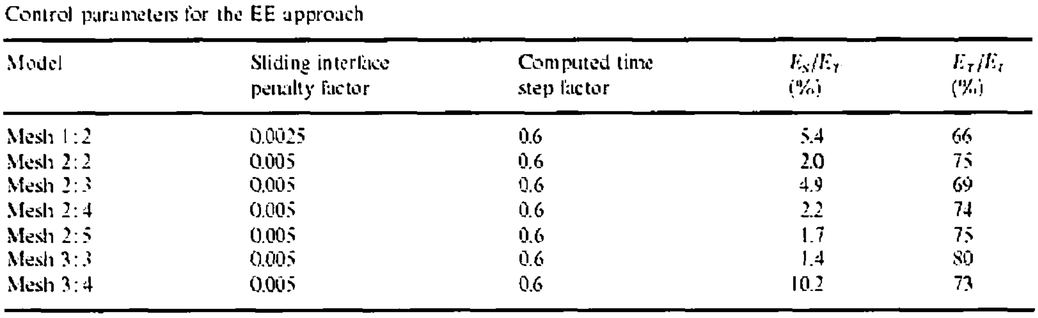

Control parameters for the EE approach

Model	Sliding interface penalty factor	Computed time step factor	E_S/E_T (%)	E_T/E_I (%)
Mesh 1:2	0.0025	0.6	5.4	66
Mesh 2:2	0.005	0.6	2.0	75
Mesh 2:3	0.005	0.6	4.9	69
Mesh 2:4	0.005	0.6	2.2	74
Mesh 2:5	0.005	0.6	1.7	75
Mesh 3:3	0.005	0.6	1.4	80
Mesh 3:4	0.005	0.6	10.2	73

A study by Buehrle et al. [34] was concerned with the ability of the finite element method to predict the modal response of aircraft structures. Two configurations were looked at; a cylindrical shell with stringers and a flat fuselage-like panel. Beam, shell and solid elements were evaluated for the stringer components as well as different attachment models between the stiffeners and the skin. It was found that beam elements were sufficient for characterising the dynamic response of the stringers but that in assembly models solid elements were needed to incorporate the different attachment models. The model of the complete cylinder tended to over estimate the natural frequency of the assembly. The modelling of the fuselage panel concentrated on the stiffener to skin attachment models. It was seen that restraining the entire contact surface between the stringer and the skin produced a model that was too stiff and that constraining the stringer only along a line coincident with the rivets produced better results. Predicted frequencies for this model were still lower than measured however, showing the need for further research in the area of rivet modelling.

Langrand et al. [10] examined the problem of riveted joints more closely. Three main aims were addressed: investigations of structural embrittlement due to the riveting process, mechanical strength characterisation and simplified modelling of bonding. In the first part structural embrittlement was identified, with the maximum and residual strains shown below in table 2.2, and modelled correctly using the finite element code Pam-Crash. In the second part Gurson damage parameters were identified and validated for both sheet and plate materials. Finally a new rivet model was developed using a non-linear spring element to reproduce the pure shear and tensile non-linear behaviour of the rivet. When implemented in an airframe with 700 rivets the new rivet model showed improved response with regard to the experimental testing but still failed to describe the airframe's stiffness correctly and did not reproduce the correct failure phenomenon.

Teng and Wierzbicki [35] presented a parametric study into the perforation process of an aircraft material (Al 2024 – T351) subject to impact, undertaken using the ABAQUS finite element code. In particular crack growth due to shear plugging was investigated and it was found that a critical indentation depth of 0.2h - 0.3h can be used as a failure indicator in shear failure.

Table 2.2: Table of maximum and residual strains induced riveted joints by riveting process. L=length, φ=diameter, δ_j=gauge position, ε_{max}=max strain, ε_{res}=residual strain [10].

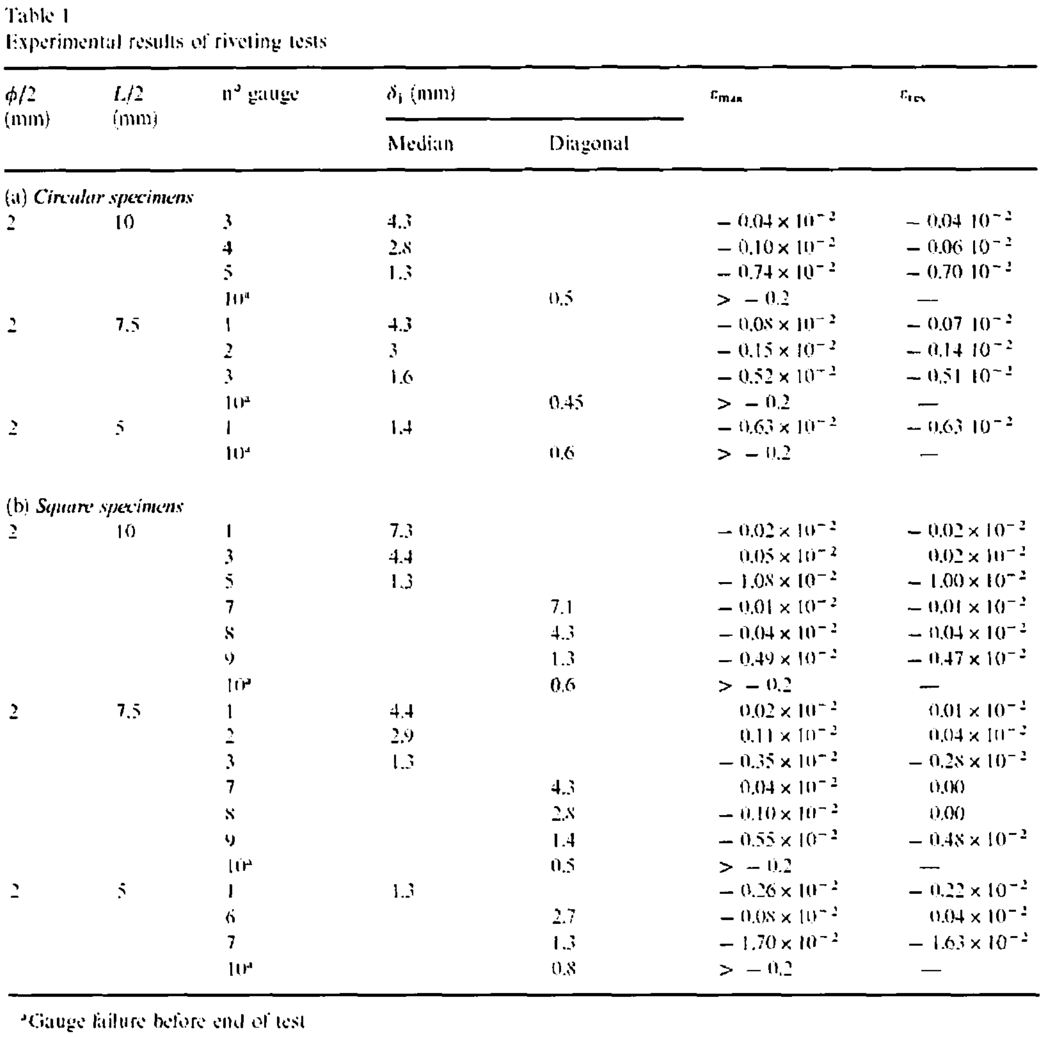

Table 1
Experimental results of riveting tests

$\phi/2$ (mm)	$L/2$ (mm)	n° gauge	δ_j (mm)		ε_{max}	ε_{res}
			Median	Diagonal		
(a) *Circular specimens*						
2	10	3	4.3		-0.04×10^{-2}	$-0.04\ 10^{-2}$
		4	2.8		-0.10×10^{-2}	$-0.06\ 10^{-2}$
		5	1.3		-0.74×10^{-2}	$-0.70\ 10^{-2}$
		10[a]		0.5	> -0.2	—
2	7.5	1	4.3		-0.08×10^{-2}	$-0.07\ 10^{-2}$
		2	3		-0.15×10^{-2}	$-0.14\ 10^{-2}$
		3	1.6		-0.52×10^{-2}	$-0.51\ 10^{-2}$
		10[a]		0.45	> -0.2	—
2	5	1	1.4		-0.63×10^{-2}	$-0.63\ 10^{-2}$
		10[a]		0.6	> -0.2	—
(b) *Square specimens*						
2	10	1	7.3		-0.02×10^{-2}	-0.02×10^{-2}
		3	4.4		0.05×10^{-2}	0.02×10^{-2}
		5	1.3		-1.08×10^{-2}	-1.00×10^{-2}
		7		7.1	-0.01×10^{-2}	-0.01×10^{-2}
		8		4.3	-0.04×10^{-2}	-0.04×10^{-2}
		9		1.3	-0.49×10^{-2}	-0.47×10^{-2}
		10[a]		0.6	> -0.2	—
2	7.5	1	4.4		0.02×10^{-2}	0.01×10^{-2}
		2	2.9		0.11×10^{-2}	0.04×10^{-2}
		3	1.3		-0.35×10^{-2}	-0.28×10^{-2}
		7		4.3	0.04×10^{-2}	0.00
		8		2.8	-0.10×10^{-2}	0.00
		9		1.4	-0.55×10^{-2}	-0.48×10^{-2}
		10[a]		0.5	> -0.2	—
2	5	1	1.3		-0.26×10^{-2}	-0.22×10^{-2}
		6		2.7	-0.08×10^{-2}	0.04×10^{-2}
		7		1.3	-1.70×10^{-2}	-1.63×10^{-2}
		10[a]		0.8	> -0.2	—

[a] Gauge failure before end of test

The affect of mesh density with regard to plugging failure was also examined and it was found that there was a unique asymptotic value of the residual velocity of the plate as the mesh density increases, see figure 2.8.

Carney et al. [6] conducted a study of turbine fan cases with the aim of weight reduction. A simulation of the fan blade containment system was tested experimentally at the NASA GRC Ballistic Impact lab and analysed using the finite element code LS-DYNA. Two configurations were tested, that of a simple flat plate and that of a plate with convex curvature.

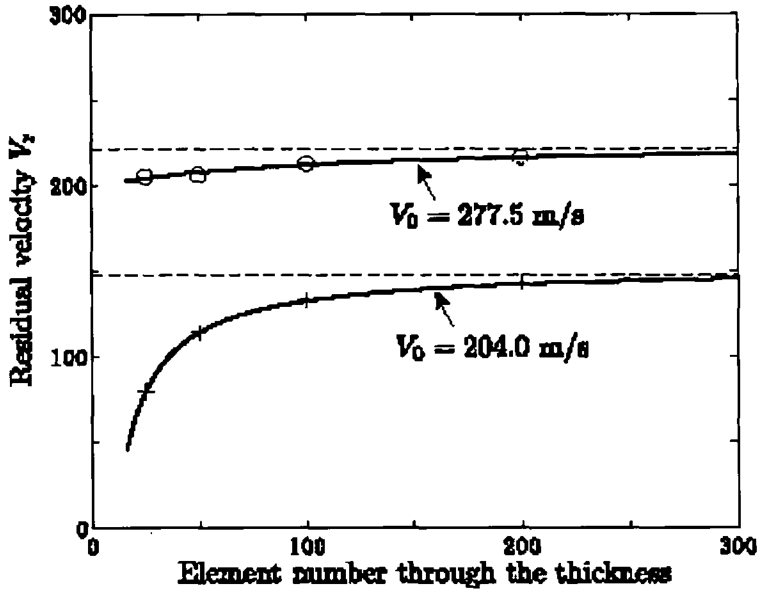

Figure 2.8: Calculated residual velocity vs. element number through the thickness of the plate [35]

It was seen that the curved plate forced the blade to deform plastically, dissipating energy before the full impact and this resulted in higher ballistic velocity for the curved plate. The finite element analysis proved to have good correlation with the experimental results except with respect to the projectile which experienced less deformation than seen experimentally.

The effects of pre-pressurisation on aircraft fuselage panels subjected to impact loading were investigated by Veldman et al. [36]. While the cause of the impact loading (explosives) was significantly different from the other studies reviewed it was felt that the effect of pre-pressurisation was an interesting case. A plate was subjected to tests where an explosive was detonated at a fixed distance from both un-pressurized and pressurised plates. In addition to this finite element simulations were carried out using the ANSYS/LS-DYNA. Comparisons between the experimental and finite element results showed good correlation with regard to permanent deformation of the plate. For the explosive loads measured no significant change in deformation was noted as the pre-pressurisation was increased from 0kPa to 62.1kPa. No perforation of the plates occurred during the testing and it is thought that pre-pressurisation might have a more significant effect in this case.

The final study reviewed here, presented by Anghileri et al. [37], sought to develop numerical methods of predicting damage from hail on aircraft structures. Three numerical models were developed; a finite element model, an arbitrary Langrangain Eulerian (ALE) and a smooth particle hydrodynamics (SPH) model. Initial comparisons were made of impact to flat plates and all three methods resembled experimental tests closely. Subsequently simulations were created of an impact to the nose-lip of an engine nacelle and the results were compared with documented damage with regard to deformation shape and size. Although the differences between the models seemed to be minor it was concluded the SPD model was the most efficient and effective as this model granted the closest correlation to experimental results and has a considerably shorter computation time.

2.6 Summary of Chapter 2

A literature review of impact to plate and aircraft structures was conducted of both experimental and computational studies and it was noted that:

- The deformation behaviour was at its most complex in the range surrounding the ballistic velocity of the plate.
- The most common failure mechanism for conical projectiles was that of ductile hole enlargement with petalling.
- Shear plugging was seen to be the most common form of failure with blunt projectiles.
- For other projectiles such as hemispherical nosed and ogival shapes combinations of shear plugging and ductile hole enlargement were observed.
- In general the ballistic velocity was seen to be greater for blunt nosed projectiles with the limit for conical and hemispherical nosed projectiles being similar
- Plate thickness was seen to be a significant factor in perforation with different failure modes observed as the plate thickness increased

- Residual projectile velocities were often used to compare experimental results and calculate energy absorbed during impact and it was seen that residual velocities reach a minimum just above the ballistic limit and subsequently increase monotonically.
- In finite element studies mesh size, element choice and material models were seen to be significant parameters and it was noted that the element size at impact needed to be 20%-25% of the smallest impact area to ensure sufficient accuracy
- Both shell and solid elements were used successfully in the impact simulations presented although it was observed that solid elements were necessary when dealing with complex assemblies
- The two most commonly used material models were the plastic kinematic hardening model which used the Cowper-Symonds model to describe strain-rate, and the Johnson-Cook temperature dependent visco-plasticity model.
- Some other numerical methods used included the arbitrary Langrangian Eulerian (ALE) methods and the smooth particle hydrodynamics (SPD) method.

3. Theory of Impact to Plates and Plate Structures

3.1 Introduction

Impact Mechanics is a complex area of study and it can be divided into many areas of consideration. The analysis of an impact on a semi-infinite medium differs considerably from an analysis of a plate impact. It is allowable to consider a plate impact if the thickness of the plate is of the same order of magnitude as the diameter of the projectile and the lateral extent of the plate is at least an order of magnitude greater [38]. Beams are defined as structures having a length that is large compared with the height and breath of the member. In this case the main area of interest is the plastic deformation and often partial or complete penetration of the plate. As a result of this the assumption of perfect plastic behavior for the material can be made. The following theory is drawn primarily from reference [39].

3.2 Static Plastic Behaviour of Beams and Plates

To gain a better understanding of the theory behind the dynamic plastic behavior of beams and plates we must first look briefly at the static case. With the assumption of perfect plasticity it is possible to obtain the principal characteristics of the structural response without too much difficulty and with confidence of a reasonable degree of accuracy when compared with experimental results. Firstly some basic beam equations need to be introduced.

3.2.1 Basic Equations for Beams

It is common in beam theory to replace the actual force distribution across the depth of the beam by a shear force, $Q = \int_A \sigma_{xz} dA$, and a bending moment, $M = \int_A \sigma_x z dA$, as seen in figure 3.1. The actual strain field is then described in terms of, κ, the curvature of the longitudinal axis. The lateral and moment equilibrium equations are therefore

$$dM/dx = Q \quad (3.1)$$

and

$$dQ/dx = -p \quad (3.2)$$

where, p is the external load per unit length and the response is time independent. The corresponding curvature change is

$$\kappa = -d^2w/dx^2 \quad (3.3)$$

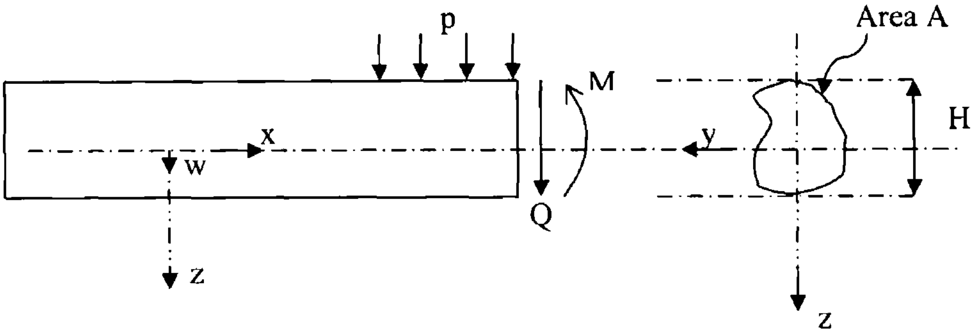

Figure 3.1: Notation for beams

Now if we take a rectangular beam of breath B and depth H into consideration it can be proved that the moment at which yielding occurs can be given by

$$M_y = \sigma_o BH^2/6 \quad (3.4)$$

where σ_o is the initial stress and that if the moment is increased further a collapse moment, M_0, can be found from

$$M_0 = \sigma_o BH^2/4 \quad (3.5)$$

From these two equations it is easy to see that for a rectangular beam

$$M_0 = 1.5M_y \quad (3.6)$$

This 1.5 value is known as the shape factor and depends on the cross-sectional shape of a beam.

3.2.2 Plastic Collapse Theory for beams

In the last section it was shown that M_0 was the moment required for the plastic collapse of a square cross-sectional beam. However this does not explain how beams fail when subjected to a bending moment distribution that varies along its axis. For this we need the limit theorems of plasticity which can provide estimates for the static collapse loads for any external static load. The theorems consist of the lower and upper bound theorems which apply to the static (equilibrium) and kinematic (deformation) requirements respectively.

3.2.2.1 The Lower Bound Theorem

The lower bound theorem states: If any system of bending moments, which is in equilibrium with the applied loads and which nowhere violates the yield condition, can be found, then the beam will not collapse, or is at the point of collapse (incident collapse)

It is assumed that F(x) is defined as the set of external loads that cause incident collapse of the beam and the collapse mechanism for the beam is described by a velocity profile, $\dot{\omega}$(x), and a rotation rate $\dot{\theta}$ with $\dot{\theta}_i$ at i locations. These discrete locations are where the rigid parts of the beam are connected to each other and they are known as plastic hinges. The bending moment distribution is then given by M(x) and M_i at the plastic hinges. According to the principal of virtual velocities [40] it can then be stated that

$$\sum M_i \dot{\theta}_i = \int F \dot{\omega} \, dx \quad \text{.....................................} \quad (3.7)$$

The object of the lower bound theorem in then to find a multiplier λ^1 so that the load $\lambda^1 F(x)$ does not cause the collapse of the beam. The bending moment $M^s(x)$ is then statically admissible if it satisfies the equilibrium equation is section 3.2.1 above and if it never exceeds the yield moment M_0. Again using the principle of virtual velocities we can say that

$$\Sigma M_i^s \dot{\theta}_i = \int \lambda^l F \dot{\omega}\, dx \tag{3.8}$$

which when subtracted from the previous equation gives

$$(1-\lambda^1)\int F \dot{\omega}\, dx = \Sigma(M_i - M_i^s)\dot{\theta}_i \tag{3.9}$$

By the assumption that M and $\dot{\theta}$ are non-negative it can be said that $M\dot{\theta} \geq 0$ and that according to the definition of a statically admissible bending field $|M^s| \geq |M|$. Therefore it can be said that

$$(M_i - M_i^s)\dot{\theta}_i \geq 0 \tag{3.10}$$

and from equation 3.9

$$(1-\lambda^1)\int F \dot{\omega}\, dx \geq 0 \tag{3.11}$$

and since the external work rate

$$F \dot{\omega}\, dx \geq 0 \tag{3.12}$$

$$\lambda^1 \leq 1 \tag{3.13}$$

This proves the lower bound theorem stated above as the multiplier λ^1 will not cause collapse of the beam.

3.2.2.2 The Upper Bound Theorem

The upper bound theorem states: If the work rate of the system of applied loads during any kinematically admissible collapse of a beam is equated to the corresponding internal energy dissipation rate, then that system of loads will cause collapse, or incident collapse, of the beam.

Let it be assumed that a beam collapses under a load $\lambda^u F(x)$ with a bending moment distribution $M^k(x)$ and a velocity field $\dot{\omega}^k(x)$, which has rotation rates $\dot{\theta}^k{}_j$ at j plastic hinges. Thus it can be said that the external work rate is equal to the internal energy dissipation

$$\Sigma M_j^k \dot{\theta}^k{}_j = \int \lambda^u F \dot{\omega}^k \, dx \ldots\ldots\ldots\ldots\ldots\ldots\ldots\ldots (3.14)$$

where $M^k{}_j$ is the bending moment at the plastic hinges.
Again using the principal of virtual velocities it is possible to show that

$$(\lambda^u - 1)\int F \dot{\omega}^k \, dx = \Sigma(M_j^k - M_j)\dot{\theta}_j^k \ldots\ldots\ldots\ldots\ldots\ldots (3.15)$$

and therefore prove

$$\lambda^u \geq 0 \ldots\ldots\ldots\ldots\ldots\ldots\ldots\ldots\ldots\ldots\ldots (3.16)$$

proving the upper bound theorem for perfect plastic beams as stated above.

3.2.2.3 The Exact Static Collapse Load

To get the exact static collapse load both the upper and lower bound theorem results must be true. This can only happen in one case where

$$\lambda^l = \lambda^u = 1 \ldots\ldots\ldots\ldots\ldots\ldots\ldots\ldots\ldots\ldots\ldots (3.17)$$

The solution is then both statically and kinematically admissible.

3.2.3 Static Plastic Collapse of a Fully Clamped Beam

The limit load for the fully clamped beam shown below in figure 3.2(a) is now found using the limit theorems of plasticity. A plastic hinge forms at the centre as seen in figure 3.2(b) and the upper bound calculation gives

$$p^u = 4M_0/L^2 \qquad (3.18)$$

If plastic hinges form at the supports, then the bending moment distribution becomes

$$M = -M_0 + p(L^2 - x^2)/2 \qquad (3.19)$$

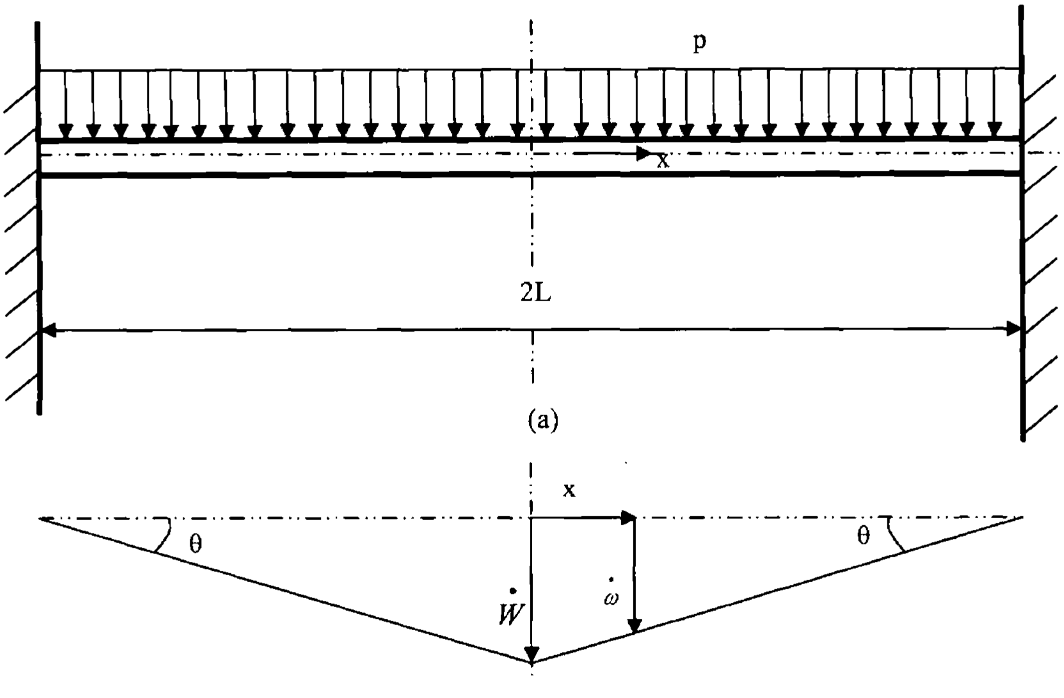

Figure 3.2 (a) Fully clamped beam subjected to a uniformly distributed pressure load. (b) Velocity profile for a fully clamped beam with a plastic hinge at the centre point

Thus it can be shown that the exact collapse pressure at the lower bound

$$p^1 = 4M_0/L^2 \tag{3.20}$$

is obtained when the maximum value of M in eq. (3.19) above is equal to M_0. The exact collapse pressure for a fully clamped beam according to the limits theorems of plasticity is therefore

$$\overline{p_c} = 4M_0 / L^2 \tag{3.21}$$

3.2.4 Basic Equations for Plates

As with the simplification for beams, there are assumptions we can make for plates of a similar nature [41]. To this end the lateral, or transverse, dimension of the plate is assumed to be small compared with the extent of the associated middle surface. As a result the stress in the z direction, i.e. through the thickness of the plate, is said to be negligible. Therefore it is now possible to represent all the stresses in the plate with the following ten generalized stresses

$$\boxed{\begin{array}{lll} N_x = \int_{-H/2}^{H/2} \sigma_x dz & N_y = \int_{-H/2}^{H/2} \sigma_y dz & N_{xy} = N_{yx} = \int_{-H/2}^{H/2} \sigma_{xy} dz \\ M_x = \int_{-H/2}^{H/2} \sigma_x z dz & M_y = \int_{-H/2}^{H/2} \sigma_y z dz & M_{xy} = M_{yx} = \int_{-H/2}^{H/2} \sigma_{xy} z dz \\ Q_x = \int_{-H/2}^{H/2} \sigma_{xz} dz \quad Q_y = \int_{-H/2}^{H/2} \sigma_{yz} dz & & \end{array}} \tag{3.22a-j}$$

where H is the thickness of the plate. These stresses are shown in figure 3.3 below where it can be seen how the plate is idealized as a 2D surface.

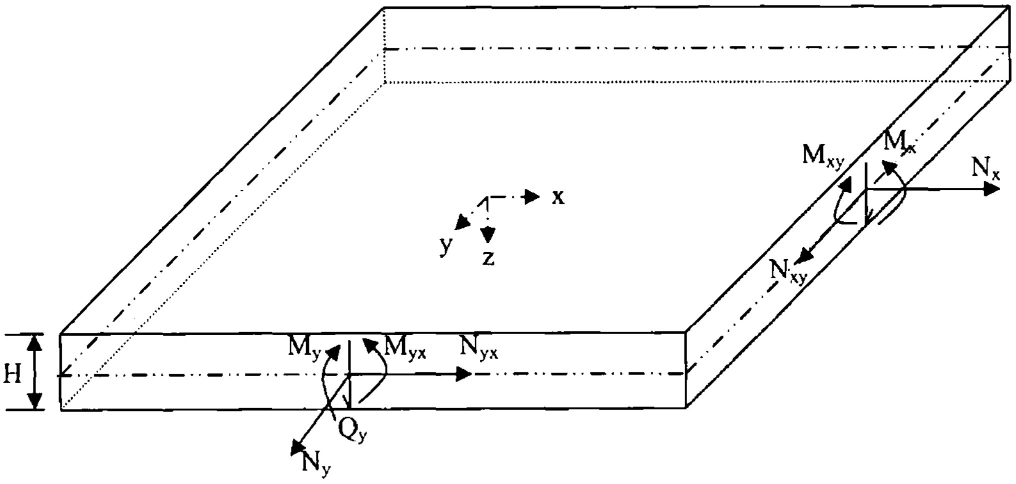

Figure 3.3: Representation of a plate with generalized stresses

The associated strains and curvature changes are thus

$$\varepsilon_x,\ \varepsilon_y,\ \varepsilon_{xy} = \varepsilon_{yx},\ \kappa_x,\ \kappa_y,\ \kappa_{xy} = \kappa_{yx},\ \gamma_x \text{ and } \gamma_y \ldots\ldots\ldots\ldots \text{(3.23a-j)}$$

corresponding to the equations (3.22a-j).

Now for a rectangular plate of uniform thickness it can be said that the $N_x = N_y = N_{xy} = N_{yx} = 0$ if the beam is subjected to lateral or transverse loads and it produces only infinitesimal displacements. This results in the transverse and moment equilibrium equations below

$$\partial Q_x / \partial x + \partial Q_y / \partial y + p = 0 \ldots\ldots\ldots\ldots \text{(3.24)}$$

$$\partial M_x / \partial x + \partial M_{xy} / \partial y - Q_x = 0 \ldots\ldots\ldots\ldots \text{(3.25)}$$

$$\partial M_y / \partial y + \partial M_{xy} / \partial x - Q_y = 0 \ldots\ldots\ldots\ldots \text{(3.26)}$$

and a governing equation may be found by differentiating Q_x and Q_y and substituting the result back into eq. (3.24) to give

$$\partial^2 M_x / \partial x^2 + 2\partial^2 M_{xy} / \partial x \partial y + \partial^2 M_y / \partial y^2 + p = 0 \ldots\ldots\ldots\ldots \text{(3.27)}$$

The principal bending moments, M_1 and M_2, are then defined as

$$M_1 = \frac{M_x + M_y}{2} + \sqrt{\frac{(M_x - M_y)^2}{4} + M_{xy}^2} \qquad (3.28)$$

$$M_2 = \frac{M_x + M_y}{2} - \sqrt{\frac{(M_x - M_y)^2}{4} + M_{xy}^2} \qquad (3.29)$$

3.2.5 Static Collapse of Plate with Simple Supports

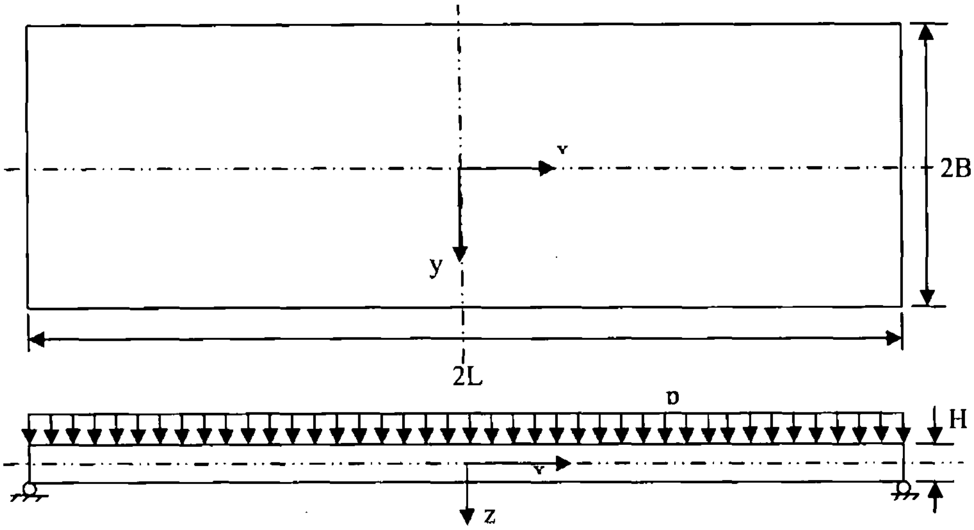

Figure 3.4: Simply supported rectangular plate subjected to a uniformly distributed load

To find the exact collapse pressure for the simply supported beam shown in figure 3.4 the limit theorems of plasticity are again used just as with beams. The plate is assumed to behave in a perfectly plastic manner and to obey the Johansen yield criterion shown in figure 3.5. If the square, Johansen, yield curve had $|M_1| = M_0/2$ and $|M_2| = M_0/2$ then it would inscribe the Tresca yield criterion [42] that the plate material is assumed to obey.

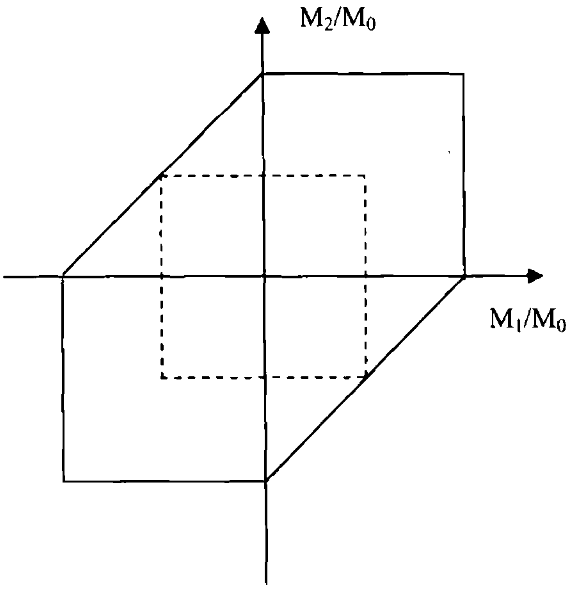

Figure 3.5: Tresca (hexagonal) yield condition with inscribed Johansen yield criterion [42]

3.2.5.1 Lower Bound Calculations

Now symmetry can now be used to further simplify the problem as the plastic collapse of a rectangular plate is symmetrical around both the x and the y axes and therefore only one quadrant is considered. As a result the bending moment must be written in the form

$$M_x = M_0 - ax^2$$

$$M_y = M_0 - by^2 \quad \text{(3.30a-c)}$$

$$M_{xy} = -cxy$$

where $a = M_o/L^2$, $b = M_o/B^2$ and $c = M_o/BL$.

So by differentiating the above generalized stresses and substituting them into the governing equation (3.27-3.29) it can be shown that the

$$p^l = 2M_0[1 + L/B + (L/B)^2]/L^2 \quad \text{(3.31)}$$

is the lower bound to the exact collapse pressure for a rectangular perfectly plastic plate.

3.2.5.2 Upper Bound Calculations

The transverse velocity profile in figure 3.6 is kinematically admissible and can be used to calculate the upper bound to the static collapse pressure for the rectangular plate. It is expressed in the form

$$\dot{w} = \dot{W}(B\tan\phi - x')/B\tan\phi \quad (3.32)$$

in region I and

$$\dot{w} = \dot{W}(B - y)/B \quad (3.33)$$

in region II where $\dot{W}$ is the maximum transverse velocity at the centre of the plate. The angular velocities at the outer support boundaries of the two regions are

$$\dot{\theta}_1 = \dot{W}/B\tan\phi \quad (3.34)$$

$$\dot{\theta}_2 = \dot{W}/B \quad (3.35)$$

and at the boundary between the regions is

$$\dot{\theta}_3 = \dot{W}/B\sin\phi \quad (3.36)$$

Therefore the total internal energy dissipated in the plate is

$$\dot{D} = 4M_0\dot{W}(L/B + \cot\phi) \quad (3.37)$$

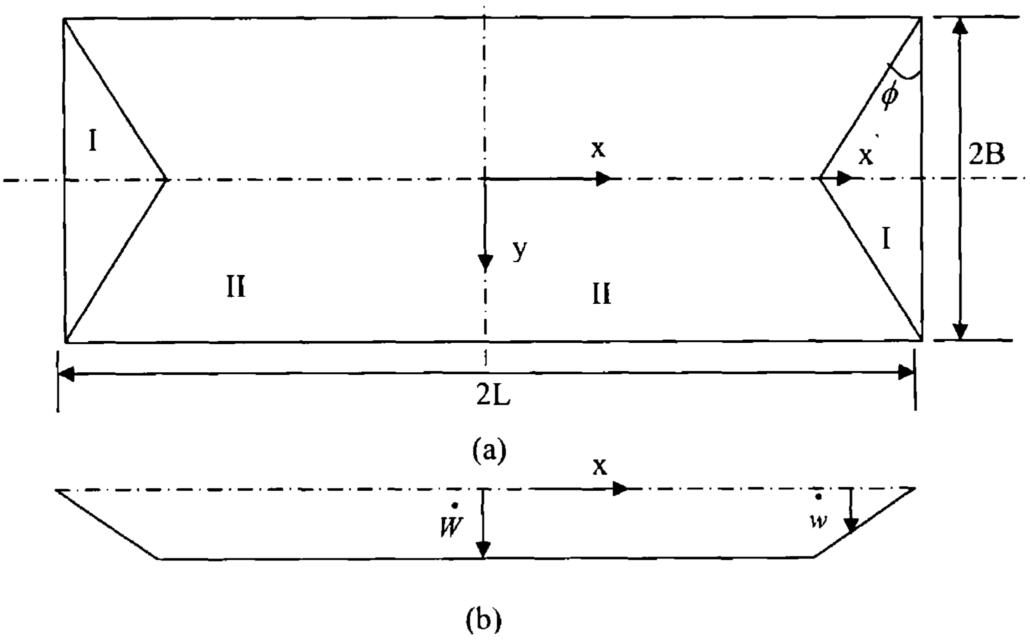

Figure 3.6: Static plastic collapse of a simply supported rectangular plate (a) plan view of plastic hinge (b) side view of transverse velocity profile

where $M_0 = \sigma_0 H^2/4$.

If the internal energy dissipation is then equated to the external work rate, which is

$$\dot{E} = 2B^2 \dot{W} p''(L/B - \tan\phi/3) \quad (3.38)$$

then the static collapse pressure can be found to be

$$p_u = \frac{6M_0(1 + \beta/\tan\phi)}{B^2(3 - \beta\tan\phi)} \quad (3.39)$$

where $\beta = B/L$.

The collapse pressure p_u is then at a minimum when $\frac{\partial p_u}{\partial \tan\phi} = 0$ thus

$$\tan\phi = -\beta + \sqrt{3 + \beta^2} \quad (3.40)$$

Substituting this in eq. (3.39) gives the exact collapse pressure to be

$$p_u = \frac{6M_0}{B^2(\sqrt{3+\beta^2}-\beta)^2} \quad \text{.......} (3.41)$$

3.3 Dynamic Plastic Behaviour of Beams and Plates

3.3.1 Considerations for Dynamic Plastic Collapse of Beams

The assumptions and simplifications that were made earlier in the earlier sections for beams are still relevant here, when discussing dynamic loading. The elastic effects are again assumed to be negligible and therefore the perfect plastic model is again adopted. The procedure for generating the theoretical solution is very similar to that of the static case and indeed the kinematically admissible velocity field needed is often very similar to the static collapse profile. The normality requirements of plasticity are used to find the correct portion of the yield surface that is associated with the velocity field by integrating the governing equations and meeting the initial and boundary conditions it is usually possible to find a solution. However if there have been any yield violations then the velocity profile used is insufficient and another must be tried for these cases. The governing equations for the dynamic behavior of a beam are

$$Q = \partial M / \partial x \quad \text{.......} (3.42)$$

$$\partial Q / \partial x = -p + m\partial^2 w / \partial t^2 \quad \text{.......} (3.43)$$

$$\kappa = -\partial^2 w / \partial x^2 \quad \text{.......} (3.44)$$

which are the same as the equations for the static case except in eq. (3.43) where the effects of inertia are included. Thus the theoretical solution must satisfy equations (3.42) and (3.43) along with the initial and boundary conditions. The bending moment, M, must remain statically admissible i.e. $-M_0 \leq M \leq M_0$ and not violate yield conditions. The curvature rate vector in the active plastic region must also be normal to the yield curve at the corresponding point i.e. $\dot{\kappa} \geq 0$ when $M = M_0$ and $\dot{\kappa} \leq 0$ when $M = -M_0$. The theoretical solution is then said to be exact if the generalised stress field is statically admissible and the transverse velocity field is kinematically admissible.

3.3.2 Dynamic Collapse of a Simply Supported Beam

Now under consideration is the dynamic response of the beam shown in figure 3.7. It is subjected to a pressure pulse, figure 3.7(c), which may be expressed in the form

$$p = p_0 \text{ for } 0 \leq t \leq \tau \quad \text{.................................} (3.45)$$

and

$$p = 0 \text{ for } t \geq \tau \quad \text{....................................} (3.46)$$

The above equations suggest that it is convenient to consider the analysis in two time steps i.e. $0 \leq t \leq \tau$ and $\tau \leq t \leq T$ where T is the duration of the motion of the beam. As before we need only consider one half of the beam $0 \leq x \leq L$ due to symmetry.

3.3.2.1 First Phase of Motion $0 \leq t \leq \tau$

The transverse velocity field shown above in figure 3.7(b) can be expressed in the form

$$\dot{w} = \dot{W}(1 - x/L) \text{ for } 0 \leq x \leq L \quad \text{..........................} (3.47)$$

where $\dot{W}$ is the lateral velocity at the midpoint.

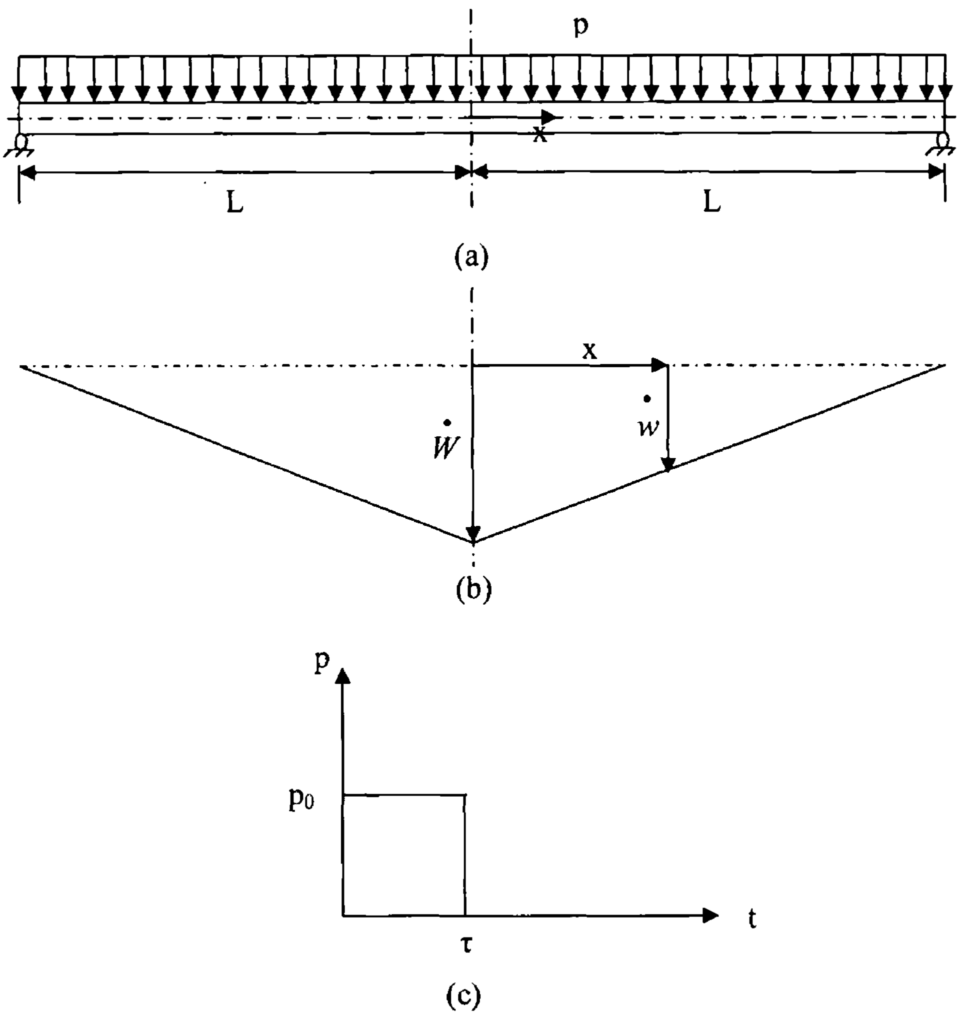

Figure 3.7: (a) Uniformly loaded beam with simple supports. (b) Transverse velocity field. (c) Rectangular pressure pulse.

The change in the curvature $\dot{\kappa}$ can be shown by equations (3.44) and (3.47) to be zero except at x = 0 where $\dot{\kappa} = \infty$. This means that the beam can be idealised as two rigid section connected by a plastic hinge. Now by differentiating eq. (3.42) and substituting it into eq. (3.43) it is possible to show that

$$\partial^2 M / \partial x^2 = -p_0 + m(1 - x/L) d^2 W / dt^2 \quad \text{......................} \quad (3.48)$$

which when integrated gives

$$M = -p_0 x^2 / 2 + m(x^2/2 - x^3/6L) d^2 W / dt^2 + M_0 \quad \text{..................} \quad (3.49)$$

but since M = 0 at x = L for a simply supported beam

$$d^2W/dt^2 = 3(\eta - 1)M_0/mL^2 \qquad (3.50)$$

where $\eta = p_0/p_c$ is the ratio of the dynamic pressure pulse to the static collapse pressure load. Integrating with respect to time and taking into account that the first phase of motion is finished at $t = \tau$ gives

$$W = 3(\eta - 1)M_0\,\tau^2/2mL^2 \qquad (3.51)$$

and

$$\dot{W} = 3(\eta - 1)M_0\,\tau/mL^2 \qquad (3.52)$$

3.3.2.2 Second Phase of Motion $\tau \le t \le T$

At $t = \tau$ the pressure p_0 is removed and displacement in this section is caused by residual kinetic energy as the beam still has a transverse velocity. The velocity field is assumed to still be valid so eq. (3.50) now becomes

$$d^2W/dt^2 = 3M_0/mL^2 \qquad (3.53)$$

which when integrated using equations (3.51) and (3.52) as initial conditions gives

$$W = 3\,M_0\,(2\eta\,\tau t - t^2 - \eta\tau^2)\,/2mL^2 \qquad (3.54)$$

$$\dot{W} = 3\,M_0\,(\eta\,\tau - t)\,/mL^2 \qquad (3.55)$$

The beam reaches it final position when $\dot{W} = 0$ as there is no elastic unloading for a perfectly plastic material. This occurs when $T = \eta\tau$ according to eq. (3.54). The final deformation profile can then be given by

$$w = 3\eta(\eta - 1)M_0\tau^2(1 - x/L)/2mL^2 \qquad (3.56)$$

3.3.2.3 Static Admissibility

The above analysis stratifies the initial conditions, boundary conditions and equilibrium equations but it is necessary to check that the bending moment does not violate the yield conditions anywhere along the length of the beam. If eq. (3.49) is rewritten using eq. (3.50) as

$$M/M_0 = 1 - \eta(x/L)^2 + (\eta - 1)(3 - x/L)(x/L)^2/2 \quad (3.57)$$

it can be seen that dM/dx = 0 for x = 0. Also

$$(L^2/M_o)d^2M/dx^2 = \eta - 3 - 3(\eta - 1)x/L \quad (3.58)$$

which gives $d^2M/dx^2 \geq 0$ as long as $\eta \leq 3$. This means the analysis is statically admissible provided $\eta \leq 3$ or $p_c \leq p_0 \leq 3p_c$. For pressures above $3p_c$ the solution is incorrect and a new velocity profile must be found that satisfies all the conditions.

3.3.3 Dynamic Collapse of a Simply Supported Beam for $p_o \geq 3p_c$

In order to obtain the correct solution in this case it is necessary to create a different transverse velocity profile. The yield violations in the previous analysis can give valuable hints as to a correct shape for this profile. Equation (3.58) with $\eta \geq 3$ and $x = 0$ is positive which implies that a local minimum develops in the bending at the mid-span. This suggests the velocity profile shown in figure 3.8 where plastic hinges form at $x = \pm\zeta_0$ and T_1 is the time at which the travelling plastic hinges meet at the midpoint and become stationary.

3.3.3.1 First Phase of Motion

The transverse velocity field is given by

$$\dot{w} = \dot{W}_1, \qquad 0 \leq x \leq \zeta_0 \quad (3.59a)$$

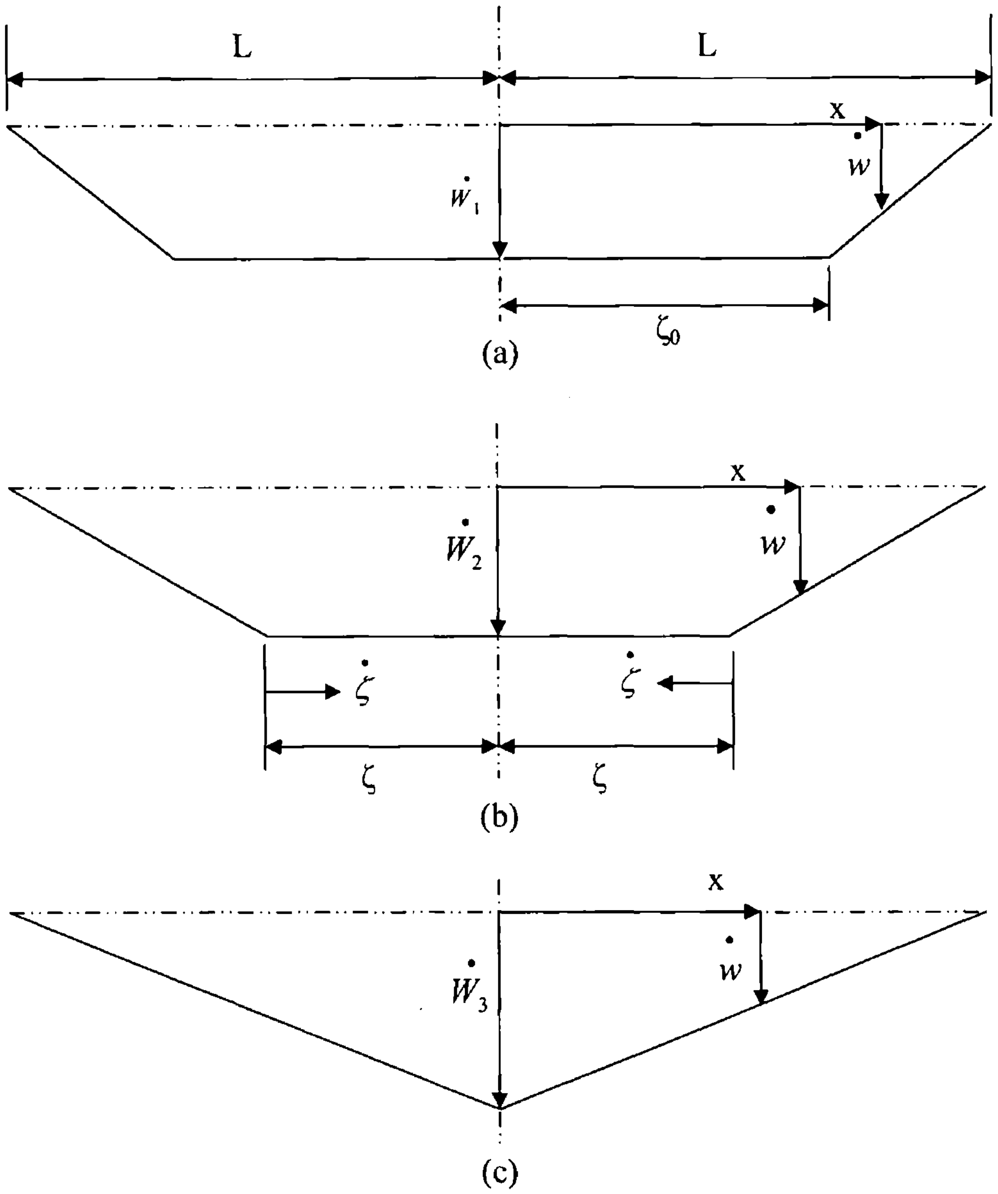

Figure 3.8: Transverse velocity profile for a simply supported beam with subject to a pressure load greater than $3p_c$. (a) First Phase of motion, $0 \le t \le \tau$. (b) Second Phase of motion $\tau \le t \le T_1$. (c) Third Phase of motion $T_1 \le t \le T$.

and

$$\dot{w}=\dot{W}_1(L-x)/(L-\zeta_0), \qquad \zeta_0 \le x \le L \text{ .... } (3.59b)$$

It is assumed the plastic hinge at $x = \zeta_0$ remains stationary for the first phase of motion. According to the equilibrium equations (3.42-3.44) and the first part of the velocity profile (3.59a) it can then be shown that

$$\partial^2 M / \partial x^2 = -p_0 + m d^2 W_1 / dt^2, \qquad 0 \le x \le \zeta_0 \ldots\ldots\ldots\ldots\ldots\ldots\ldots (3.60)$$

which when integrated with respect to x gives

$$\partial M / \partial x = (-p_0 + m d^2 W_1 / dt^2) x \ldots\ldots\ldots\ldots\ldots\ldots\ldots\ldots (3.61)$$

However since $\partial M / \partial x = Q = 0$ at the plastic hinges we get

$$M = M_0 \ldots\ldots\ldots\ldots\ldots\ldots\ldots\ldots\ldots\ldots\ldots\ldots (3.62)$$

when it is integrated further.

Now for the second part of the velocity profile (3.59b) and according to the equilibrium equations (3.42-3.44)

$$\partial^2 M / \partial x^2 = -p_0 + m[(L - x)/(L - \zeta_0)] d^2 W_1 / dt^2, \qquad \zeta_0 \le x \le L \ldots\ldots \quad (3.63)$$

which when integrated becomes

$$\partial M / \partial x = -p_0 x + p_0 (Lx - x^2/2)/(L - \zeta_0) + A_1 \ldots\ldots\ldots\ldots\ldots (3.64)$$

where $A_1 = p_0\zeta_0 - p_0\zeta_0(L - \zeta_0/2)/(L - \zeta_0)$ and when integrated again becomes

$$M = -p_0 x^2 + p_0 (Lx^2/2 - x^3/6)/(L - \zeta_0) + A_1 x + B_1 \ldots\ldots\ldots\ldots (3.65)$$

where $B_1 = p_0L^2/2 - p_0L^3/3(L - \zeta_0) - p_0\zeta_0L + p_0\zeta_0L(L - \zeta_0/2)/(L - \zeta_0)$.

Since we must satisfy the yield condition that $M = M_0$ at the plastic hinge it can be shown that

$$(1 - \overline{\zeta_0})^2 = 3/\eta \ldots\ldots\ldots\ldots\ldots\ldots\ldots\ldots\ldots\ldots\ldots (3.66)$$

where $\overline{\zeta_0} = \zeta_0/L$.

The bending moment distribution now becomes

$$M/M_0 = \eta \frac{3\overline{\zeta_0}\left(x/L\right)^2 - \left(x/L\right)^3 - 3\overline{\zeta_0^2}\left(x/L\right) + 1 - 3\overline{\zeta_0} + 3\overline{\zeta_0^2}}{3\left(1 - \overline{\zeta_0}\right)}, \quad \zeta_0 \leq x \leq L \ldots\ldots \qquad (3.67)$$

From equation (3.61) and (3.62) it can be seen that $md^2W_1/dt^2 = p_0$ so integrating

$$dW_1/dt = p_0t/m \ldots\ldots \qquad (3.68)$$

and

$$W_1 = p_0t^2/2m \ldots\ldots \qquad (3.69)$$

3.3.3.2 Second Phase of Motion, $\tau \leq t \leq T_1$

In the second phase of motion the pressure load is removed and beam continues to be deformed by the remaining kinetic energy. The velocity profile is described as per figure 3.8(b) where the plastic hinges are assumed to be moving in towards the mid-span of the beam. $\dot{W}_1$ is replaced by $\dot{W}_2$ and $p_0 = 0$ for $0 \leq x \leq \zeta$ and therefore

$$d^2W_2/dt^2 = 0 \ldots\ldots \qquad (3.70)$$

$$dW_2/dt = p_0\tau/m \ldots\ldots \qquad (3.71)$$

$$W_2 = p_0\tau t/m - p_0\tau^2/2m \ldots\ldots \qquad (3.72)$$

The governing equation becomes

$$\partial^2 M / \partial x^2 = p_0\tau\left(\frac{L - x}{(L - \zeta)^2}\right)d\zeta / dt \ldots\ldots \qquad (3.73)$$

which when integrated becomes

$$\partial M/\partial t = p_0\tau\frac{(Lx - x^2/2)\dot{\zeta}}{(L-\zeta)^2} + A_2 \quad\text{.............................. (3.74)}$$

where $A_2 = -p_0\tau\zeta\frac{(L-\zeta/2)\dot{\zeta}}{(L-\zeta)^2}$ and integrating again gives

$$M = p_0\tau\frac{(L\zeta^2/2 - \zeta^3/6)\dot{\zeta}}{(L-\zeta)^2} + A_2\zeta + B_2 \quad\text{...................... (3.75)}$$

where $B_2 = -\frac{p_0\tau L^3\dot{\zeta}}{3(L-\zeta)^2} - A_2 L$. At the travelling plastic hinges M $=M_o$ so therefore from equation (3.75) it can be seen that

$$M_0 = -p_0\tau(L-\dot{\zeta})/3 \quad\text{.............................. (3.76)}$$

Therefore it can be shown that the bending moment distribution is

$$M/M_0 = \frac{\left[2 + 2x/L - x^2/L^2 - 6\left(\zeta/L - \zeta^2/2L^2\right)\right]\left(1 - x/L\right)}{2\left(1 - \zeta/L\right)^3} \quad\text{............ (3.77)}$$

3.3.3.3 Third Phase of Motion, $T_1 \leq t \leq T$

In the final phase of motion the plastic hinge remains stationary at the mid-span of the beam which results in $\zeta_0 = 0$ and $\dot{W}_1$ is replaced by $\dot{W}_3$. Equations (3.42-3.44) now give

$$\partial^2 M / \partial x^2 = m(1 - x / L)\ddot{W}_3 \ldots\ldots\ldots\ldots\ldots\ldots\ldots\ldots\ldots\ldots \quad (3.78)$$

which when integrated gives

$$\partial M / \partial x = m(x - x^2 / 2L)\ddot{W}_3 \ldots\ldots\ldots\ldots\ldots\ldots\ldots\ldots\ldots\ldots \quad (3.79)$$

and

$$M = m(x^2 / 2 + x^3 / 6L)\ddot{W}_3 + M_0 \ldots\ldots\ldots\ldots\ldots\ldots\ldots\ldots\ldots \quad (3.80)$$

As equation (3.80) needs to satisfy the simply supported boundary conditions it can be in the form

$$\ddot{W}_3 = -3M_0 / mL^2 \ldots\ldots\ldots\ldots\ldots\ldots\ldots\ldots\ldots\ldots\ldots\ldots \quad (3.81)$$

The transverse velocity can then be found by integrating

$$\dot{W}_3 = -3M_0 t / mL^2 + 3p_0 \tau / 2m \ldots\ldots\ldots\ldots\ldots\ldots\ldots\ldots\ldots \quad (3.82)$$

and integrating again the transverse displacement is given by

$$W_3 = -3M_0 t^2 / 2mL^2 + 3p_0 t\tau / 2m - p_0 \tau^2 / 2m - p_0^2 L^2 \tau^2 / 24mM_0 \ldots\ldots \quad (3.83)$$

Finally the bending moment distribution, from equation (3.81), is given by

$$M/M_0 = 1 - (3x^2/L^2 - x^3/L^3)/2, \qquad \text{for } 0 \le x \le L \ldots\ldots\ldots\ldots\ldots\ldots \quad (3.84)$$

The static and kinematic admissibility of the above solution can be proved similar to section 3.3.2.3 [43].

3.3.4 Considerations for the Dynamic Collapse of a Plate

The same basic procedure developed for beams in the previously section will be used for the analysis of the dynamic collapse of plates. When considering the dynamic collapse of a rectangular plate it is found that the governing equations are

$$\partial Q_x / \partial x + \partial Q_y / \partial y + p = \mu \ddot{w} \qquad (3.85)$$

$$\partial M_x / \partial x + \partial M_{xy} / \partial y - Q_x = 0 \qquad (3.86)$$

$$\partial M_y / \partial y + \partial M_{xy} / \partial x - Q_y = 0 \qquad (3.87)$$

$$\kappa_x = -\partial^2 w / \partial x^2 \qquad (3.88)$$

$$\kappa_y = -\partial^2 w / \partial y^2 \qquad (3.89)$$

$$\kappa_{xy} = -\partial^2 w / \partial x \partial y \qquad (3.90)$$

The principal bending moments are now given by

$$M_1 = (M_x + M_y)/2 + \sqrt{(M_x - M_y)^2 + 4M_{xy}^2}\,/2 \qquad (3.91)$$

$$M_1 = (M_x + M_y)/2 - \sqrt{(M_x - M_y)^2 + 4M_{xy}^2}\,/2 \qquad (3.92)$$

where M$_x$, M$_y$ and M$_{xy}$ are defined in figure 3.9 below.

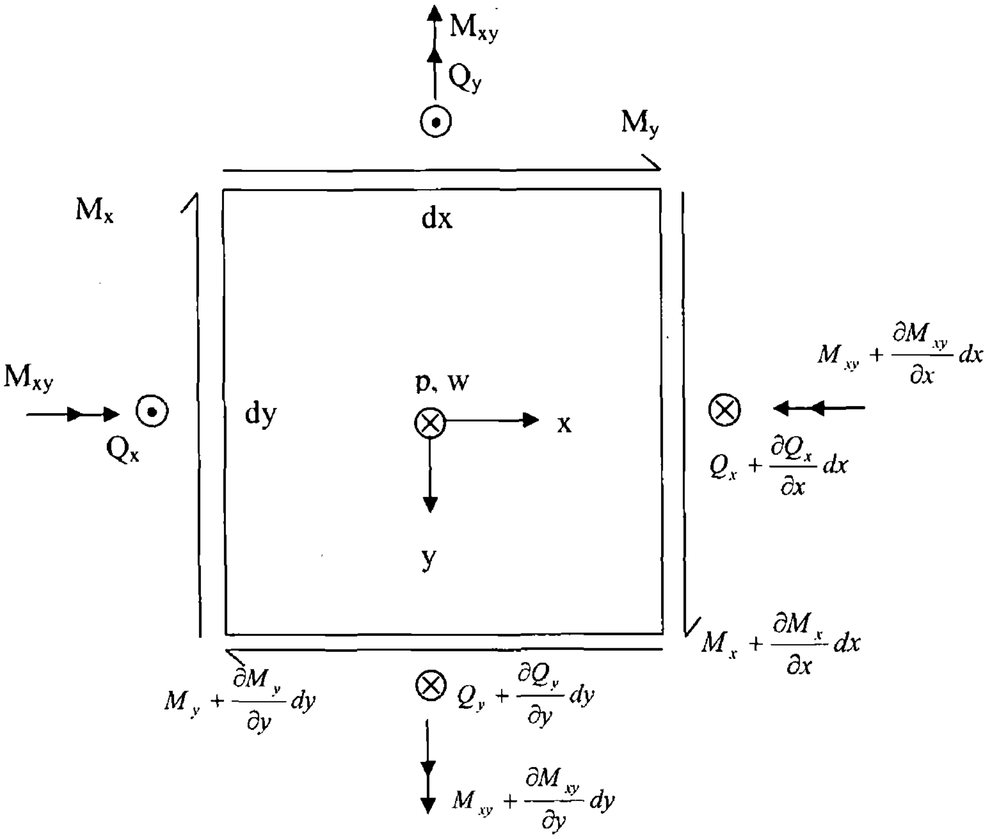

Figure 3.9: Infinitesimal element (dx dy) of a rectangular plate.

3.3.5 Dynamic Collapse of a Simply Supported Plate

3.3.5.1 First Phase of Motion, $0 \leq t \leq \tau$

Transverse motion commences when the pressure load exceeds the static collapse pressure p_c and it is assumed that transverse velocity profile, figure 3.10, is the same as in the static case. Therefore

$$\dot{w} = \dot{W}_1 (1 - z), \qquad 0 \leq z \leq 1 \ldots\ldots\ldots\ldots\ldots\ldots\ldots \text{(3.93)}$$

where $z = {}^{x+y}\!\!\Big/\!{}_{\sqrt{2}L}$.

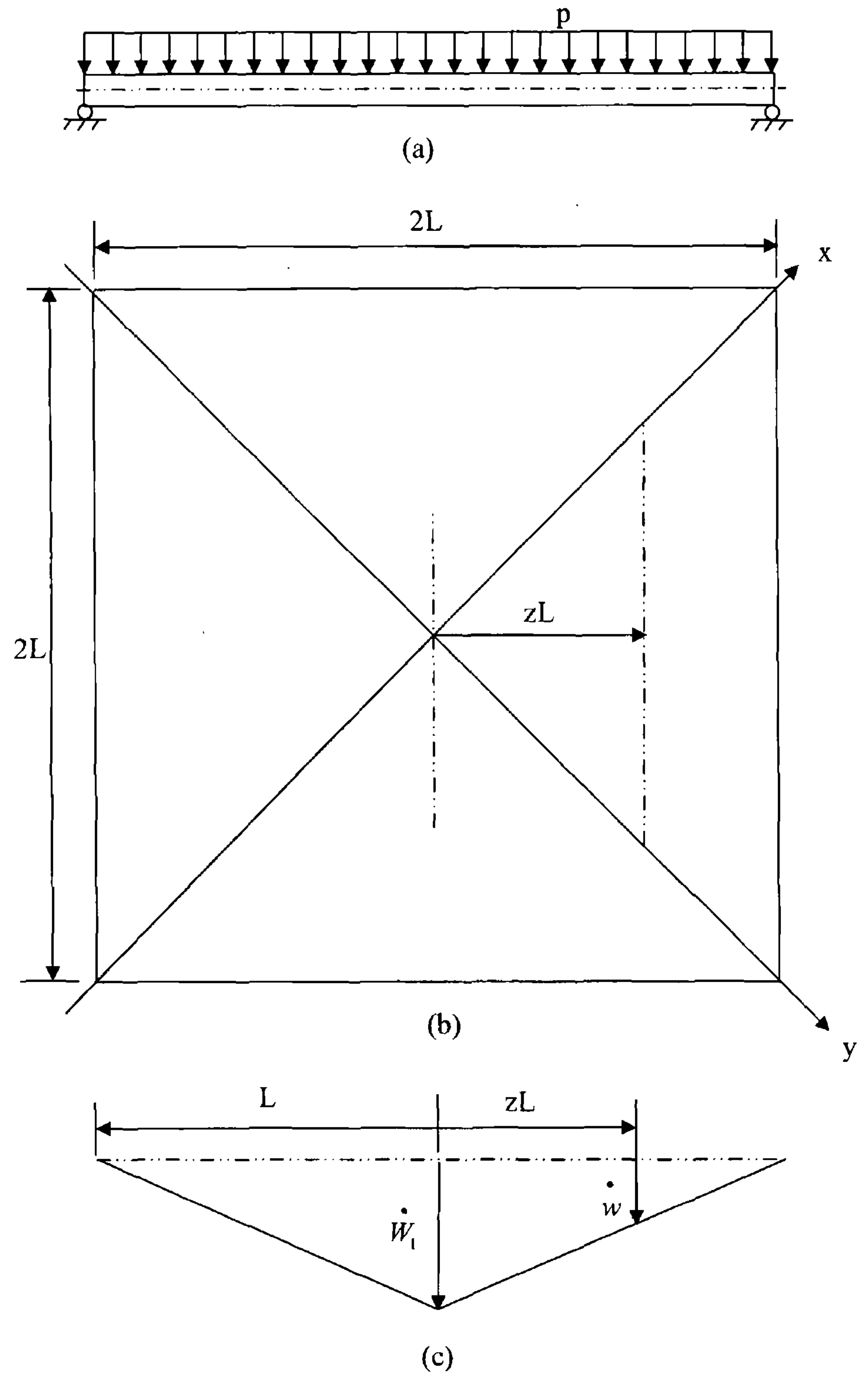

Figure 3.10: Simply supported square plate subjected to a uniformly distributed load. (a) Side view of square plate. (b) Plan view of square plate. (c) Transverse velocity profile

From the equilibrium equations (3.85.-3.88) and using p = p$_0$ and the transverse velocity profile it is possible to show that

$$\partial^2 M_x / \partial x^2 + 2\partial^2 M_{xy} / \partial x \partial y + \partial^2 M_y / \partial y^2 = \mu \ddot{W}_1 (1 - z) - p_0 \ \text{.......} \ (3.94)$$

From symmetry considerations it can be shown that $M_x = M_y = M_0$ and $M_{xy} = 0$ at the centre of the plate and along the plastic hinges it can be shown that

$$M_y = M_0 \text{ when } y = 0 \text{ and } 0 \leq x \leq \sqrt{2}L \ \text{......................} \ (3.95)$$

and

$$M_x = M_0 \text{ when } x = 0 \text{ and } 0 \leq y \leq \sqrt{2}L \ \text{......................} \ (3.96)$$

Thus from the Johansen yield condition it can be shown that

$$M_1 = (M_x + M_y)/2 + \sqrt{(M_x + M_y)^2 + 4M_{xy}^2}/2 = M_0 \ \text{............} \ (3.97)$$

$$-M_0 \leq M_1 = (M_x + M_y)/2 - \sqrt{(M_x + M_y)^2 + 4M_{xy}^2}/2 \leq M_0 \ \text{............} \ (3.98)$$

Simplifying, these equations can be written

$$M_x = M_0 + x^2 f_1(z) \ \text{.................................} \ (3.99)$$

$$M_y = M_0 + y^2 f_1(z) \ \text{.................................} \ (3.100)$$

$$M_{xy} = xy f_1(z) \ \text{...................................} \ (3.101)$$

where $f_1 = (\mu \ddot{W}_1 - p_0)/6 - \mu \ddot{W}_1 z/12$.

The simply supported boundary condition requires that

$$(M_x + M_y)/2 + M_{xy} = 0, \qquad z = 1 \ \text{..................} \ (3.102)$$

thus substituting in equations (3.99-3.101) gives

$$\mu \ddot{W}_1 = 2(p_o - p_c) \ldots\ldots \tag{3.103}$$

Integrating with respect to time gives the transverse velocity

$$\dot{w} = 2(p_0 - p_c)\tau(1 - z)/\mu \ldots\ldots \tag{3.104}$$

and the transverse displacement

$$w = 2(p_0 - p_c)t^2(1 - z)/\mu \ldots\ldots \tag{3.105}$$

3.3.5.2 Second Phase of Motion

When the pressure pulse is removed from the plate at t = τ the remaining kinetic energy in the plate results in a second phase of motion where the energy is dissipated plastically. The transverse velocity profile remains the same

$$\dot{w} = \dot{W}_2(1 - z) \ldots\ldots \tag{3.106}$$

but p = 0 for t ≥ τ. Therefore the governing equation can now be written

$$\partial^2 M_x / \partial x^2 + 2\partial^2 M_{xy} / \partial x \partial y + \partial^2 M_y / \partial y^2 = \mu \ddot{W}_2(1 - z) \ldots\ldots \tag{3.107}$$

Equations (3.99-3.101) remain valid with f_1 replaced by $f_2 = \mu \ddot{W}_2/6 - \mu \ddot{W}_2\, z/12$. Thus the simply supported boundary condition yields

$$\mu \ddot{W}_2 = -2p_c \ldots\ldots \tag{3.108}$$

and integrating with respect to time gives

$$\dot{W}_2 = 2(p_0\tau - p_c t)/\mu \quad (3.109)$$

$$W_2 = -p_c t^2/\mu + 2p_0 t\tau/\mu - p_0\tau^2/\mu \quad (3.110)$$

3.3.5.3 Static Admissibility

It may be shown by substituting equations (3.99-3.101) and equation (3.103) into equation (3.97) that $M_l = M_0$, $0 \leq z \leq 1$which satisfies equation (3.97) for the first phase of motion. Similarly substituting in equations (3.99-3.101) into the inequality (3.98) results in

$$-M_0 \leq M_0 + (x^2 + y^2)f_1(z) \leq M_0 \quad (3.111)$$

which can be rearranged into the form

$$-2 \leq (x^2 + y^2)[\eta - 2 - (\eta - 1)z]/L^2 \quad (3.112)$$

which shows a yield violation at the plate centre when $\eta \geq 2$. Thus a different velocity profile is required for loads greater than $2p_c$ similar to the beam outlined in section 3.3.3.

3.4 Effects of finite displacements

In the previous sections it was assumed that the displacements that the elements of the beams or plates were undergoing were infinitesimal. The equilibrium equations were developed for the undeformed shape and ignored any change in shape during an impact event. This method has proved to be accurate in many cases and has been verified by experimental testing. However, it is evident that if the change in geometry is not ignored then the previous equilibrium equations fail to describe the problem. The membrane force shown in figure 3.11 turns out to be the most important development of a finite displacement.

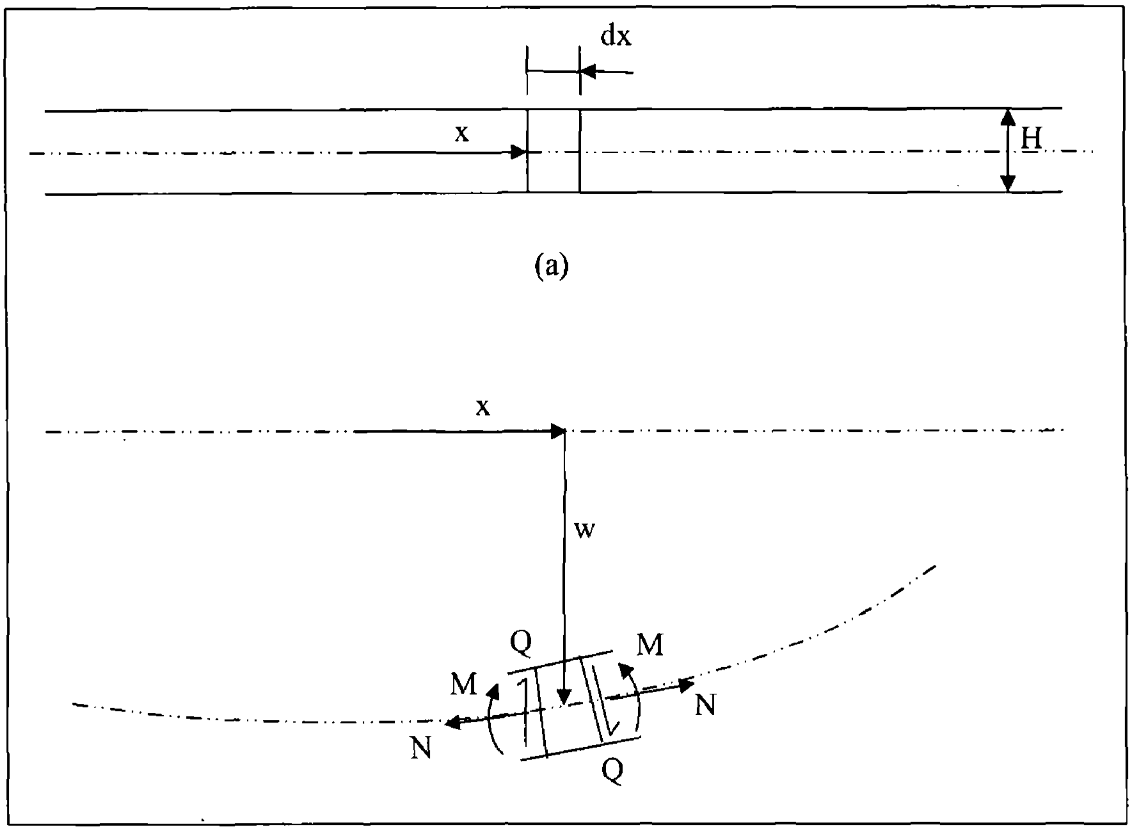

Figure 3.11: Element of a beam. (a) Initial Shape. (b) Shape after deformation

The centre line of the beam must be longer when the beam with axial restraints is deformed and this deformation creates an axial membrane strain and the membrane force N shown in figure 3.11. As seen in section 3.2.1 the equilibrium of a beam with infinitesimal displacements is governed by a bending moment M and a shear force Q but when transverse displacements are considered a third force, the membrane force N must be considered. As the transverse displacement increases so does the effect of the membrane force until the other forces become negligible themselves. This is known as a string response and at this point a beam made from perfectly plastic material will flow plastically at the fully plastic membrane force N_0 for the cross-section. Similar geometry changes can also occur during the static and dynamic responses of plates and have similar effect on their equilibrium equations. No general theorems have been developed for finite displacement analysis of beams and plates that are of interest here but some have been obtained for special cases and have good correlation with experimental results [44].

3.5 Strain Rate Effects

In the previous sections it has been assumed that the plastic flow in the structures were independent of strain rate. However, for many materials this is not the case. This is known as strain rate sensitivity or viscoplasticity. Figure 3.12 below shows a graph of mild steel subjected different strain rates during tensile tests.

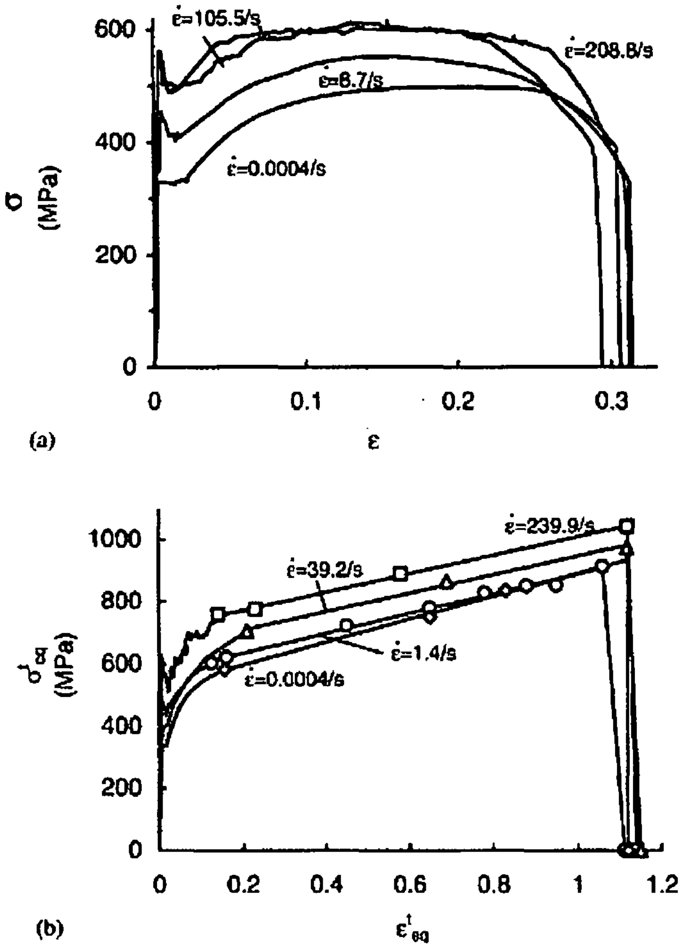

Figure 3.12: (a) Engineering and (b) equivalent true stress–strain curves for the mild steel at several strain rates [45]

From figure 3.12 it is evident that mild steel has a high sensitivity to strain rate. Some materials are sensitive to a lesser extent or not at all and often experimentation is needed to provide accurate data for a range of different strain rates. Stain rate sensitivity is a material effect and the geometry of the object has no effect with regard to it. The influence of strain rate sensitivity is that of a strengthening effect and so it is often taken as an extra safety factor in design.

3.5.1 Cowper-Symonds Constitutive Equation

There has been a lot of research undertaken to find constitutive equations that describe the strain rate sensitivity of materials resulting in many different equations. Experimental work is needed to generate the coefficients needed for these equations and in some cases this can be extensive. Even then there is still much debate on the accuracy of the models. One equation that is popular is the Cowper-Symonds constitutive equation because of its simplicity. The Cowper-Symonds equation states

$$\dot{\epsilon} = D\left(\frac{\sigma_0'}{\sigma_0} - 1\right)^q \text{ .... } (3.113)$$

where σ_0' is the dynamic flow stress at a uniaxial plastic strain rate $\dot{\epsilon}$, σ_0 is the associated static flow stress, and D and q are constants of a particular material. If values of D = $40.4s^{-1}$ and q = 5 are used close agreement to the graph in figure 3.12 is seen for mild steel.

3.6 Early Time response/Near Contact Phenomenon

The near contact phenomena of an impact to a plate structure are concerned with the deformation immediately around the region in which the impact occurs. They occur within the same order of time taken for a stress wave to propagate through the plate which can generally be measured in microseconds. Thus they are also known as the early time response of the structure. Some of the factors which affect the behavior of this response include the speed and angle of impact, the shape of the projectile, the material properties of the plate and of the projectile and the ratio of the projectile diameter to the plate thickness [38].

As already mentioned the shape of the projectile, or more correctly the projectile nose shape, is a major consideration when try to predict impact behaviour. There are three categories of projectiles recognized:

1. ogival and the conical ended circular cylinder,
2. the square ended circular cylinder and
3. spherical

It should be noted that the deformations described are due to normal impact of the projectile and that impact at an angle can cause changes in this behavior. The velocities of the projectile range from 50m/s to 1000m/s for penetration behavior. Impacts above these speeds are known as transvelocity and hypervelocity impacts and have distinct properties.

Conical-ended, ogival and to some extent spherical projectiles all have similar behavior starting by indentation of the plate. With ductile materials this indentation is accompanied by a coronet around the impact site, see figure 3.13. With brittle materials the behavior includes fractures immediately under the projectile. As a result of the high strain rates brittle behavior is more commonly observed when dealing with penetration analysis. As the conical-ended or ogival projectile, penetrates further the mode of deformation changes. The metal is now pushed radially outwards resulting in radial compression of the material involved.

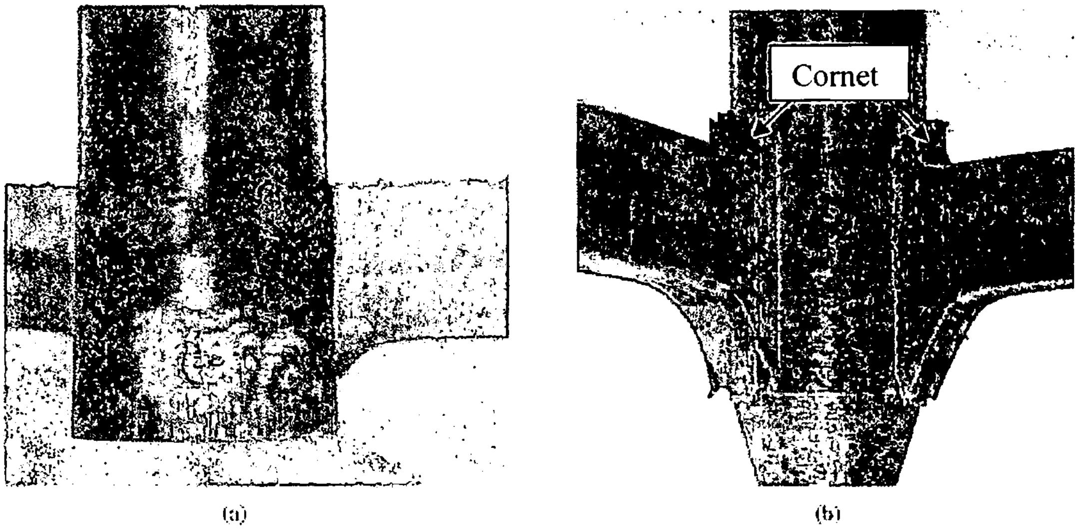

Figure 3.13: (a) Impact of square-ended projectile causing plugging. (b) Impact of conical projectile with a cornet at the impact site and some petalling. [12]

Finally, sometimes accompanied by spalling cracks, the bottom layers are dished, fractured and bent downwards as the projectile penetrates the plate. There is often petalling of the material if it is ductile. The behavior of the plate during impact with a square-ended projectile, see figure 3.14, and in some cases ball projectiles, is quite different from that of an ogival projectile. In these cases a plug is punched from the plate with cracks being formed parallel to and ahead of the projectile as it penetrates. There is also the possibility that one side of the plug will remain attached and will result in the petalling effect. The plug diameter is usually equivalent to that of the projectile and is usually dished shaped. This is because it tends to be forced out at high velocity, but with the edges restrained they are held back while the centre progresses. The inertia of the plug plays a significant role during the impact event as do the strength properties of the plate. From experiments [38] it is seen that the plug and the projectile have almost the same velocity at the moment of separation from the plate. The velocity of the plug and projectile v_r can be given by

$$v_r = v_0^2 - v_b^2 / 1 + m_s/m_p \ldots\ldots\ldots\ldots\ldots\ldots\ldots\ldots \quad (3.114)$$

where v_0 is the initial projectile velocity, v_b is the ballistic velocity just sufficient to cause ejection of the plug, m_s is the mass of the plug and m_p the mass of the projectile.

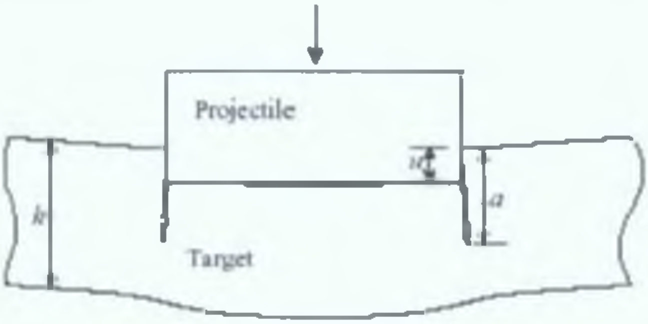

Figure 3.14: Square-ended projectile causing plugging in plate [46]

3.7 Summary of Chapter 3

This chapter concerned the theory of impact mechanics specifically with impact on thin plates in mind. A study was made of the theory of plastic deformation and near contact phenomena causing failure.

4. Analysis of Simple Plate Structures

4.1 Introduction

This chapter concerns the experimental and computational analysis of a simple sheet metal aircraft structure subject to high energy impact. The idea is to gain in-depth understanding of this simple problem to facilitate analysis of more complex structures. Experimental testing was carried out using an existing gas powered projectile launcher. Thin aluminium plates were impacted at velocities up to 150m/s with a titanium projectile. Computer simulations were then carried out using the Ansys/Ls-Dyna software attempting to reproduce the impact event accurately.

4.2 Experimental Testing

4.2.1 The Experimental Test Set-up

As mentioned above experimental testing was undertaken to allow for validation for the finite element model and to provide knowledge in its own right. It was carried out using an existing impact testing rig, shown in figure 4.1, which had been modified for the purpose [48]. Aluminium plates $150mm^2$ were clamped on two 28mm strips on each side. The idea of using smaller strips to conserve material was considered but it was found that the clamping mechanism was insufficient and the plates slipped when impacted. The plates used were 1mm thick 2014 T4 Aluminium. The projectile, which was a titanium (Ti-6Al-4V) cylinder 9mm in diameter and 19mm long, was placed in a 1m barrel and shot at the test plates. The projectile launcher was powered from a compressed nitrogen gas cylinder. A reservoir was filled with the gas and then released into the barrel by a solenoid valve. The projectile was thereby fired down the barrel at velocities up to 150m/s. The velocity of the projectile was measured as it exited the barrel by means of a laser and receiver. A timer measured the length of time the laser beam was broken and the velocity of the projectile could then be calculated by dividing the length of the projectile by the time taken for it to pass the laser.

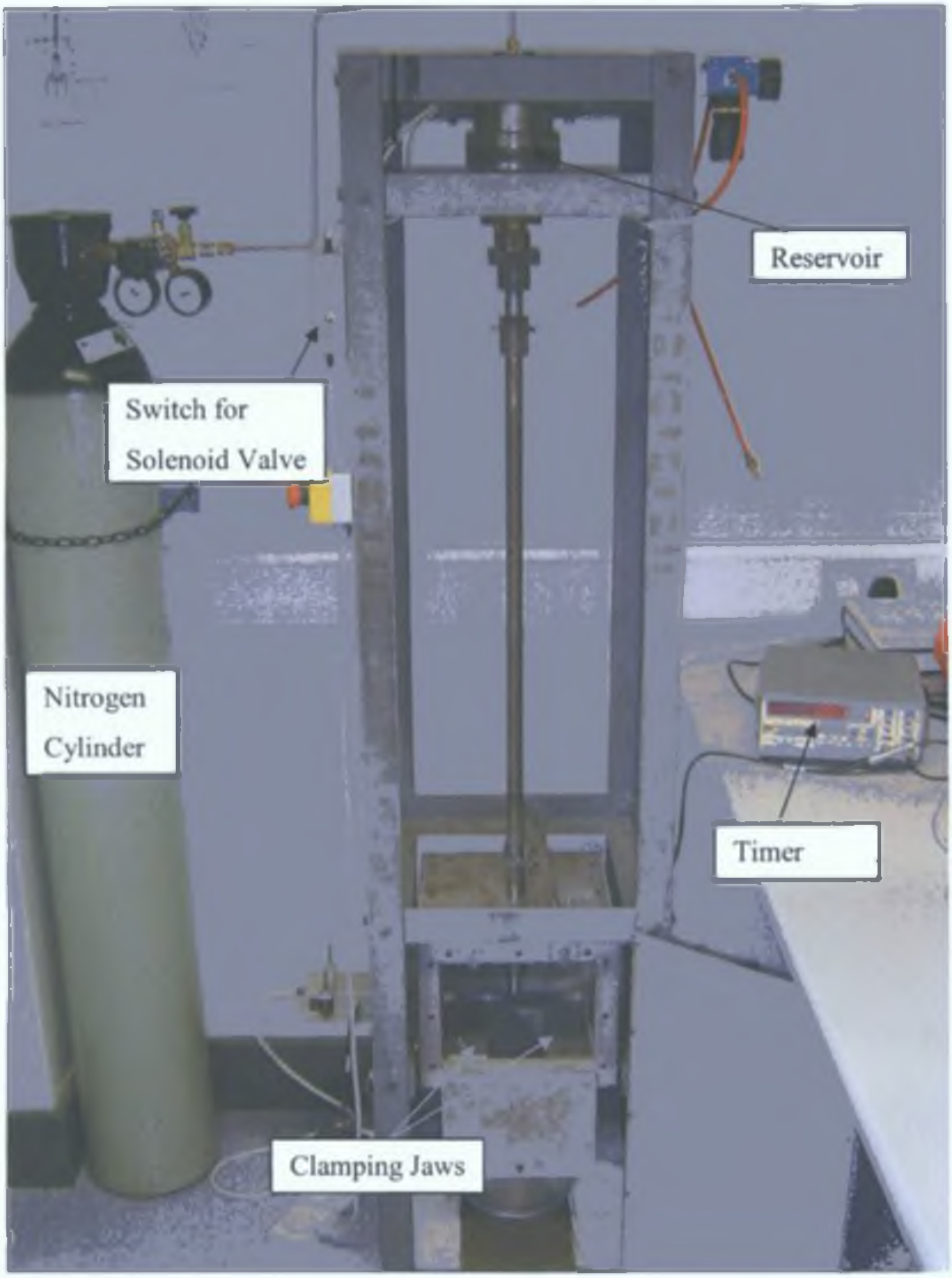

Figure 4.1: Gas powered projectile launcher

The projectile was caught either in the shielded box surrounding the clamping mechanism, if it failed to penetrate the plate, or in a bucket filled with cloth to absorb the impact if it penetrated the plate. This whole area was sealed off by aluminium plate during operation for safety.

4.2.2 Initial Testing

Tests were performed at a range of velocities from 50m/s to 150m/and it was noted that for most of the velocities the tests were very repeatable with regard to the deformation of the plate. Below approximately 90m/s the plate would deform slightly with a dishing in the centre where the projectile impacted. Above approximately 130m/s a plug was ejected from the plate more or less the same diameter as the projectile, again with dishing of the plate around the impact site and slight deformation of the plate in other areas. However, between 90m/s and 130m/s, the behaviour of the plate was much more complex and the results less repeatable. This was the range of velocities surrounding the ballistic velocity of the plate, the velocity at which the plate was perforated by the projectile, and because of these variations it was decided to concentrates the analysis on velocities in this region.

4.2.3 Ballistic Velocity Testing

A series of further tests were thus undertaken at velocities around the ballistic velocity. For this case the ballistic velocity was taken to be the velocity needed to obtain any perforation of the plate by the projectile. Twenty plates were tested at velocities between 90m/s and 130m/s. A 10mm^2 grid was drawn on the plates to help identify the damage. Three distinct groups of damage were noted

- No perforation (figure 4.2)
- Perforation without completed penetration of the plate (figure 4.3)
- and complete penetration of the plate by the projectile (figure 4.4)

The first occurred mostly in the 90m/s-100m/s range but also in two other plates, one at 117m/s and the other at 119m/s. The second case occurred at a low of 99.7m/s but other wise was confined to the 115m/s-120m/s range. This perforation was accompanied by a petalling of the plate where the projectile hit. The final case occurred at velocities greater than 119m/s and the deformation was either petalling, as in the previous case, or plugging, as with the greater than 130m/s cases. However the hole in these cases also experienced some tearing with oblong holes noted in some of the cases.

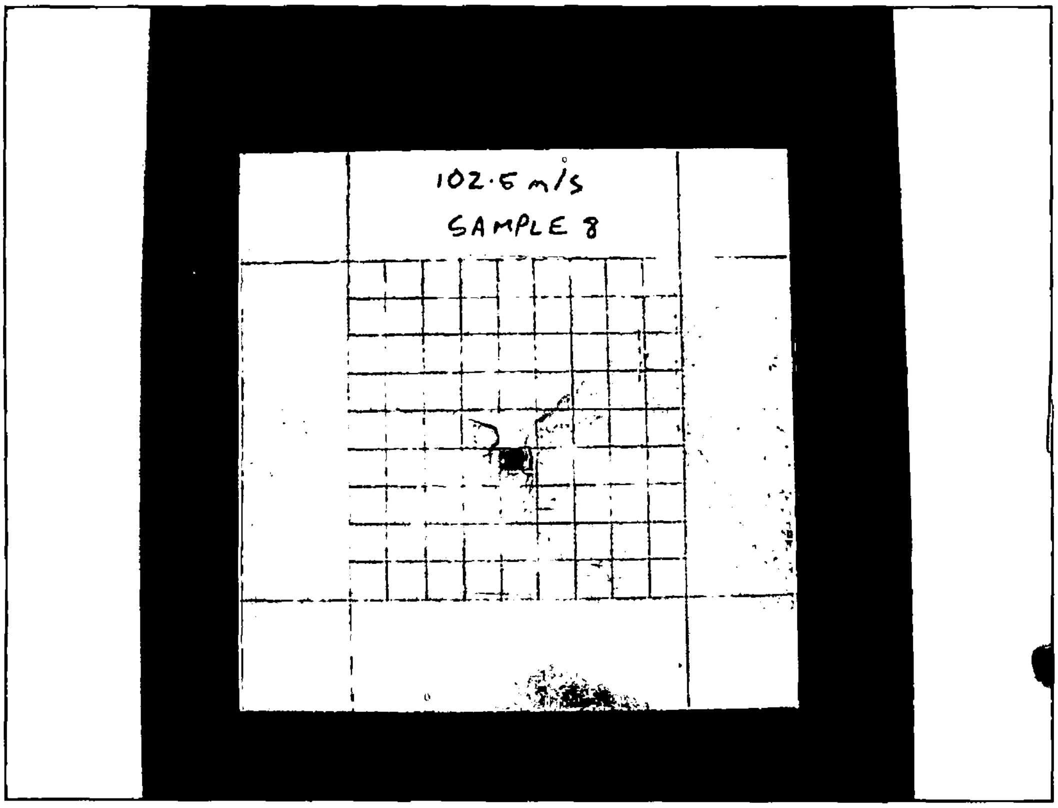

Figure 4.2: Case 1: No perforation of the plate

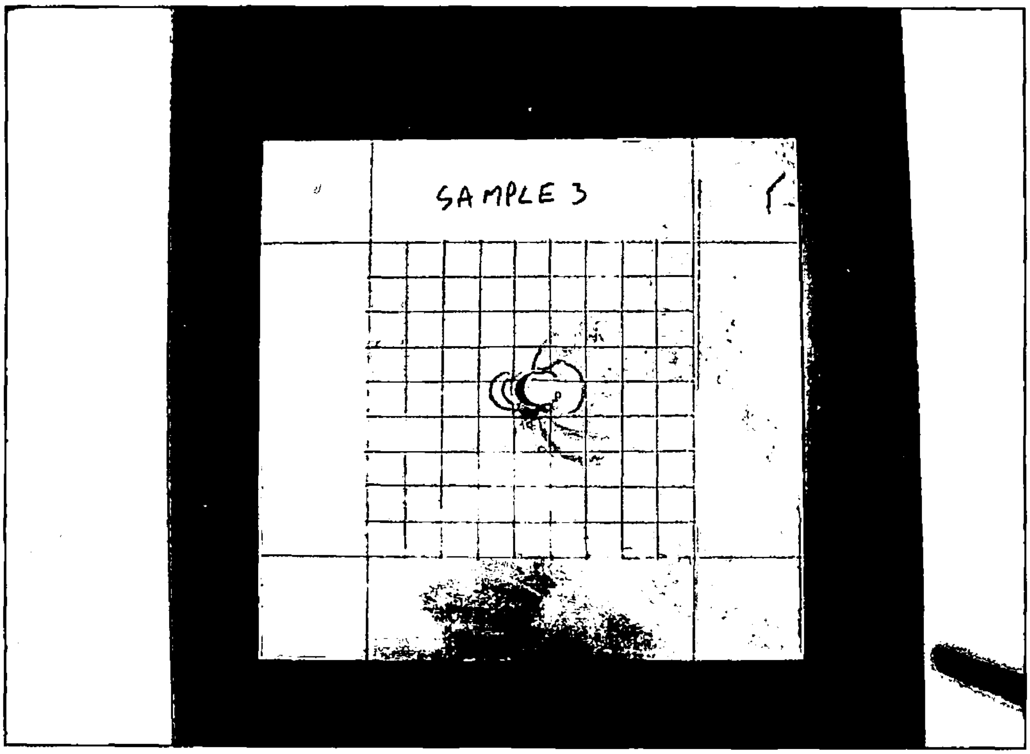

Figure 4.3: Case 2: Perforation and petalling of the plate

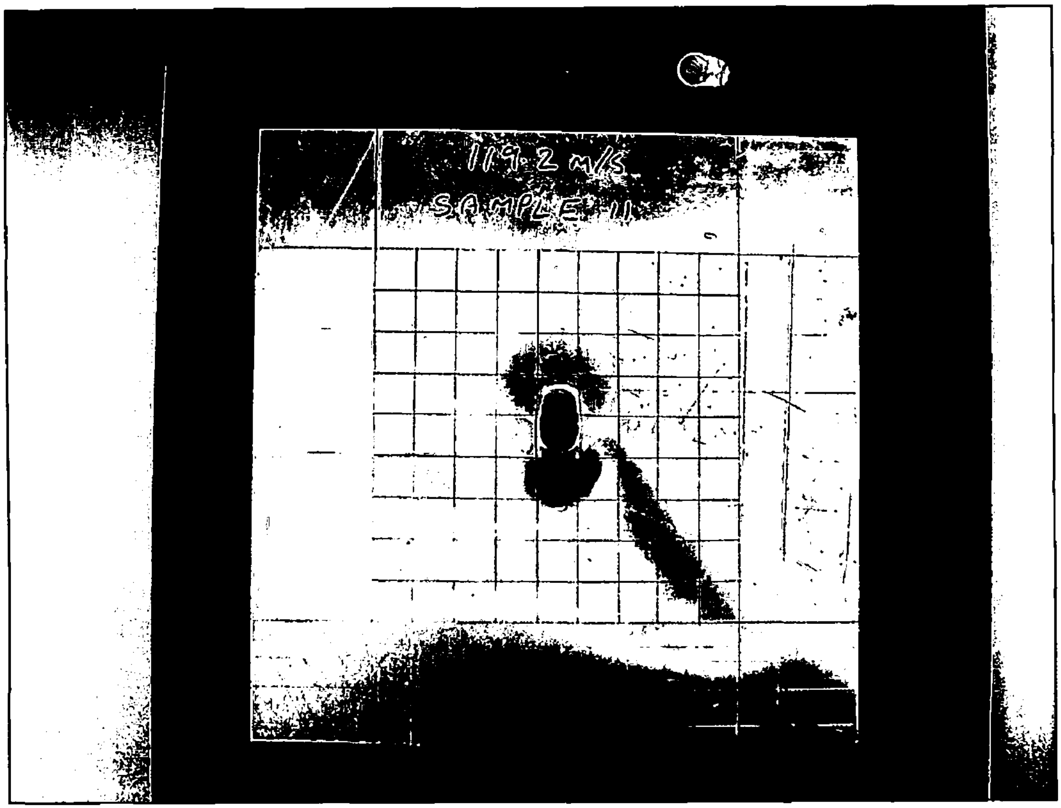

Figure 4.4: Case 3: Complete penetration of the plate with plugging

A measurement of the maximum deformation of the plate perpendicular to the plane of the plate was taken. Again it was noticed that the results were sorted into the three groups of no perforation, slight perforation and full penetration. For the second two groups the petal or plug was ignored and the measurements were taken from the edge of the hole. The results were averaged and are shown in table 4.1.

Table 4.1: Average plate deformations for the three categories

	Average height of deformation at hole (mm)
No perforation	5.2
Slight Perforation	5.7
Full Penetration	6.2

4.3 Modelling the Simple Plate

The software package used for the finite element modelling and solution was Ansys/Ls-Dyna which was chosen because of previous experience with Ansys, its proven ability to solve dynamic problems [9] and its availability. Ansys was used initially for post-processing of the results but when the file became large it proved to be inadequate and LS-Prepost, the post-processor supplied with Ls-Dyna, was used subsequently. The computer hardware used was a 2.7Ghz Pentium IV with 512Mb of RAM. The parameters for the material model for the Al 2014 material were taken from the material specifications given by the supplier (see appendix 1) and the parameters for the titanium model were adapted from those used by Knight et al [9]. The parameters used are shown in table 4.2 below. The tangent modulus was calculated as a linear approximation between the yield stress and the ultimate tensile stress on the stress-strain graph. The model is a non-linear plastic kinematic model. The stress-strain curve is essentially bilinear and is described by the Young's modulus and the tangent modulus. The hardening parameter gives a combination of isotropic and kinematic hardening. The model on the left, representing the plate material Al 2014 T4, also has a failure strain specified at which point the elements in the

Table 4.2: (left) Material model for Al2014 T4. (right) Material Model for Ti-6Al-4V

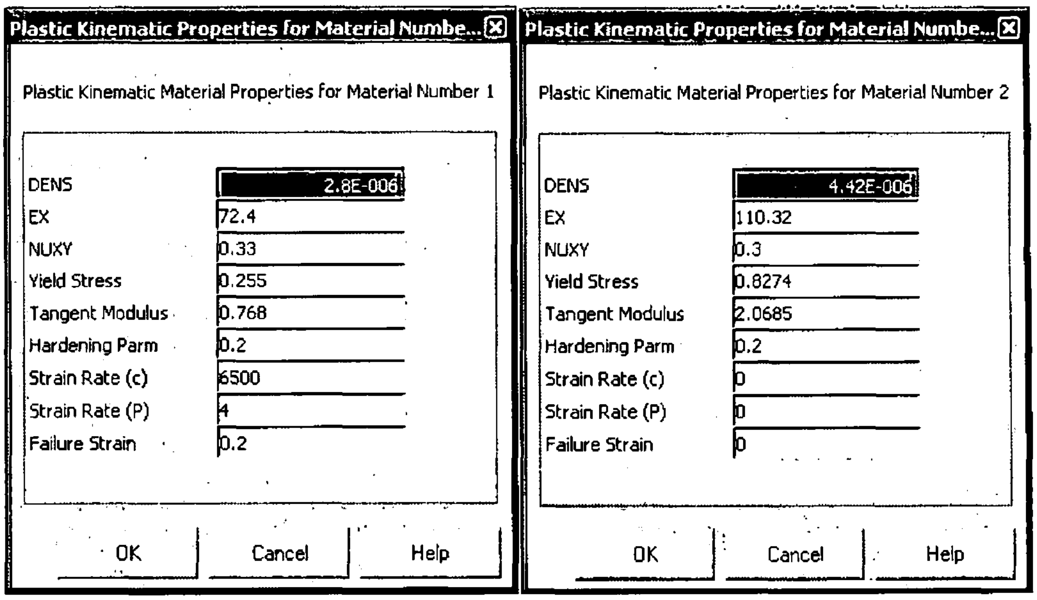

Plastic Kinematic Material Properties for Material Number 1

DENS	2.8E-006
EX	72.4
NUXY	0.33
Yield Stress	0.255
Tangent Modulus	0.768
Hardening Parm	0.2
Strain Rate (c)	6500
Strain Rate (P)	4
Failure Strain	0.2

Plastic Kinematic Material Properties for Material Number 2

DENS	4.42E-006
EX	110.32
NUXY	0.3
Yield Stress	0.8274
Tangent Modulus	2.0685
Hardening Parm	0.2
Strain Rate (c)	0
Strain Rate (P)	0
Failure Strain	0

mesh concerned would fail. The titanium model does not need this parameter as it is not expected to fail. The models used by Knight et al [9] did not take strain rate sensitivity of the materials into account. Their effects are examined later in section 4.3.4. With a view to future, more complex, models that would need two contact surfaces it was decided to use solid 164 elements rather than shell elements to build the model. The geometry of the problem was created such that the projectile was offset from the plate by 1mm. This offset distance was chosen so that too much processor time was not wasted while the projectile was travelling through air before hitting the plate. The plate was initially meshed with 3600 brick elements, which included four elements through the thickness of the plate and 30 along either side, and the projectile was meshed with 76 brick elements. An eroding surface to surface contact algorithm was setup between the projectile and the plate. This algorithm allowed for deformation to occur to both the elements in the plate and the projectile up to the point where the failure strain was reached in an element, at which point it was eroded from the solution. Using this method allowed through thickness damage to occur in the plate. The projectile experienced little or no deformation due to its shape and superior stiffness. The nodes of the plates were constrained in all directions along two 28mm wide strips on opposite sides of the plate to simulate the clamping of the plate. A velocity, initially 90m/s, was then prescribed to nodes making up the projectile. At this velocity it was calculated that the projectile would take 0.01ms to reach the plate. As a result the solution time, the time at which the simulation would end, was set to 5ms as a "first guess" as to how long would be needed for the complete impact event to occur. However after the results of the first simulation were examined it was clear that all of the significant events occurred within a much shorter time frame. As a result further simulations were carried out using the more suitable solution time of 0.5ms.

4.3.1 Initial Results

As already mentioned above the initial velocity prescribed to the projectile in the simulation was 90m/s, the lower end of the range of velocities used in the experimental testing. The results of the simulation were encouraging with the plate being deformed in a similar fashion with a dish shaped indentation at the impact site. However, as already mentioned, this sort of deformation was the easiest to reproduce and so it was decided to find the ballistic velocity for the simulation. The velocity was increased in 10m/s increments until finally the ballistic velocity was reached at 150m/s, a value substantially larger than expected. Some elements had been eroded from the surface of the plate in simulations previous to this but this was the first simulation with through thickness damage, see figure 4.5 below.

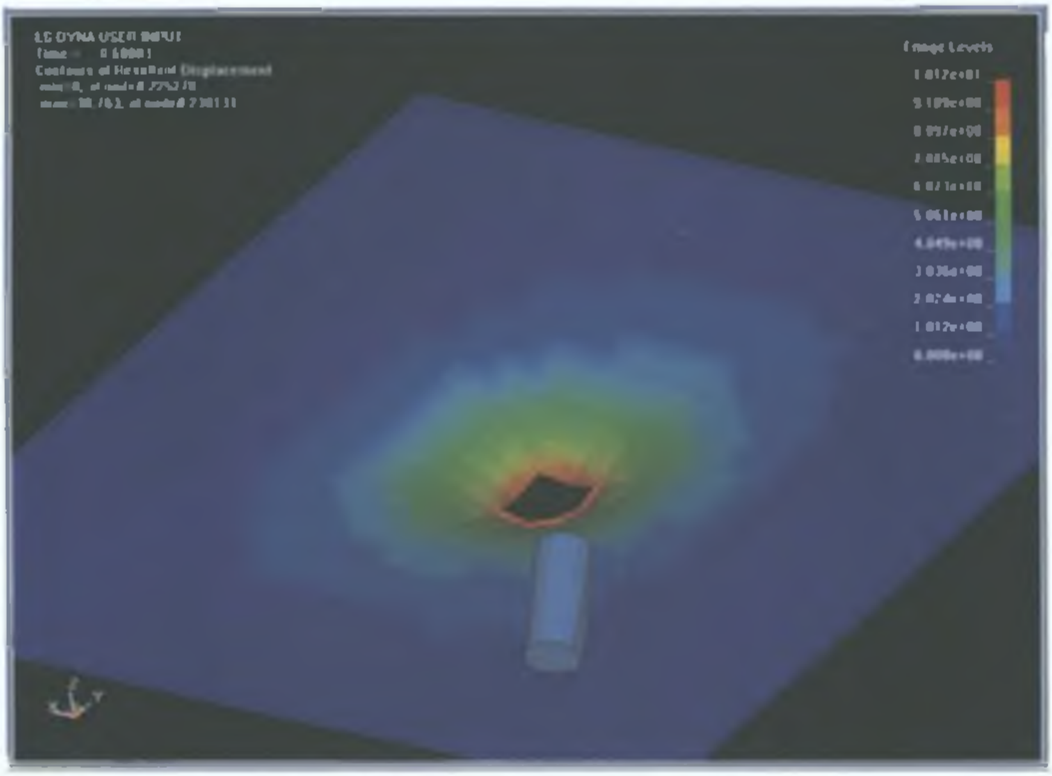

Figure 4.5: Plot of displacement in the z direction for the initial modelling of the problem

The shape of the deformation was also strange with the projectile penetrating the plate without any plug being ejected. The elements at the impact site had simply been eroded until enough had been eroded to allow the projectile to pass. While this showed some of the limitations of the contact algorithm it also suggested a denser mesh was needed to model the problem accurately.

4.3.2 Examination of Mesh Convergence

It is widely accepted that there is a convergence in the results of a linear finite element model as the mesh density is increased and that to obtain an accurate solution this convergence should be sought [49]. An example of an inaccurate solution was presented in the section above where although the geometry and loading conditions of the problem were correct the lack of adequate mesh density caused the solution to be inaccurate. Often designers are content to accept the results of a simulation if they appear to be correct but, as will be seen in the following section, the solution which may look correct is not always the converged solution and while the unconverged solution may seem correct at the time it may prove to be unpredictable when loading conditions or other parameters are changed. It was assumed before beginning this investigation of mesh convergence that the accuracy of the solution would increase gradually, settling as the point of convergence was reached however what was experienced was more like an oscillation which decreased as convergence was reached as the results varied significantly as the mesh was refined. Several simulations whose results seemed to tally closely with the experimental observations were followed by models of greater mesh density with hugely different results.

The first aspect of the mesh density to be examined was the effect of the number of elements through the thickness of the plate. Previous literature [9,28] have put forward that a thickness of three or four elements is needed for accuracy and after some tests four was seen to be the best solution. After this the surface mesh was increased in a uniform manner by increasing the number of elements along each side of the plate to 50, 70, 90 etc. As the mesh density was increased the features of deformation seen in the experimental testing began to appear. At a surface mesh density of 70x70 the plate underwent pettaling as can be seen below in figure 4.6. The ballistic velocity at this point was quite reasonable, at 135m/s, when compared with the experimental results but as the mesh was increased again the solution changed considerably. After the petalling the deformed shape changed to plugging for ballistic impacts which penetrated the plate and remained so until convergence was achieved.

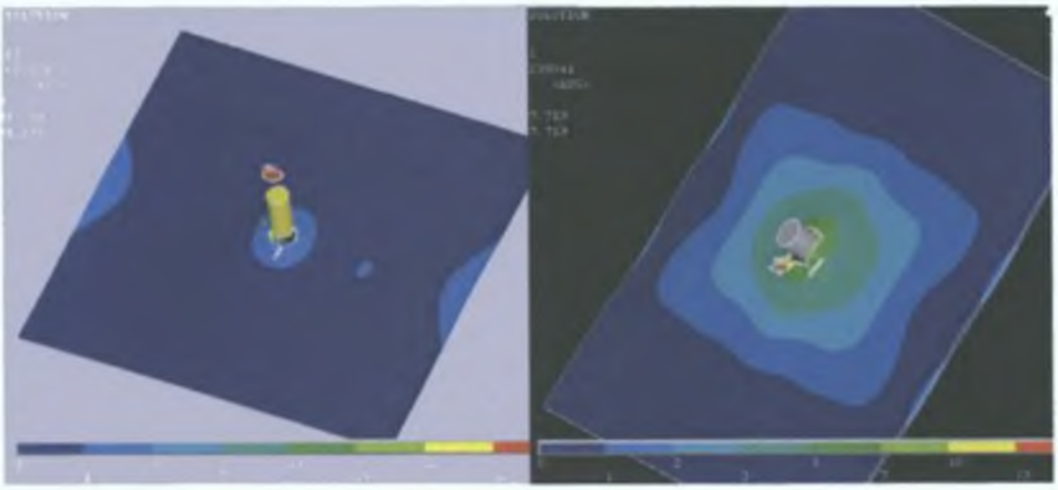

Figure 4.6: (left) Plugging of plate. (right) Petalling of plate

It was decided to use the ballistic velocity as the convergence factor and it settled eventually when the mesh density reached 155x155 for the surface of the plate, which gave a total of 96100 elements in the plate. Figure 4.7 shows a plot of the ballistic velocity plotted against an increasing number of elements. A steadier, more monotonic increase was expected as seen by Teng and Wierzbicki [35] (see figure 2.10) but it can still clearly be seen that the ballistic velocity settles at approximately 100m/s with the results of the last two simulations being almost identical and that the results of the previous simulations contained considerable errors.

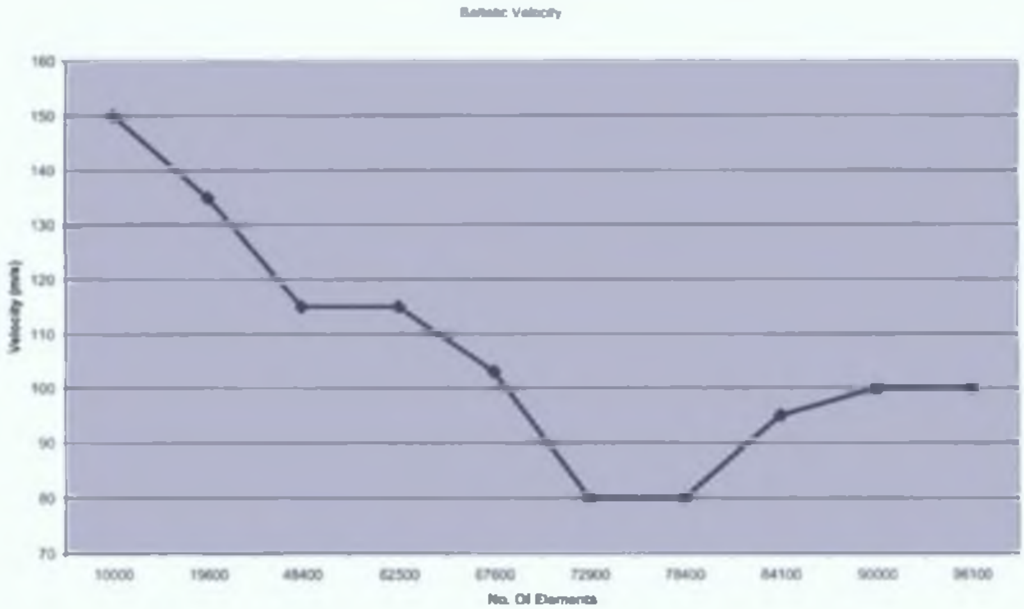

Figure 4.7: Graph of ballistic velocity vs. number of elements

Initially it was thought that the mesh density of the projectile was negligible due to its lack of deformation but when its density was varied it caused significant changes, increasing the ballistic velocity for the converged plate mesh. The converged projectile mesh was seen to have 355 elements.

4.3.3 Problems encountered during Modelling

The finite element analysis that was undertaken was a highly complex nonlinear simulation and predictably did not run smoothly the first time. Instabilities in the analysis meant that errors such as negative volume in elements were experienced. The solution to this was to decrease the timestep scale factor from the default of 0.9 to 0.7. This unfortunately also increased the solution time for the problem. The other major problem experienced was that of "no damage" penetration, see figure 4.8, of the plate by the projectile i.e. where the projectile would pass through the elements of the plate without coming into contact with them at all. This problem was related to the sliding interface energy part of the contact and was solved by increasing the sliding interface penalty factor (SIPF). However too high a value was also problematic as it could lead to inaccuracies.

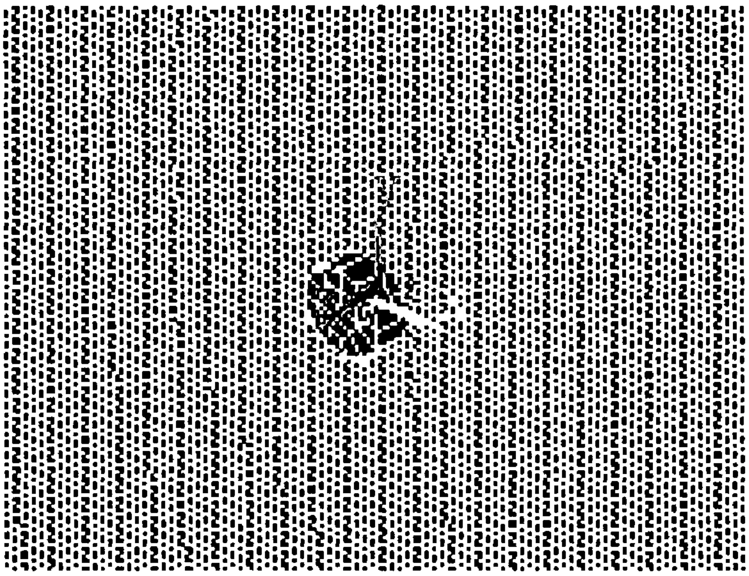

Figure 4.8: No damage penetration of projectile through plate

An investigation was made to find the lowest value that would prevent the no damage penetration to minimise the inaccuracies in the calculation. To prevent the no damage penetration it was necessary for the sliding interface energy in the problem to remain below zero. Tests were carried out with SIPF's between 0.001 and 0.1. The sliding interface energy in each case was recorded and the results were compared, see figure 4.9 below.

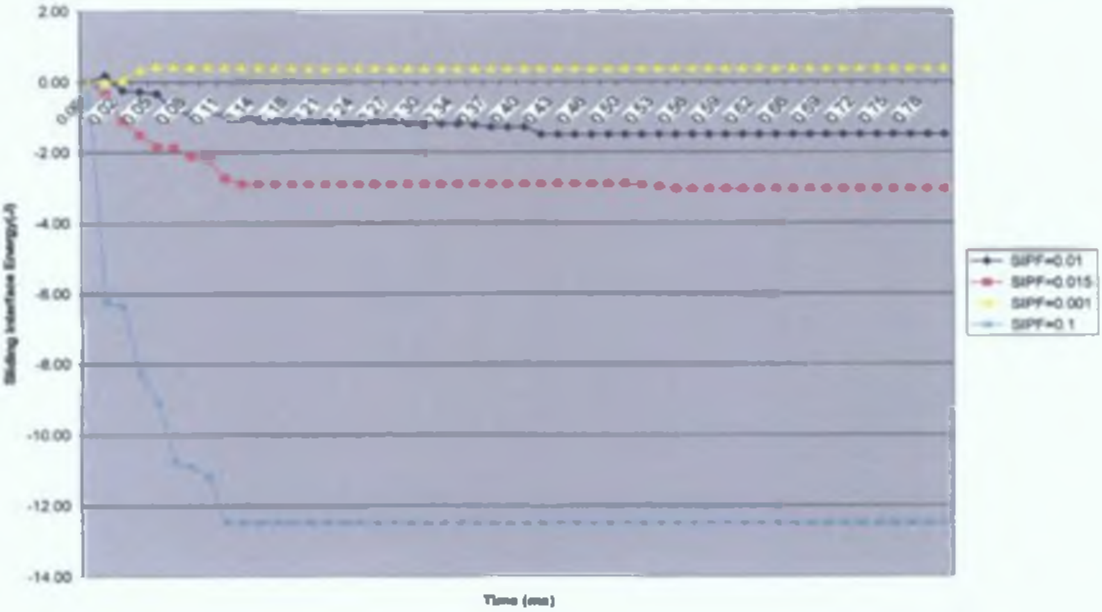

Figure 4.9: Graph of sliding interface energy for different values of SIPF

As can be seen from the graph, a SIPF = 0.01 was almost satisfactory except for the slight peak over zero just after the beginning of the simulation which corresponded with the projectiles first contact with the plate. The value was thus increased slightly to SIPF = 0.015 and this result proved to be ideal. This was similar to the value found by Knight et al. [9] (see figure 2.8).

4.3.4 Strain-rate effects

There are a number of different opinions on whether aluminium materials such as the one being used in this project, Al 2014 T4, are strain rate sensitive. Some researchers have claimed they are not [18] and some have showed otherwise [39]. It was decided to take the values for the Cowper-Symonds model from reference [39] for general aluminium alloys, $C = 6500s^{-1}$ and $P = 4$, and see what effects they had on the model. A simulation was run with the new material model and the results were compared to a simulation with the old material model. It was evident from the results that, as expected, including the strain rate effects resulted in a strengthening of the plate. The ballistic velocity was increased slightly. A comparison can be seen in figure 4.10 below where the residual velocity of the model is plotted for the two simulations.

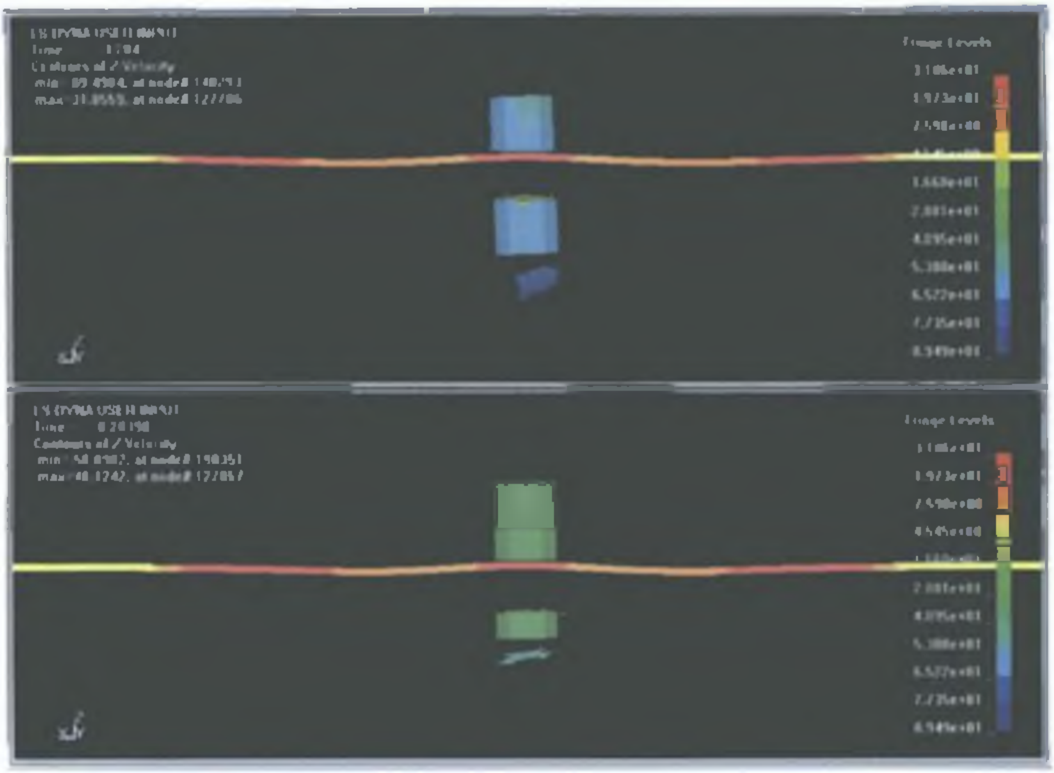

Figure 4.10 Comparison of residual velocity in models with (below) and without (above) strain-rate effects

The plots of the models are taken at the same time and the strengthening effect can easily be seen by the smaller displacement and velocity of the projectile in the strain rate sensitive model.

4.3.5 Cost Cutting Measures

The cost of a finite element simulation is generally measured in the time taken to complete the simulation. This depends on a number of factors including the contact algorithm, the mesh size and shape and the number of elements in the solution. In this case the contact algorithm was as simple as could be allowed and the shape of the elements was as close to ideal as possible with all being regularly shaped brick elements. It was thus attempted to reduce the simulation time by two methods, reducing the number of elements and increasing the mesh size. The aim was to affect these changes without compromising the converged solution. To this end it was necessary to determine where high mesh density was needed and where coarse mesh would affect the solution as little as possible. The centre of the plate where the projectile impacted obviously needed high density mesh as this was the area with the greatest deformation where as the edges of the plate, especially where the plate was clamped, experienced little deformation and so it was felt that a coarser mesh would be sufficient in these areas. It was decided to set a ratio on the lines at the edge of the plate so that there would be smaller elements at the centre of the lines and bigger elements at the ends. A number of different ratios were tried but all seemed to have a detrimental affect on the solution. It was concluded that the buckling that occurred throughout the plate was just as significant a factor in the simulation as the near impact phenomenon and so the mesh density needed to be uniform throughout.

The second method attempted to reduce the simulation time was to remove some of the elements entirely. It was decided that the elements being constrained in all directions where the plate was clamped were adding little to the solution and so the geometry of the plate was altered to remove these sections and the new constraint acted on the area at the edge of the plate, figure 4.11. Unexpectedly, this change caused large changes in the results. A possible cause may be that the change in the mass of the plate, caused by removing the volume at either end, resulted in a difference dynamic response of the plate.

The final method considered to reduce the simulation time was that of using symmetry to essentially halve the geometry of the problem. While the problem was symmetric around two axes it was decided that due to the non-symmetric deformation observed in some of the simulation, possibly caused by some rotation of the projectile, this option may have proved to be inaccurate. In the final solution none of the above cost cutting methods were used as it was felt that the drop in accuracy could not be justified for the gains in solution time.

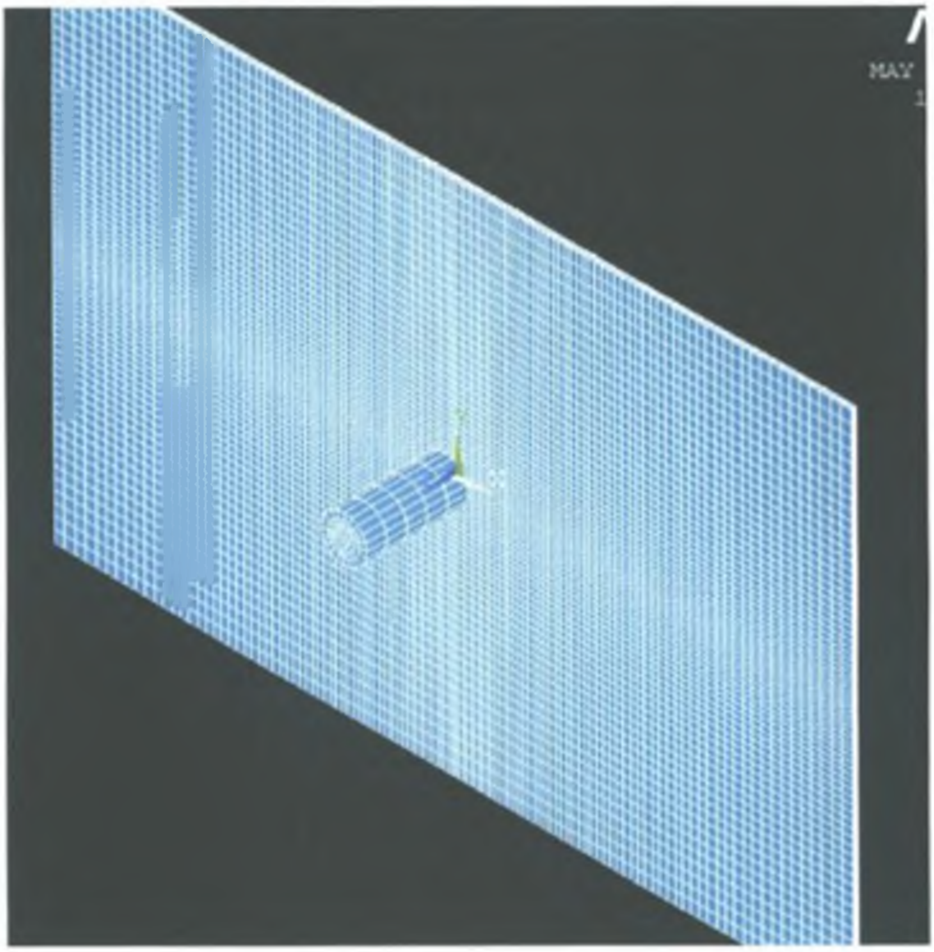

Figure 4.11: Mesh after removal of elements under clamps and with line ratios

4.3.6 The Final Results for the Simple Plate

The final results for the simple plate are shown below. The finite element solutions were compared with the experimental results in three ways. A comparison was made between

- the projectile velocity needed for the various deformations,
- the maximum deformation in the z-direction, excluding the ejected plug or petal, experienced by the plate, and
- the appearances of the deformations in each case.

The finite element model appeared to give a reasonable prediction of the ballistic velocity of the plate with it occurring at 104m/s whereas during experimental testing is occurred anywhere in the 115m/s-120m/s range, except for the anomaly where some penetration was seen at 100m/s, table 4.3.

Table 4.3: Comparison between experimental and finite element velocities

Deformation Type	Experimental Velocity	Finite Element Velocity
No perforation	<115	<104
Slight Perforation	115-120	104
Full Penetration	>120	>104

Figure 4.12 offers proof that this is the ballistic velocity where a graph of the projectile velocity shows the residual velocity to be close to zero as it penetrates the plate after 0.3ms The range of deformation, from slight penetration to petalling to plugging, seen in the experimental analysis was not seen in the final finite element model with plugging occurring, directly after the slight perforation, at 105m/s. The error, however, is within 10% and quite acceptable for this kind of non-linear simulation.

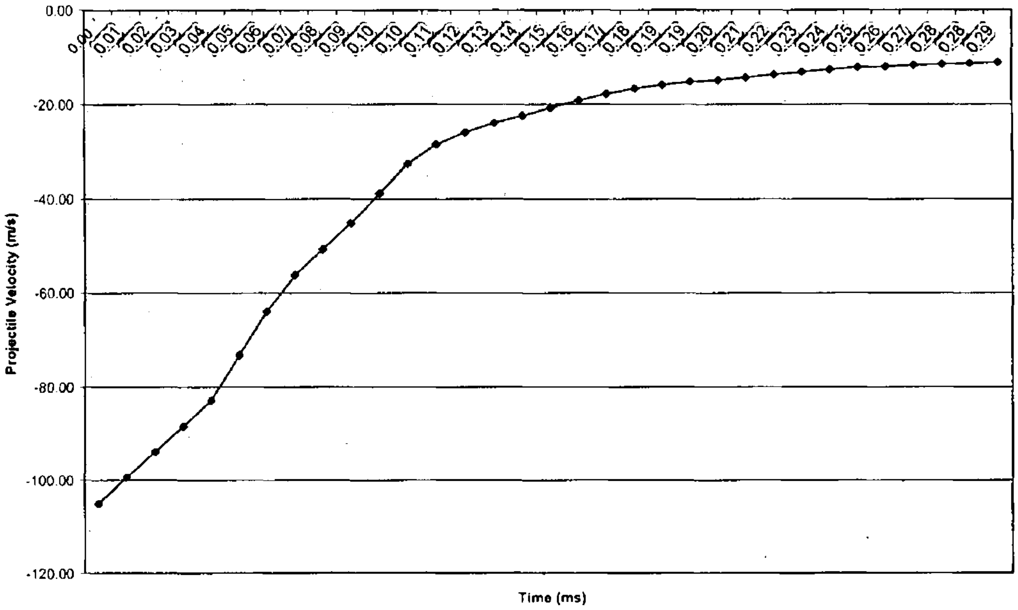

Figure 4.12: Graph of projectile velocity for ballistic simulation

The second characteristic from the finite element model that was compared with the experimental testing was that of the maximum deformation of the plate in the z-direction. In the experiments the results were broken up into three categories, no perforation, slight perforation and complete penetration. In the finite element simulations graphs were produced of maximum displacement of the plate in the z direction. For the no penetration case node 238131 was chosen at the centre of the plate and for the other two cases node 12551 was chosen at the edge of the hole. Figure 4.13 shows their displacement graph over time for several different projectile velocities. The reason for the longer time frames for the 110m/s and 120m/s plots was that they took longer to settle.

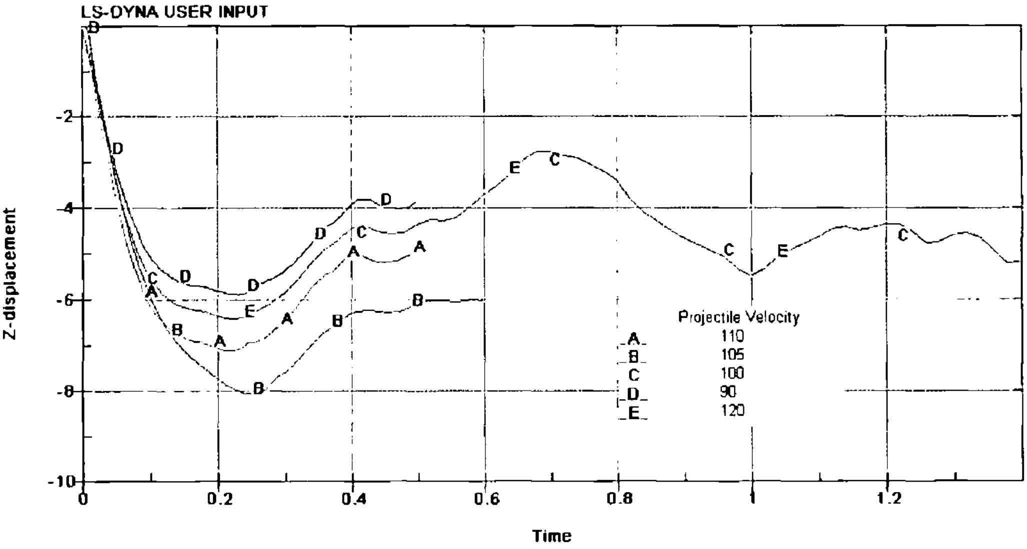

Figure 4.13: Maximum deformation at impact site in finite element simulations

Table 4.4 shows that the finite element results match well with the experimental results for two of the three cases in terms of the height of deformation. Between the no perforation and slight perforation case there is only a maximum error of 5%.

Table 4.4: Comparison between max deformations at impact site

	Average height of deformation at impact site (mm)	
	Experimental	**Finite Element**
No perforation	5.2	5.0
Slight Perforation	5.7	6.0
Full Penetration	6.2	4.5

In the case of the full penetration model, however, there is considerably more error in the region of 30%. The decrease in the height of the deformation after the ballistic velocity was observed in other research [16] but not in this case, see figure 4.14. The reason for this would seem to be the small additional petals seen on some of the full penetration tests. This feature was not present in the finite element solution.

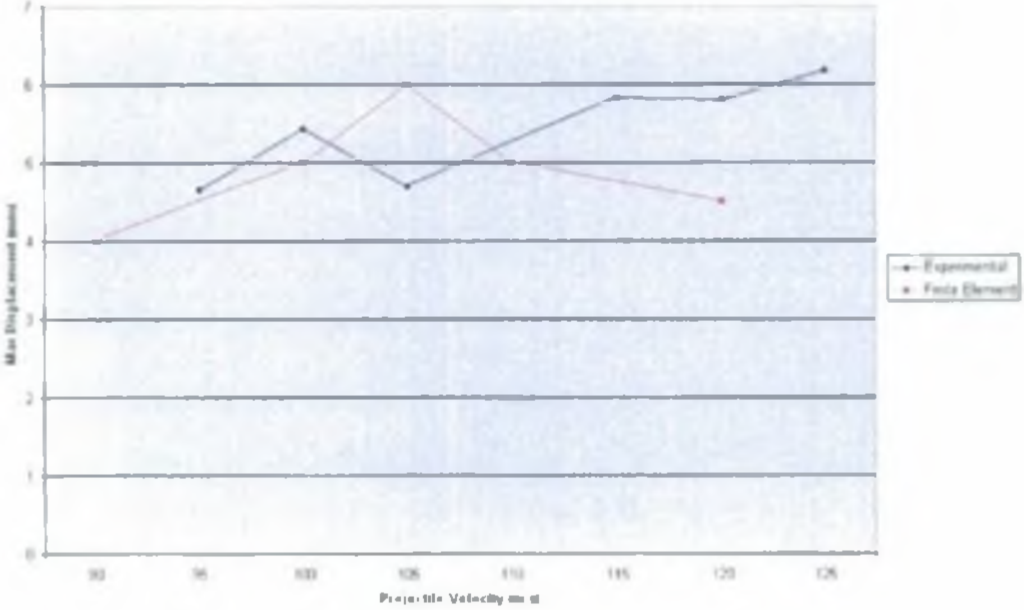

Figure 4.14: Comparison between maximum deformation for experimental and finite element results.

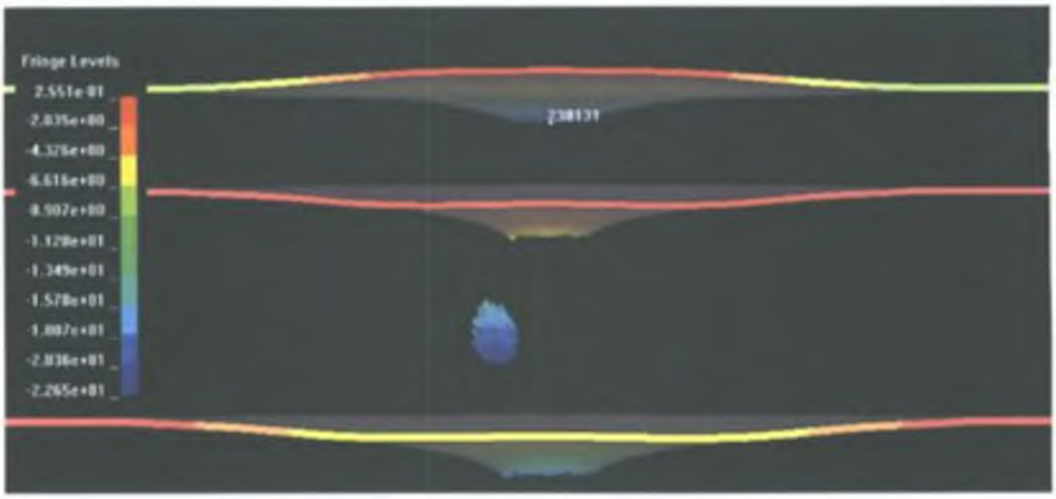

Figure 4.15: Final deformation of test plate for the three cases. (top) No perforation. (middle) At ballistic velocity/Slight Perforation. (bottom) Full penetration

Qualitively, the deformation appeared to match quite well. In the finite element studies the plate was seen to undergo large amount of buckling but then settle back to be almost flat. One can presume this was also the case under testing as the plates have all buckled slightly. The perforations that were observed in the experimental testing were all observed at some stage in the finite element study with the only exception being the tearing of an oblong hole that was observed with some of the through plate penetrations. The lack of this feature in the finite element study may have been due to the limitations of the contact algorithm. Other methods such as tied node with failure contact allow tearing to occur but are much more difficult to set up and do not have some of the capabilities of eroding contact.

4.4 Summary

- The ballistic velocity of the a simple test plate in the experimental testing was found to be in the region of 115m/s-120m/s
- Three distinct deformation shapes were observed
    - Dishing with no penetration
    - Slight penetration with petalling
    - Full penetration with petalling or plugging
- A finite element analysis was undertaken using Ansys/LS-Dyna
- The ballistic velocity of the plate was predicted to be 104m/s reasonably close to the experimental testing
- All three major deformation shapes were seen during the finite element analysis although some minor features were missing

5. Analysis of Impact to Riveted Sheet Metal Structures

5.1 Introduction

This chapter concerns the experimental and computational analysis of impacts to riveted sheet metal structures and in particular a plate with a right angled support, or stringer, attached by four rivets. This represented an increase in complexity from the analysis in the previous section. As before, a set of experimental tests were undertaken in order to validate the finite element results. Two approaches were taken in the computational analysis, modelling the problem fully in 3D and subsequently using 2D approximations for the rivets.

5.2 Experimental Analysis

The experimental analysis was carried out using the gas-fired projectile launcher described in chapter 4. Initial tests were undertaken with right-angles of Al 2014 pop-riveted to plates of Al 2014, however, because of the fact that pop rivets are not representative of fasteners used in aircraft structures it was decided to obtain aircraft standard rivets.

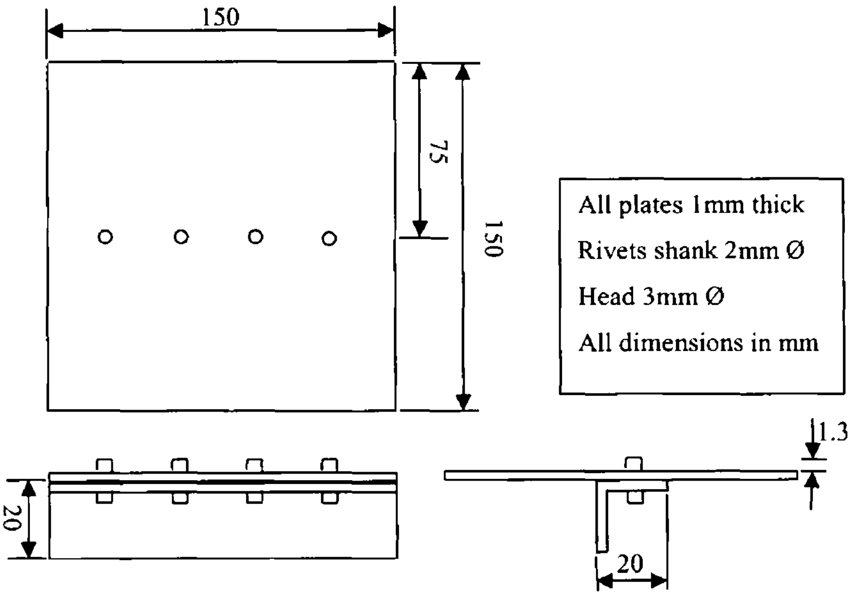

All plates 1mm thick
Rivets shank 2mm 0
Head 3mm 0
All dimensions in mm

Figure 5.1: Riveted plate structure geometry

For this reason aircraft standard rivets, Al 2117 T4, were obtained and used to fasten the angle to the plates as described in figure 5.1. The same titanium projectile used in the previous testing was used. The dimensions for the rivets were obtained from an aircraft repairs manual and are the minimum allowable for the shank diameter used.

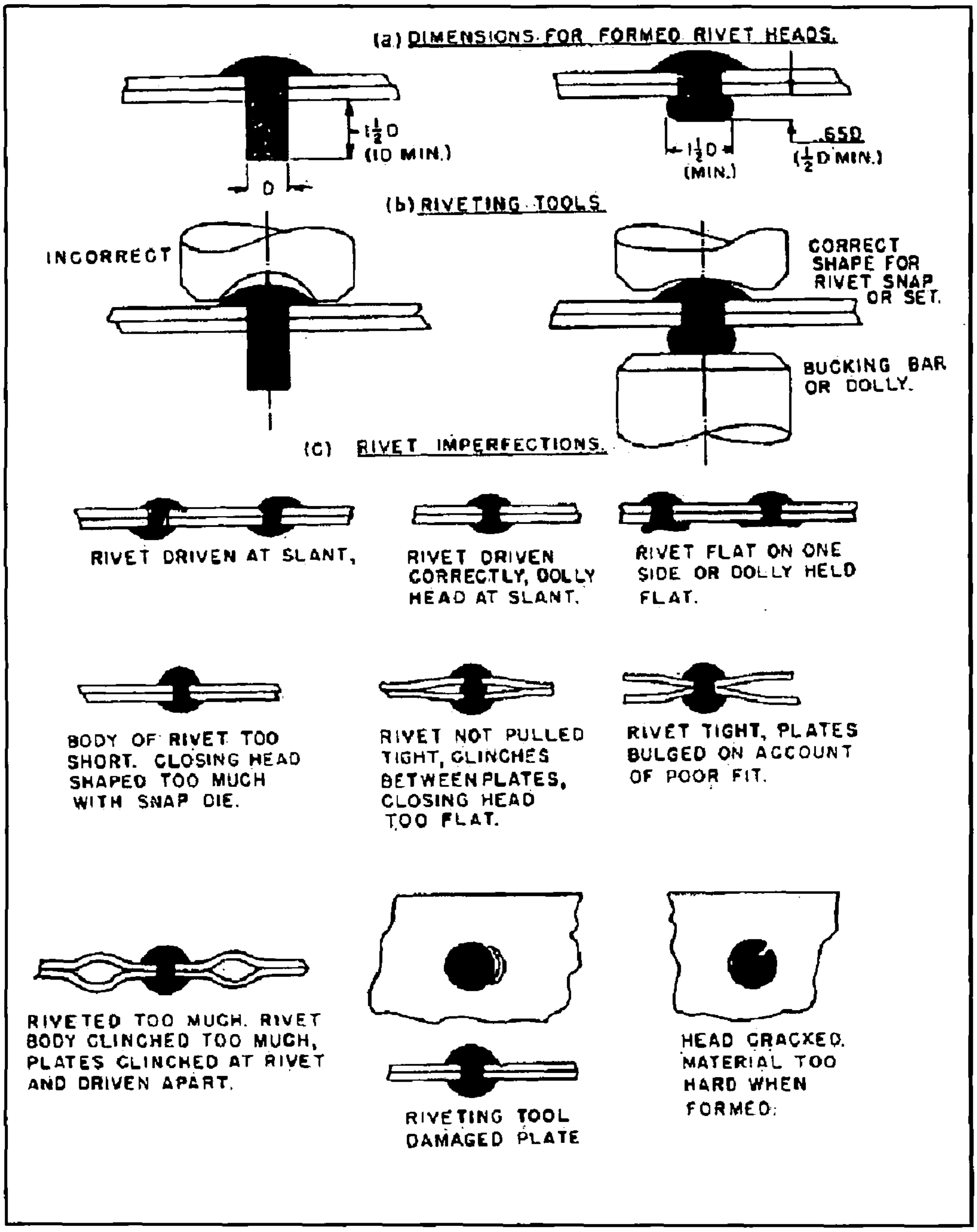

Figure 5.2: Dimensions for formed rivet heads and common imperfections [47]

These parameters and the required shape are shown in figure 5.2. The assembled test plates were impacted at velocities between 125m/s and 220m/s and three main deformation shapes were seen. Table 5.1 outlines these results for both the pop-rivet and solid rivet assemblies and figures 5.3-5.5 shows each of the failure types in the solid rivets assembly. The tearing noted in table 5.1 resulted in some of the rivet fastenings failing through pulling out of the plate but in general the failure mode of the rivets was through shearing of the shank. Figure 5.6 shows an example of this. No perforation of the angle was seen for the solid rivet assembly for projectile velocities within the range of the gas powered projectile launcher used, however, if the trends observed in the pop rivet model are consistent this failure mode should occur somewhere in the 275m/s-325m/s range.

Table 5.1: Deformation modes from experimental analysis

Average Projectile Velocity (m/s)	**Pop-Rivet Assembly Deformation**		
	Plate	**Angle**	**Rivet**
125	Partial plugging of plate	No perforation	Centre rivets pulling out of plate
150	Plugging of plate	No perforation	All rivets failed
200	Plugging of plate	Slight petalling of angle	All rivets failed
250	Plugging of plate	Large petalling failure of angle	All rivets failed
300	Plugging of plate	Plugging of angle	All rivets failed
	Solid Rivet Assembly deformation		
	Plate	**Angle**	**Rivet**
125	No perforation of plate	No perforation of angle	No rivet failure
150	Partial plugging of plate	No perforation of angle	No rivet failure
175	Partial plugging of plate with some tearing	No perforation of angle	No rivet failure
200	Full plugging of plate with tearing	No perforation of angle	2-3 rivets failing
220	Full plugging of plate some with tearing	No perforation of angle	All rivets failed

Figure 5.3: Test plate 4 with no perforation of angle and no rivet failure. Initial velocity =162m/s

Figure 5.4: Test plate 9 with plugging of plate and failure of three rivets but no perforation of angle. Initial velocity 208m/s

Figure 5.5: Test plate 7 with petalling of plate with tearing, failure of all four rivets but no perforation of angle. Initial velocity 218m/s

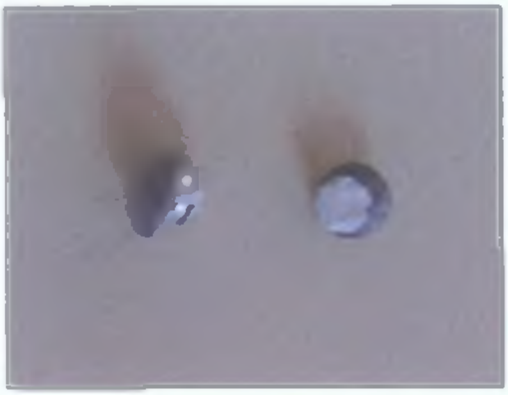

Figure 5.6: Rivets failure by shearing

5.3 3D Modelling of Riveted Plate Structure

It was decided to model the problem in 3D in an attempt to get an accurate solution with no regard for the cost of the simulation. The geometry of the plate and angle were created in the normal way with the holes cut in the plates by subtracting the volume of the holes.

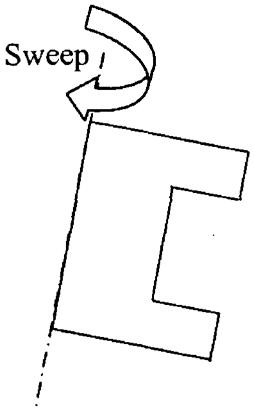

Figure 5.7: Area to be swept to form rivet

The rivet geometry was originally produced by creating three cylinders, corresponding to the two heads and the shank, and then adding the volumes together, however, this geometry then proved difficult to mesh in a satisfactory manner. Instead, a section was taken though half the rivet and the area then swept around the central axis as shown in figure 5.7. Some difficulty was also experienced in meshing the plate and angle due to the presence of holes. Firstly the volumes were split up to enable a cube around the holes to be meshed separately but this proved to be problematic. It was only possible to mesh this cube around the hole with tetrahedral elements, which are less accurate than hexahedral elements, and the interface between the tetrahedral and hexahedral elements was not very satisfactory. It was also found to be difficult to create a symmetric mesh while meshing the volumes separately. It was found subsequently to be possible to mesh the volume all together using the sweep command. The plate was meshed by creating a 2D mesh on the front face of the plate and then sweeping the mesh of the face all the way through to the back surface. The same was done with the part of the angle parallel to the plate with the volume perpendicular to the plate meshed separately. The size of the mesh was based on the mesh from the converged solution of the simple plate with 155 elements along each side of the plate, shown in figure 5.8. This resulted in a total of 160941 elements for the plate, 22395 elements for the angle, 355 elements for the projectile and a total of 6960 elements between the four rivets, which were treated as one part. As before an investigation of convergence was made and this model was judged to be a converged solution.

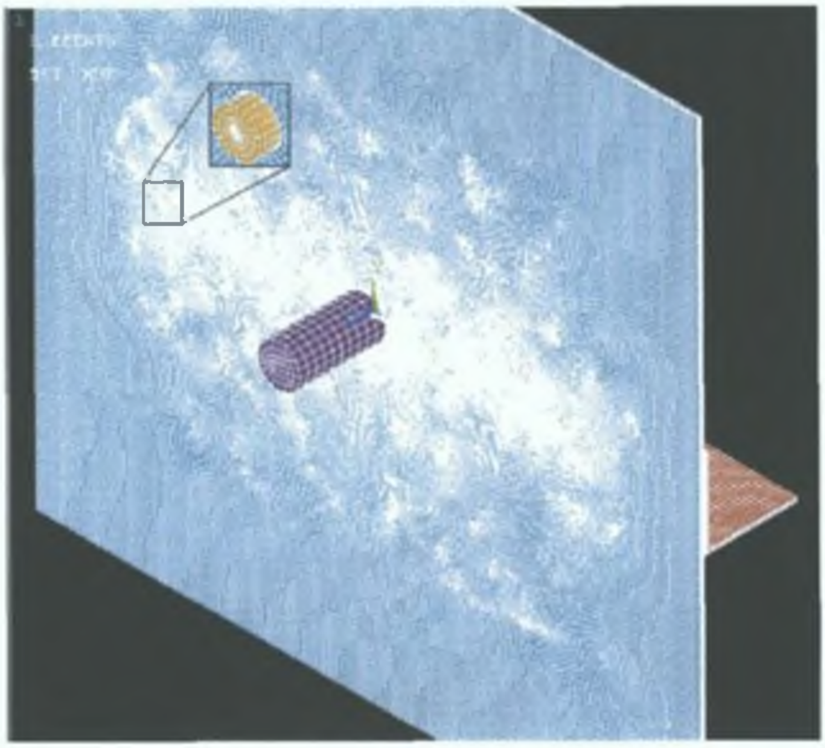

Figure 5.8: Details of the mesh used in 3D model

Contact was again defined between all the parts. Eroding surface to surface contact was used in most cases, i.e. between the projectile, the plate and the angle and between the rivets, the plate and the angle. However automatic surface to surface contact was used between the plate and the angle as no erosion of elements was expected here and the automatic contact option tends to be more robust. The ideal value for the SIPF was again investigated and in this case the default of 0.1 provided good accuracy without causing any damage free penetration.

The material model for the titanium projectile was the same as it was in the simple plate analysis but the material used for the rivets was different. The rivets were made from Al 2117 T4. The same non-linear kinematic hardening model was used as before and parameters were found from the manufacturers certificates with some reference again to Knights et al [9].

5.3.1 Initial Results

As in the case of the simple plate it was decided again to concentrate on the ballistic characteristics of the riveted plate structure. In this case the ballistic velocity was a bit more complicated as the projectile was impinging on two surfaces, that of the plate and the angle. As seen in the experimental results this resulted in several different deformation modes. These included:

- no perforation of plate or angle,
- perforation of plate, either partially or full, but no perforation of angle
- and perforation of plate and angle, either partially of fully.

Another factor that needed to be considered was that of the rivets, their deformation, if they failed and their mode of failure.

The first tests were carried out at the ballistic velocity of the simple plate, which was in the region of 105m/s. As was expected the riveted plate structure proved to be more resilient than the simple plate and no perforation of the plate or angle was seen at this velocity. It was then decided to increase the velocity to 125m/s.

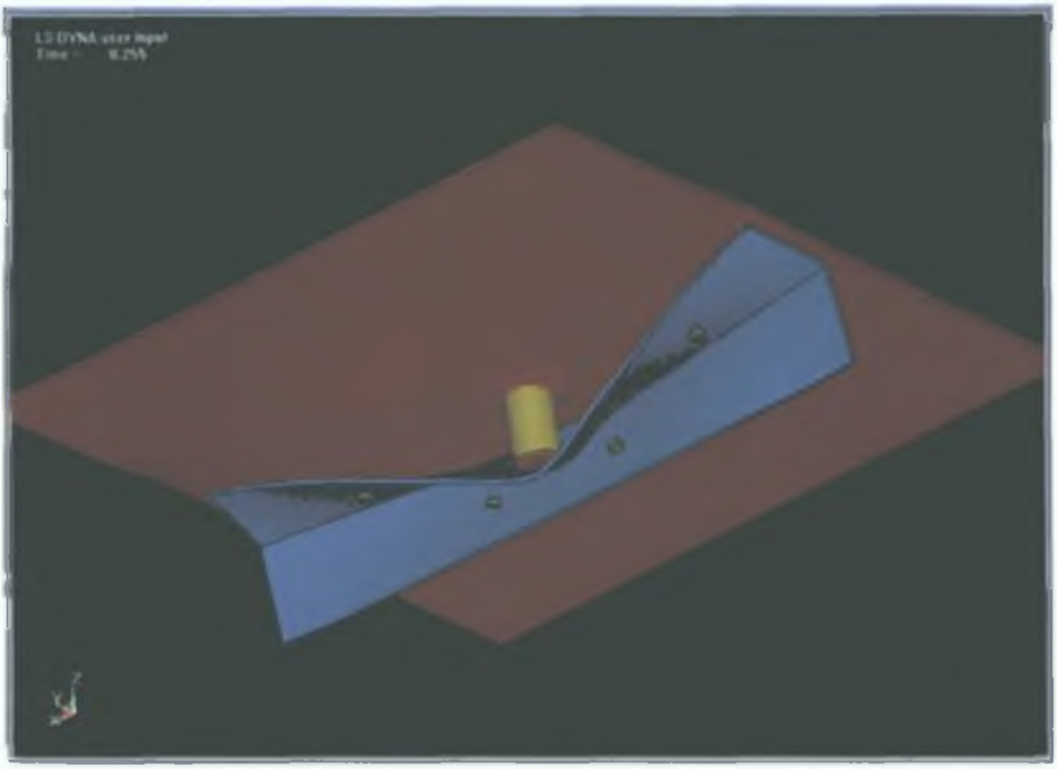

Figure 5.9: 3D Model after plugging of plate and failure of rivets. Initial projectile velocity 125m/s

At this velocity the second deformation mode was seen with the projectile penetrating the plate fully but failing to perforate the angle, as seen in figure 5.9. The four rivets in this case failed by shearing within 0.075ms of the beginning of the simulation, the failure being cause by the dynamic buckling of the plate. This was the mode of failure of the majority of the rivets seen in the experimental testing but it occurred at a much lower projectile velocity. As the projectile velocity was increased further, it was found that the initial projectile velocity needed to be in the region of 150m/s to penetrate both the plate and the angle before the rivets failed, as seen in figure 5.10. All of the rivets failed before the projectile came to rest. This deformation mode was not experienced at all with the solid rivets assembly. When compared with the experimental results it is clear that the finite element model was not succeeding in modelling the rivets correctly. The projectile velocity needed to induce rivet failure in the FE model was found to be too low as was the velocity needed to penetrate both plate and angle. Since the modelling of impact to the simple plate had only small errors in comparison it was assumed that the modelling of the rivets was at fault.

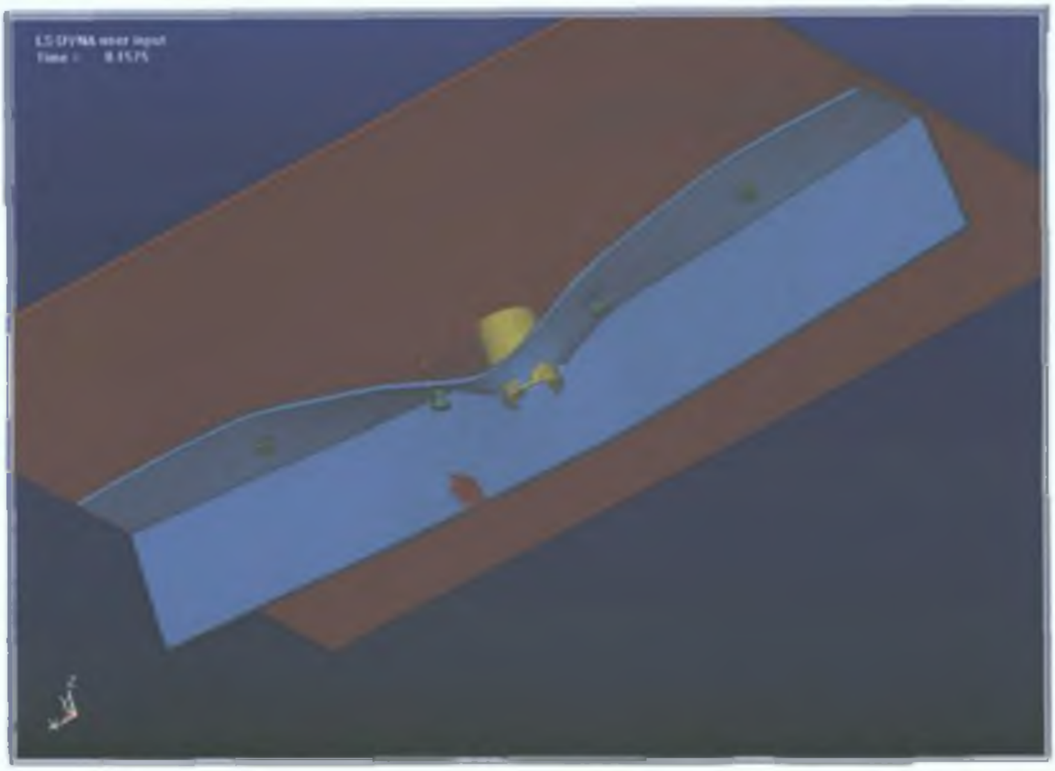

Figure 5.10: 3D Model with full penetration of plate and angle. Initial projectile velocity = 150m/s

5.3.2 Modelling of Pretension in Rivets

Due to the large differences between the finite element and experimental results for the riveted plate structure it was decided to investigate possible methods for reducing the error. One of the possibilities that had not been taken into account in the original model was that the original riveting process would affect the characteristics of the assembly before it was impacted. Therefore it was decided to introduce a pretension into the rivets to simulate the stresses induced during the riveting process. To do this it was necessary to employ the implicit Ansys package to do a combined implicit-explicit analysis. The pretension would be introduced to the model in a static analysis and the resulting displacements would be exported to the explicit Ls-Dyna solver. The explicit analysis would then be solved using these new displacements as initial conditions.

From the beginning this analysis proved problematic. The implicit solution needed to be solved in Ansys. Unfortunately the version of Ansys available had a restriction of a maximum of 20,000 elements so it was impossible to use the same mesh with proven convergence that had been used in the last section.

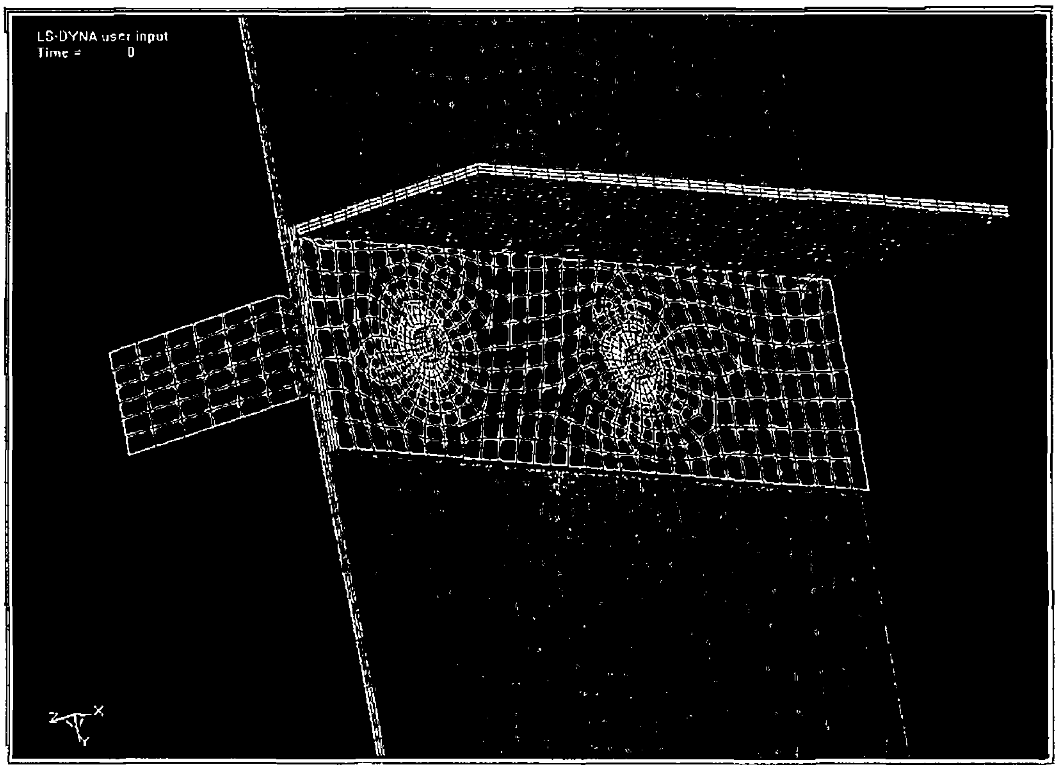

Figure 5.11: ½ symmetric mesh for used for pretension analysis

In fact it was required that the number of elements be reduced by (190,651-20,000) = 170,651 elements. As a result of this the accuracy of this model was always going to be questionable. In an attempt to minimize this it was decided to use the symmetry of the problem and model only half of the riveted plate assembly as seen in figure 5.11. As mentioned before in section 4 this was not considered to be as accurate a method as using the full plate due to the non-symmetric deformation noted but it was decided that it would have a less detrimental affect than using a courser mesh.

The pretension was applied in Ansys by creating a section through the rivets and then meshing them with pretension elements. A load was then applied to these elements and the model was solved. The aim was to induce maximum residual strains of 2×10^{-4} in the assembly to simulate the strains induced by riveting as seen in figure 2.9 [10]. The effects of this are shown below in figure 5.12 and figure 5.13. The resulting displacements from this implicit static analysis were then saved and the model reopened and renamed to preserve this data. The elements were then changed to explicit elements and the initial conditions and material models were updated.

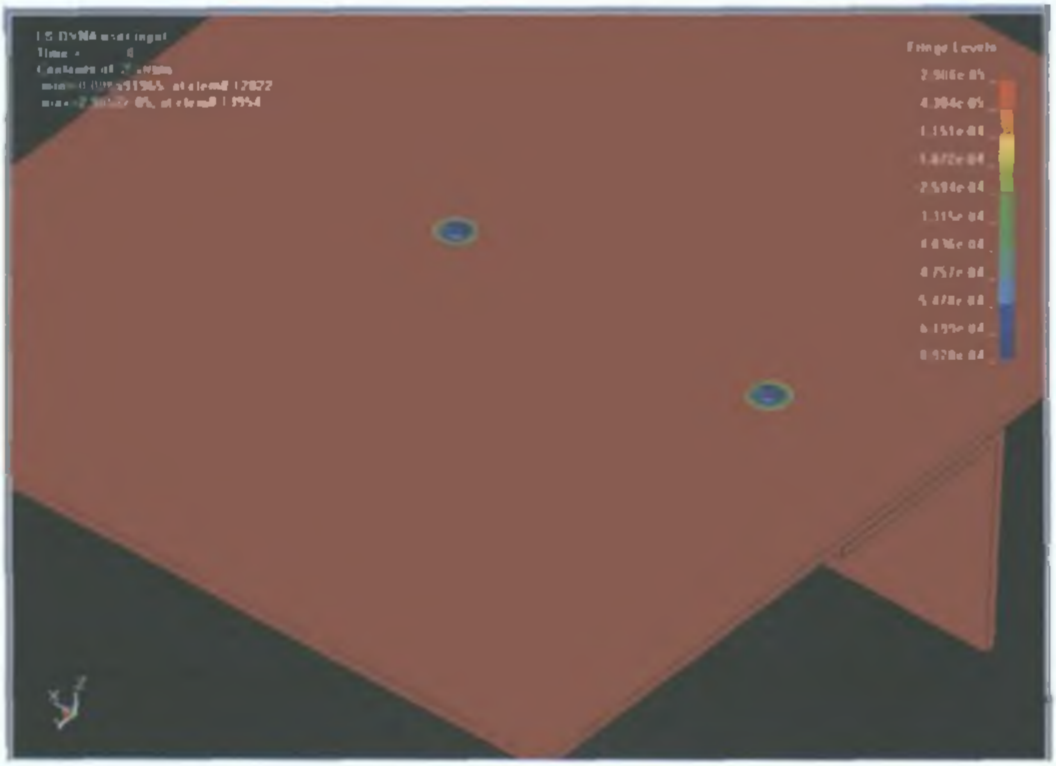

Figure 5.12: Plot of initial strain induced in the plate and angle due to the riveting process

Figure 5.13: Plot of von-mises stress in cross-section through rivets, plate and angle induced by the riveting process.

It was necessary to delete the sections and the pretension elements from the model as they had no mirror in the explicit solution and were in any case redundant at this stage.

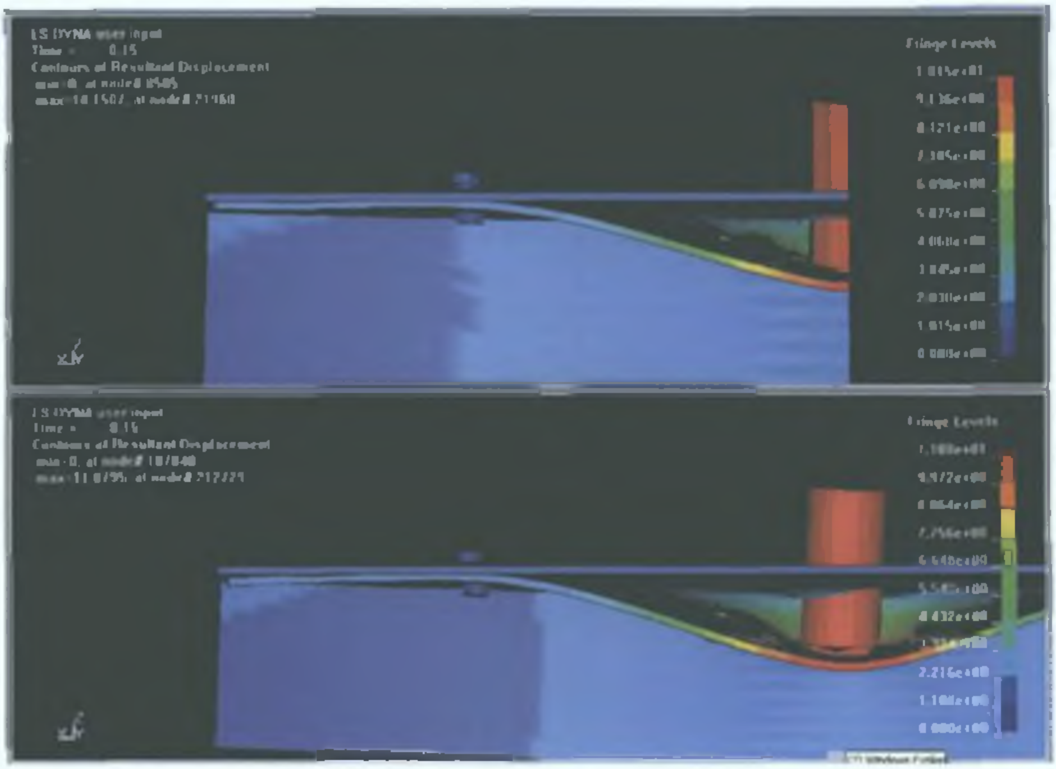

Figure 5.14: Comparison of displacement between pretension model (top) and standard model (bottom)

Finally the displacements from the implicit analysis were read into the explicit analysis. The model was then solved as normal with the first step used to initialise the displacements through the dynamic relax function.

The results obtained were compared with a similar model without the initial displacements as it was felt that the difference in the mesh with the full model would make the comparison invalid. Figure 5.14 below shows a comparison between the maximum displacement in the two of the models and it clearly shows that the pretension has resulted in very little change in the results. The maximum deflection at the centre of the angle is 10.15mm for the pretension case and 11mm for the model without pretension after 0.15ms. The mode of failure of the plate, plugging, and the rivets, all four fail by shearing is similar. As a result of these negligible differences it was decided that applying pretension to the 3D rivets did not sufficiently approximate the riveting process and was in no way beneficial towards modelling the problem in a satisfactory manner.

5.4 2D Modelling of Rivets with Failure

The idea behind initially modelling the rivets in 3D was to find out if it was possible to model this problem accurately but it was not found to be at all practical. For a simulation lasting 0.75ms the solution time was 73 hours 49 minutes. This is for a model with four rivets. The time would increase significantly with each new rivet and quickly become not just impractical but impossible to solve. As a result a more practical and efficient way was sought. 2D approximations are the recognised way of modelling fasteners such as rivets and so an investigation was conducted into their application and accuracy.

5.4.1 TNWF Rivets

The first method used to approximate the rivets used the tied node with failure (TNWF) contact option. This option ties coincident nodes together until failure criteria are reached. In this case the failure criteria were the shear and tensile forces experienced by the nodes and were given by the shear and tensile yield

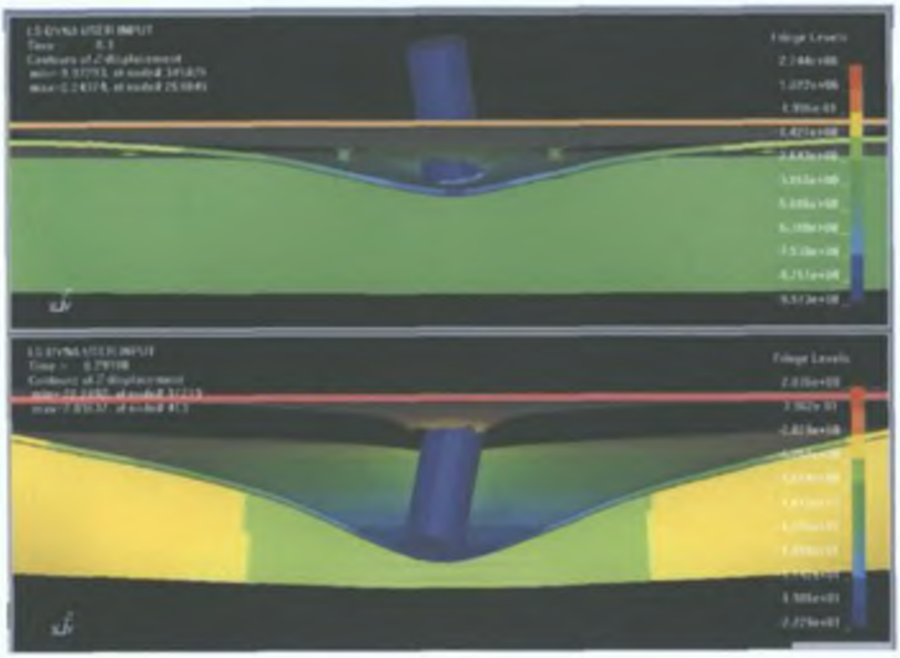

Figure 5.15: Comparison between 3D model (top) and TNWF model (bottom) after 0.3ms.

strengths of the rivet material. To simulate the rivets several nodes, in a diameter equal to the head of the rivet, on the adjoining surfaces of the plate and angle were constrained using TNWF. The results were compared with the 3D model and the experimental results. The comparison below between the 3D model and the TNWF 2D approximation, figure 5.15, show that the TNWF rivets tended to fail much earlier than the full 3D rivets and with less deformation of the plate around the rivets.

5.4.2 Spot-weld Rivets

The other method used to approximately represent the rivets was that of a spot-weld. This facility allows non-coincident nodes to be tied together. Failure was again linked to the tensile and shear forces on the rivets. Nodes on the adjoining surfaces of the plate and angle were again constrained with much the same results as the TNWF rivets. Attempts were made to improve its performance by coupling the nodes in the plate and angle where the rivet would be, but due to the fact that the surface nodes that were spot-welded could not be included, the coupling had little or no effect. Some improvement was seen when nodes from the opposite side of the plate and angle were constrained. This was valid if one worked on the assumptions that the rivets essentially created a solid component between the two rivet heads until the rivet failed and it was possible, because unlike TNWF, the nodes did not need to be coincident. This method produced results similar to those of the 3D model in terms of deformation and timing of rivet failure as seen below in figure 5.16. The advantage of the 2D model at this point is that the solution time is roughly one tenth of that needed for the full 3D model. The 2D model also had some through thickness damage done to the plate at the rivet sites which may be read as the rivets pulling out of the plate. However as the model was similar to the 3D model large inaccuracies still existed.

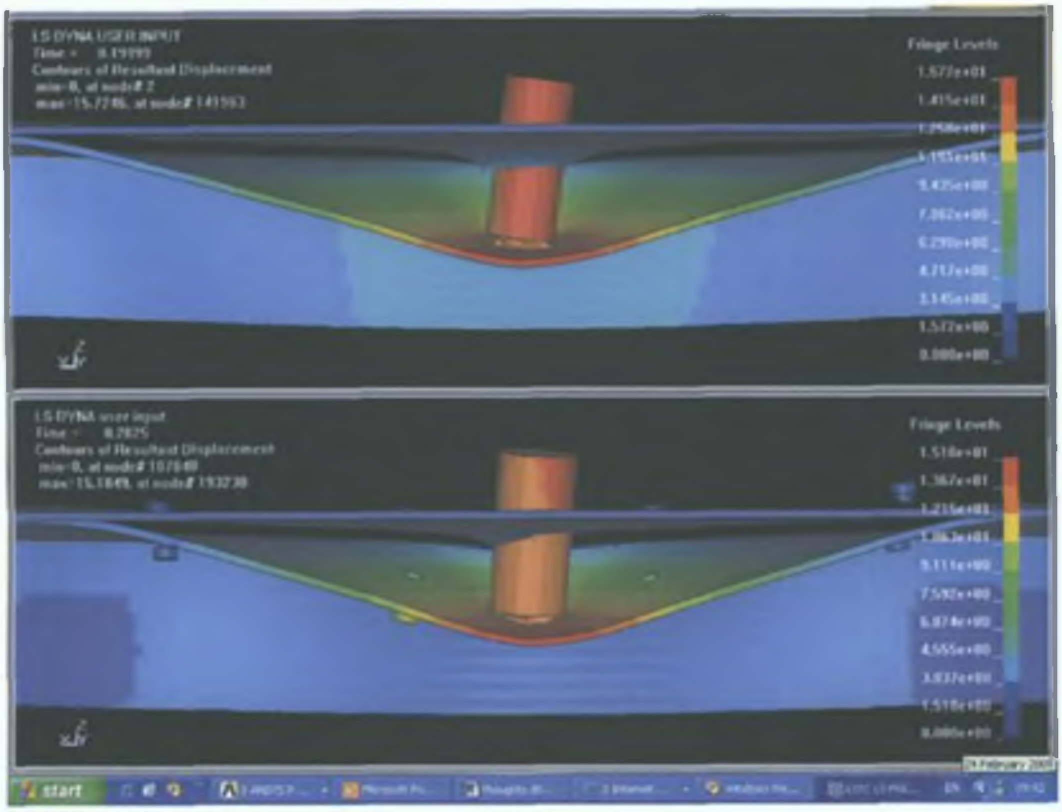

Figure 5.16: Comparison plot between the deformation of spot-weld rivets (top) and 3D rivets (bottom)

5.5 2D Modelling of Rivets without Failure

To begin with this option was not considered feasible as modelling rivets that cannot fail would appear at first to be inherently wrong since it is obvious that rivets do fail. However when the modes of failure of a riveted joint are examined it becomes clear that such a model could work well. One of the causes of failure in riveted joints is not the failure of the rivets themselves it's the failure of the plate around the head of the rivets i.e. the rivets pull out of the plate [10]. As a result is was decided to model rivets with no failure criteria to see if it was possible to reproduce this in a finite element simulation.

Having learned from the TNWF and spot-weld rivets it was decided not to use the tied node contact option. A facility within the weld command was found by which two non-coincident nodes could be constrained without any failure criterion. It was unsurprisingly called the rivet command. Again a selection of nodes of diameter 3mm on opposite sides of the plate and angle were constrained. The results of this FE model were closer to the experimental results with the rivets proving to be much more robust. The plot of the assembly's deformation after an impact with a projectile velocity of 150m/s, figure 5.17, shows the second deformation mode, that of perforation of the plate with failure of the all four rivets. The holes around the centre rivets simulate the rivet pulling out of the plate as was expected. Unfortunately the plate elements around the outer holes remain for the most part intact. The elements on the surface of the

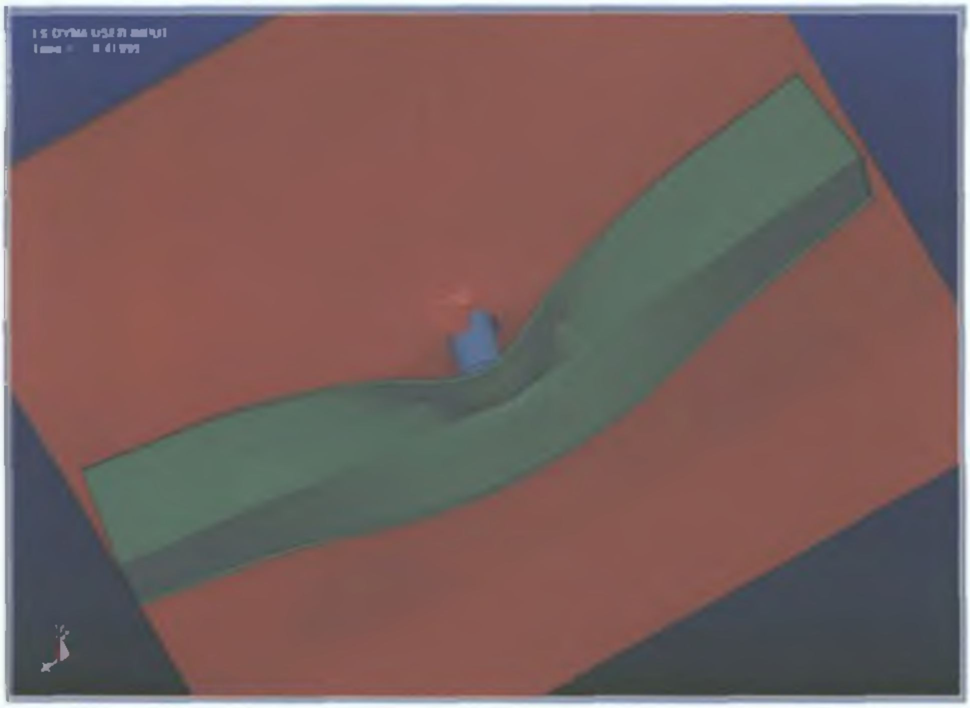

Figure 5.17: Failure of plate and four rivets. Initial projectile velocity = 150m/s

plate, with which the constrained nodes are attached, erode away before the others and release the constraint. This results in a slight dent in the surface of the plate and no through thickness damage. All three deformation shapes were again seen for this model and although the projectile velocities were close to those observed for the pop-rivet assemblies, they still underestimated the more realistic solid rivet assembly's behaviour by a margin of 25%-35%.

5.6 Final Results

A comparison between all of the results both experimental and numerical is presented in table 5.2 on the following page.

			Deformation Type		
Projectile Velocity (m/s)	**No perforation of plate or angle and no rivet failure**	**Some perforation of plate but no rivet failure**	**Some perforation of plate, some rivet failure, no perforation of angle**	**Perforation of plate, no perforation of angle and total rivet failure**	**Perforation of plate and angle and total rivet failure**
125-150	Solid rivet assemb.	Pop rivet assemb. 2D rivet model		3D rivet model	
150-175		Solid rivet assemb	Pop rivet assemb. 2D rivet model		3D rivet model
175-200			Solid rivet assemb	Pop rivet assemb. 2D rivet model	3D rivet model
200-250				Solid rivet assemb Pop rivet assemb	2D rivet model
250-300				Solid rivet assemb	Pop rivet assemb 2D rivet model 3D rivet model

Table 5.2: Comparison of experimental and finite element results

5.7 Summary of Chapter 5

An experimental analysis was undertaken using the gas powered projectile launcher. Al 2014 test plates were fabricated with Al 2014 angles riveted to plates using pop rivets and standard (Al 2117) aircraft rivets. Three main deformation shapes were seen:

- No perforation of plate or angle with no rivet failure
- Partial or full penetration of plate with no perforation of angle and some rivet damage
- And full penetration of plate and angle with failure of all rivets.

This last mode was only seen for the pop rivet assembly.

The experimental analysis was followed by a finite element analysis. Several modelling techniques were attempted including:

- Modelling the rivets in 3D with and without pretension
- Modelling the rivets as simple approximations with failure using the TNWF contact option and the spot-weld facility
- And modelling the rivets as simple approximations without failure using the rivet command.

When compared with the experimental results all of the models proved to have large inaccuracies. The 3D rivet model was comparable with the spot-weld model but had errors of almost 50% when compared with the solid rivet assembly. The rivet model without failure was closer to the experimental results, matching closely to the pop rivet assembly, but still gave an error of 30% when compared with the solid rivet assembly.

6. Design and Manufacture of Gas-powered Projectile Launcher

6.1 Introduction

The testing that was undertaken for this project was carried out with the gas-powered projectile launcher shown in figure 4.1 in chapter 4. Clearly this rig was limited in terms of the projectile size and shape that could be fired and test plate size that could be used. As a result it was decided to design a new test rig that would be available in the university for further experimental testing in the area of impact mechanics. The aims of the design process are outlined below

- To be able to take test plates of up to $0.5m^2$
- To be able to fire projectiles of any shape up to a maximum diameter of 50mm
- To be able to impact the plate at any point and so facilitate multiple impacts to plates
- To be able to impact the plate at an angle

The design was based on the older rig but was to be fabricated from scratch with these four new concepts integrated.

6.2 Projectile Firing Concepts and Design

The main aspects of the new test rig were to be taken from the proven concepts of the older rig. As a result the design and modification history of the old rig was examined closely [48]. An investigation of alternative design types of gas-powered projectile launchers available in literature was also undertaken [7-9, 12-19].

The first challenge was to find a method of firing different sizes and shaped projectiles. Some early concepts included either replacing the barrel or having inserts for each projectile but both were rejected as too costly and time consuming. A solution was found however after examining other designs in literature. In several cases [8, 9, 49] a device called a sabot had been used to overcome the problem. The sabot was essentially a seat for the projectile, the outside diameter of which conformed to the inside diameter of the barrel. The sabot would impact a stop towards the end of the barrel and the projectile would continue onto the target. To facilitate different sizes and shaped projectiles different sabots could be manufactured.

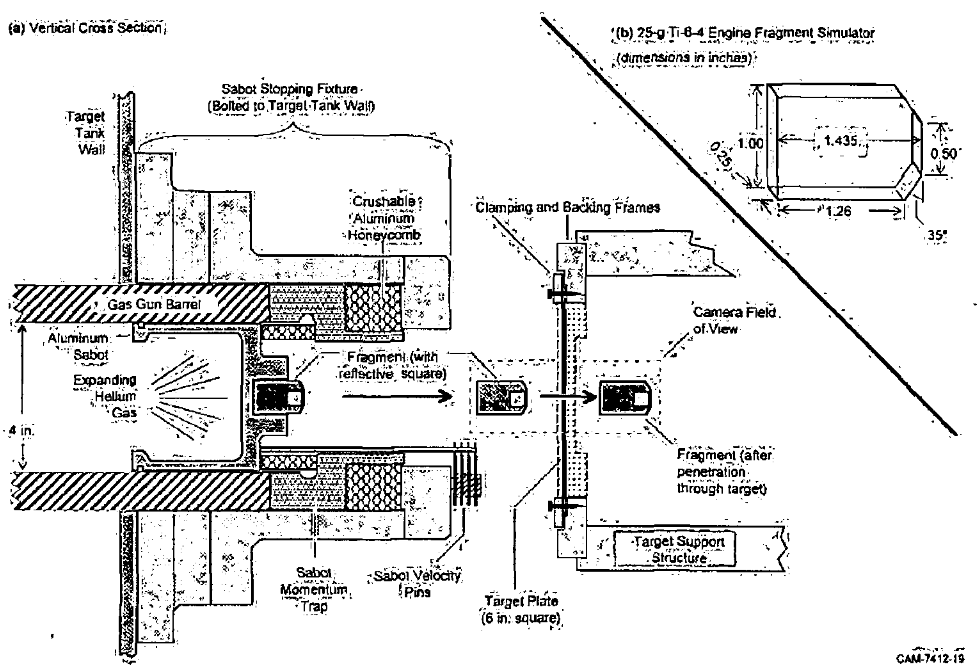

Figure 6.1: Sabot design used by Knight et al. [50]

The two most important features of this design are the sabot and the sabot stop. In figure 6.1 above it can be seen that the sabot is designed to maximise the pushing power of the gas and that the sabot stop is made from crushable aluminium foam that absorbs some of the impact. This is necessary so that the sabot is not damaged on each firing. Another design for sabot and sabot stop that has proven successful is shown below in figure 6.2. The sabot itself is made from an impact absorbing rubber so that it is not damaged on impact. This design was chosen for the new test rig because of its simplicity. Some other useful features of this design included the Teflon bushings, which reduced the friction effects between the barrel and the sabot, and the open end that vented the gas from the barrel.

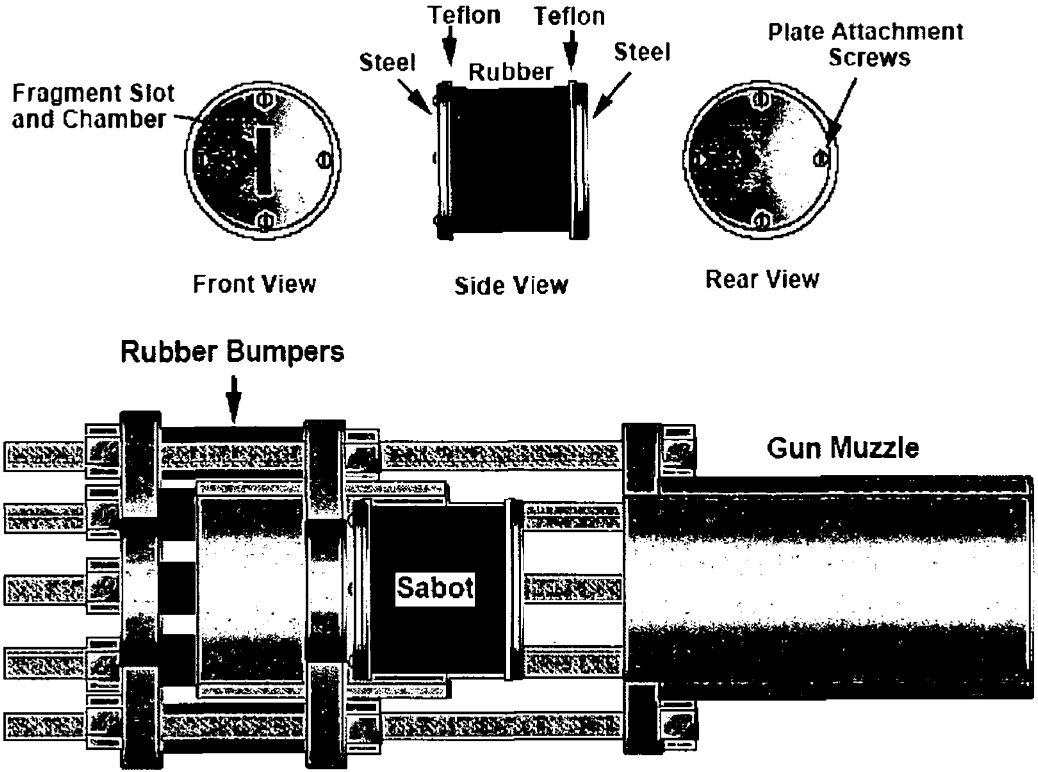

Figure 6.2: Sabot design by Manchor and Frankenberger [51]

With the design decided on for firing the projectile by using a sabot it was now necessary to check that the solution would be practical to implement. The calculations below show that it is.

6.2.1 Proof of Concept Calculations

These calculations were developed from those used in the design of the old rig [48]. Since the diameter of the barrel was to be scaled up it was thus necessary to scale up some of the other components. The length of the barrel was increased from 1m to 1.5m to give a greater length to accelerate the projectile and the gas reservoir was scaled up to have a volume greater than that of the barrel. As a result the volume of the reservoir, V_r, became

$$V_r = \pi r_r^2 l_r \qquad (6.1)$$

where r_r = radius of the reservoir = 75mm and l_r = length of the reservoir = 500mm. Therefore

$$V_r = \pi \times .075^2 \times .5 = 8.84 \times 10^{-3} m^3 \qquad (6.2)$$

The volume of the barrel, V_b, is then

$$V_b = \pi \times .03^2 \times 1.5 = 4.24 \times 10^{-3} m^3 \qquad (6.3)$$

where r_b = radius of barrel = 60mm and l_b = length of barrel = 1.5m and the volume of the sabot, V_s

$$V_s = \pi \times .03^2 \times .04 = 1.13 \times 10^{-4} m^3 \qquad (6.4)$$

The sabot was to be mostly manufactured from an impact resistant polymer called Ertalon 6PLA. Its density, ρ, was 1.15g/cm^3. The sabot's mass was therefore given by

$$m = 1150 \times 1.13 \times 10^{-4} = 0.13 \text{ Kg} \qquad (6.5)$$

If the maximum velocity that the projectile needs to reach is assumed to be v=300m/s then the energy needed to accelerate the projectile to this speed is

$$E = 1/2mv^2 = 5.85kJ \qquad (6.6)$$

The pressure required in the reservoir is therefore given by the equation below

$$P_1 = \frac{\frac{1}{2}mv^2}{V_r \ln\left(1 + {V_b}/{V_r}\right)} \qquad (6.7)$$

So P_1 = 0.586 MPa or 5.86 bar. This is only an approximate value as it does not take into account friction effects but it is easily within the capabilities of the high pressure gas cylinder available.

6.3 Reservoir Design

As mentioned above it was necessary to scale up the gas reservoir as the barrel was scaled up. The idea of this was that the reservoir should have a greater volume of gas stored than was necessary to fill the volume of the barrel. This would insure that the projectile was accelerated down the full length of the barrel. As a result of this the internal volume that was needed for the reservoir was known. However it was still important to design the reservoir in a safe and practical way. Initially welding of the end plates was considered but the lack of the facilities to check the welds and the high pressures involved ruled out this option. So it was decided to bolt the end plates to the reservoir. To show that the pressure vessel was suitable for the application intended it was designed according to the following calculations.

6.3.1 Wall Thickness Calculation

Clavarino's equation (for ductile materials) gives a wall thickness t for thick walled closed ended pressure vessels.

$$t = \frac{d_i}{2}\left(\sqrt{\frac{S_t + (1-2\mu)p_i}{S_t - (1+\mu)p_i}} - 1\right) \text{..............................} \quad (6.8)$$

where d_i = internal diameter = 150mm = 0.15m, S_t = permissible working stress in tension, μ = Poisson's ratio = 0.3, p_i = internal pressure = 25 bar = 2500000. For En-16 Steel, $S_t = \sigma_{ut}$/safety factor where σ_{ut} = allowable UTS = 620MPa and taking a safety factor of 3 gives S_t = 207Mpa.

Therefore from equation 1 the wall thickness, t, was determined as $7.7\text{x}10^{-4}$m $\approx$ 0.8mm. The walls of the pressure vessel exceed this by a large margin, the walls being 10mm thick, due to the necessity of bolting on the end plates.

6.3.2 Endplate Bolt Calculations

From [52] the minimum seal load on a bolt for a pressure vessel is given by:

$$W_{m2} = \pi bGy \ldots\ldots\ldots\ldots\ldots\ldots\ldots\ldots\ldots\ldots\ldots (6.9)$$

where b = gasket width = 0.002m, G = Gasket sealing diameter = 0.155m, y = seating stress = 1.4 for a rubber O-ring. This gives us W_{m2} = 1363N.

Therefore the initial tightening stress σ_I on each bolt is:

$$\sigma_I = \text{Initial Load/Root Area} \ldots\ldots\ldots\ldots\ldots\ldots\ldots\ldots (6.10)$$

where the root area $A_r = \frac{\pi}{4} d_r^2 = 1.96 \times 10^{-5}$ m^2

This gives us a value of σ_I = 69.4 MPa. The bolt material is high tensile steel with a tensile yield stress σ_y = 586MPa. Hence the available stress $\sigma_a = \sigma_y - \sigma_I$ = 516.6MPa

Taking a factor of safety of 2 the available load per capacity per bolt over the stressing area,

$$F_a = Ar \times \sigma_a/2 = 5062.7 \text{ N} \ldots\ldots\ldots\ldots\ldots\ldots\ldots\ldots (6.11)$$

The minimum required bolt load for operating conditions is given by:

$$W_{m1} = \pi G^2P/4 + 2\pi GbkP \ldots\ldots\ldots\ldots\ldots\ldots\ldots\ldots (6.12)$$

Where P = Operating Pressure = 25 bar, k = gasket factor = 0.25

This gives a value of 47172 N. Therefore the number of bolts required is

$$W_{m1}/F_a = 9.3 \Rightarrow 10 \text{ bolts} \ldots\ldots\ldots\ldots\ldots\ldots\ldots (6.13)$$

When fabricated each end plate was bolted with 18 bolts for additional safety.

6.4 Final Barrel Assembly

The final barrel assembly was designed and modelled in Pro Engineer. In the previous test rig the barrel was vertical but because of the extra half metre in the barrel length and the larger reservoir this was not practical in the new rig and the barrel was mounted horizontally. The initial sabot, see figure 6.3, was designed to hold the titanium projectile used by the other test rig.

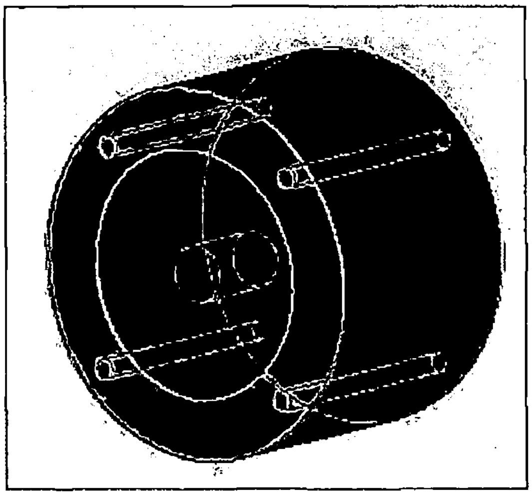

Figure 6.3: First sabot design

The barrel was fabricated from a tube with an internal bore of 60mm and a 10mm wall thickness. One end of the tube has threaded internally to connect to the valve. At the other end a stop was bolted to the end of the barrel for the sabot to impact. 40mm from this end a series of holes were drilled to exhaust the gases after the projectile had fired. The final modification to the barrel tube was to cut a breach into which the sabot and projectile could be loaded. This was then covered by a semi-circular section and a collar to hold it in place. The whole assembly is shown in figure 6.4

For the reservoir design the internal volume and wall thicknesses were already set. The diameter was decided by the biggest size tube of the correct wall thickness that could be found and so the length needed was found to be 500mm. One end plate was a simple circle with bolt holes at the circumference and a hole at the centre to fit the gas feed.

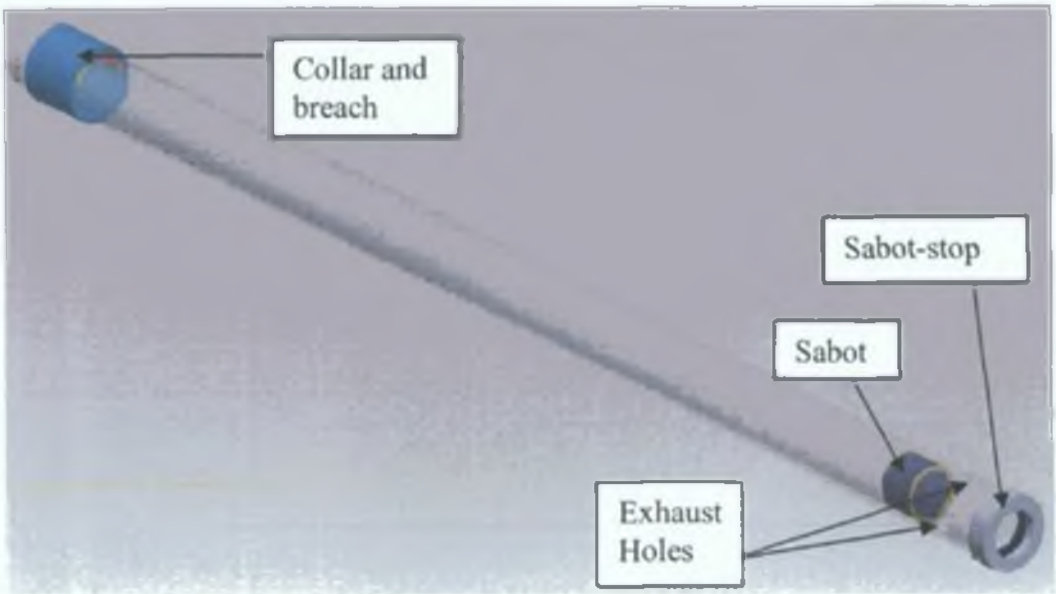

Figure 6.4: Barrel Assembly

The other end plate was cone shaped to ensure that the gas would escape into the barrel at the highest possible velocity with the minimum of losses. At the end of the cone was a threaded section to attach to the valve. The complete reservoir is shown in figure 6.5

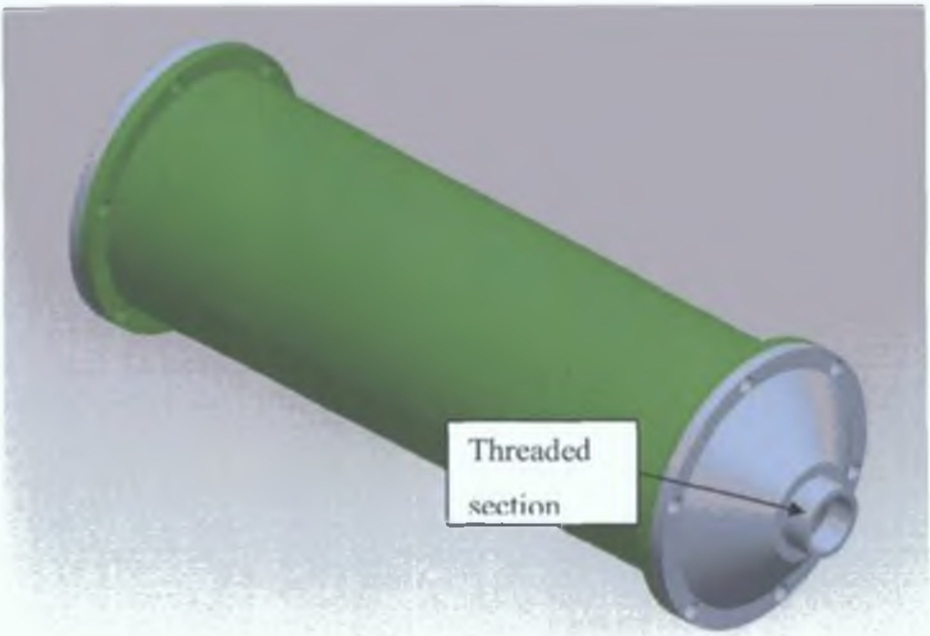

Figure 6.5: Reservoir

6.5 Clamping and Tilting Mechanism

One of the main aims of this design process was to be able to accommodate test plates with an area 0.5m^2. The clamping mechanism on the old rig was not designed very well so instead of just scaling it up it was decided to redesign it completely. To simulate real aircraft structure behaviour it was decided to clamp the plate on all four sides. This resulted in the design seen below in figure 6.6.

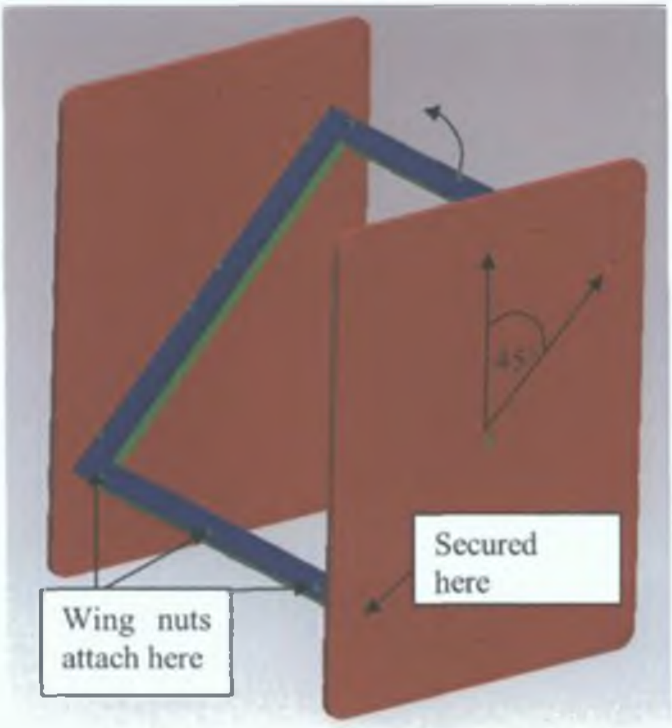

Figure 6.6: Clamping and tilting mechanism

The bottom clamp has threaded bars which protrude through holes in the top clamp. Wing nuts are fastened to them to produce the clamping pressure. The bottom clamp is actually made from four strips bolted together. This was required to save on the costs of buying a large plate 10mm thick. The bottom clamp needs to be this thick to accommodate the dowel on which the whole clamp rotates. The clamps can rotate through 45° on their mounting plates and are secured by bolts that fit into holes at the ends of the bottom clamp.

6.6 Sliding Mechanism

The sliding mechanism was designed so that the test plate could be moved through 0.5m in the plane perpendicular to the barrel with the aim being the ability to impact the plate at any point. It consists primarily of two pairs of rails with attached carriages that enable the plate to be moved vertically and horizontally, see figure 6.7. The rails and carriages were sourced from Rhino products. Initially they were both to be locked in place using heavy duty magnetic clamps for quick and easy use but unfortunately the assembly proved too heavy for the clamps and travel in the vertical direction was constrained using a clamp bolted to the frame.

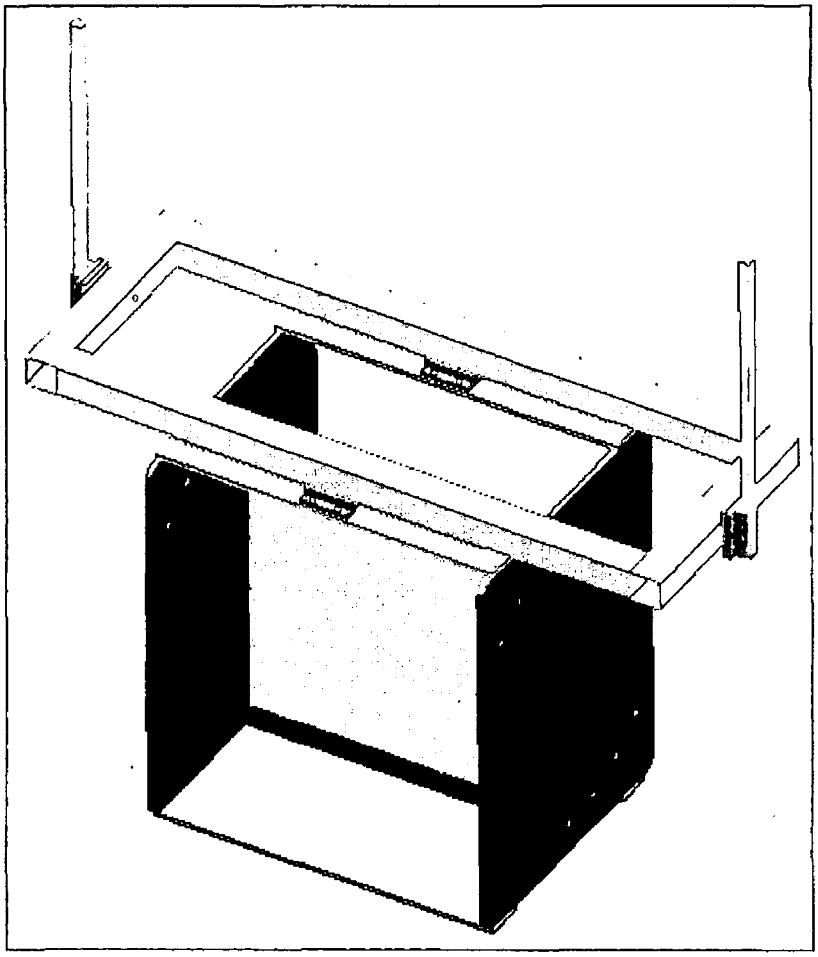

Figure 6.7: Rails and clamp assembly for moving the test plate in the x-y plane

6.7 Final Design Issues

At this point all the aims outlined for the design of the new impact testing rig had been met and the only issues remaining were safety and the overall assembly. A frame was designed to hold both the barrel and the clamping assembly from box steel and this was covered with sheet aluminium to prevent the projectile from escaping when it is fired. A trap was designed at the rear of the frame to catch projectiles that penetrated the test plates. This consisted of an angled plate at the same height as the barrel and an enclosure. The idea was that the projectiles impact on the angled plate would change its direction through 90° and it would come to stop in the enclosure.

Safety was the main reason behind the aluminium sheet that covered the frame but it was necessary to hinge most of the sheets and make doors for access. As a result safety switches were installed on all the doors to ensure they were closed during operation of the projectile launcher. The switches were wired in series with the power to the valve actuator so that if any door was open no electricity would flow and it would be impossible to open the valve. In addition to this a key switch was also wired in series with the power to the valve no that no unauthorised person could activate the rig. The wiring diagram for the switches and valve is shown below in figure 6.8.

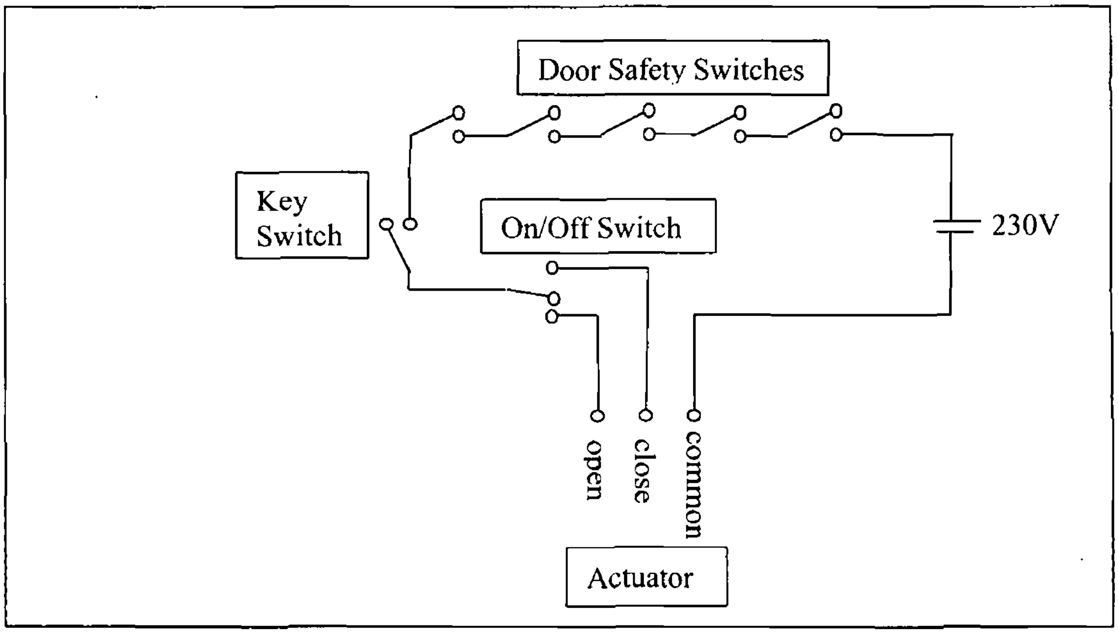

Figure 6.8: Rig Wiring Schematic

The On/Off switch shown is a button switch that opened the valve then pressed and closed the valve when released.

The final assembly drawing of the new gas powered projectile launcher is shown below in figure 6.9. This was submitted with the working drawings (see appendix 2) to the work shop in Dublin City University to be manufactured. It was completed with minimal changes to the design. When the work was finished in the workshop the rig was wired, the velocity measuring system from the old test rig was transferred to the new rig and the high pressure nitrogen cylinder was plumbed in. The rig was then ready to be tested.

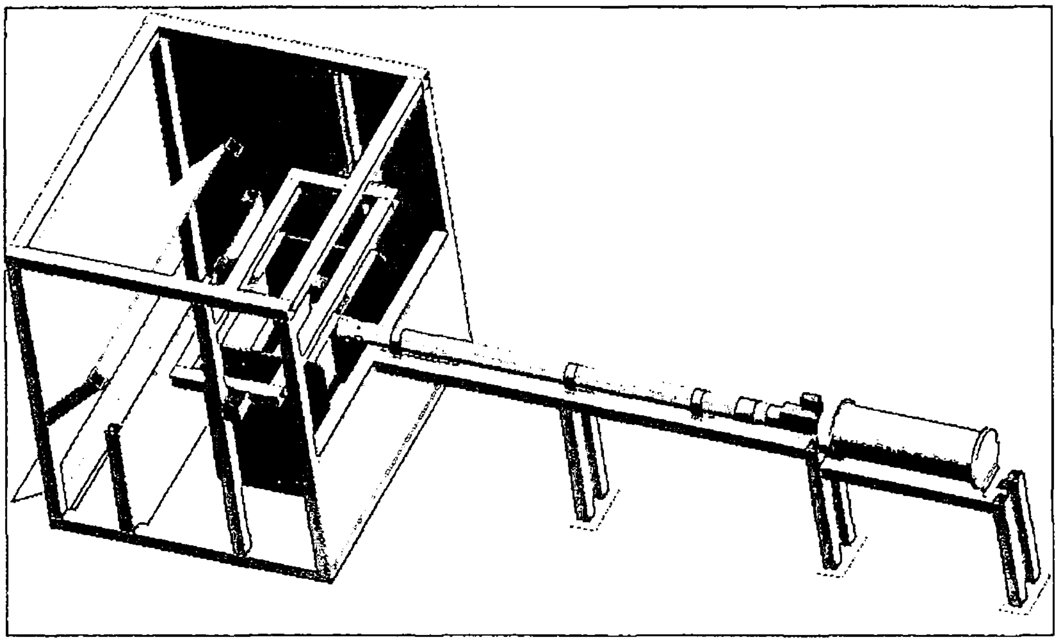

Figure 6.9: Full gas powered projectile launcher assembly

6.8 Problems Encountered with the Completed Impact Test Rig

As one would expect with a completely new design all of the problems with the new impact testing rig had not been solved in the design phase. The first problem that was apparent was that the motorised valve operated too slowly. For the previous test rig the valve was operated by a solenoid and so opened almost instantaneously. The motorised valve, however, took several seconds to open and restricted the gas escaping from the reservoir. This resulted in a lower gas velocity and hence a lower sabot and projectile velocity than anticipated.

Unfortunately the valve manufacturer did not supply an actuator that could open the valve faster as all of their actuators were designed with laminar flow in mind. To ensure that the theory presented in section 6.2.1 for the possible sabot velocity was correct the actuator was removed and the valve was operated manually. A series of tests were conducted and the results showed that it was possible to reach a projectile velocity of 200m/s without difficulty. Unfortunately it was not possible to operate the valve continuously on a manual basis as all of the safety features were built into the electrical actuation. Possible alternative actuators for the valve would include other electric motors, rotary pneumatic actuators or solenoid actuators, as in the original test rig. These options are currently being investigated by the researchers assigned to continue with the project.

One other problem that occurred with the final design was that the Teflon plate at the front of the sabot deformed slightly on impact with the sabot stop. The deformation resulted in the sabot being unable to fit back into the barrel. Placing a mild steel plate in front of the Teflon plate solved the problem.

6.9 Summary of Chapter 6

A new gas powered projectile launcher was designed and manufactured. Its capabilities included:

- a clamping mechanism capable of taking a test plate 500mm^2 in area
- a titling mechanism on the clamp to allow impact at oblique angles
- a sliding mechanism to allow impact at any point on the plate
- a barrel and sabot design that allowed the rig to accommodate projectile of any shape and size up to a maximum diameter of 50mm

Some problems were encountered with the sabot and the valve actuation and solutions were provided in the case of the sabot design. An investigation into the valve actuation problem is continuing.

7. Discussion

7.1 Analysis of Simple Plate Structures

An experimental analysis was carried out with a gas-powered projectile launcher. Results from the tests showed three modes of deformation; dishing of the plate without perforation, perforation with petalling of the plate and full penetration with either perforation or plugging. The failure modes were much as expected in thin aluminium plates with shear plugging being the dominant failure mode. Petalling occurred mostly in tests where the projectile failed to penetrate the plate completely. The tearing observed may have occurred due to slightly oblique impacts of the projectile. If such impacts occurred they would have resulted in a sharp edge impacting the plate first with indentation of the plate taking place before the rest of the projectile face could come in contact with the plate. The result observed from this would have been for one side of the projectile to penetrate the plate first possibly causing the tearing damage seen. Unfortunately there was no possible way of knowing if such an oblique impact had occurred during the experimental testing. The height of the deformation was also within expected ranges although the increase in the height after the ballistic limit (see figure 4.14) was not as seen in previous research [16]. It is thought that the additional petals caused by radial cracks around the hole are responsible and that the height of the deformation would decrease again if the projectile velocity was increased further.

The finite element simulation was conducted using the LS-DYNA explicit finite element code because of its proven ability to solve dynamic problems. Ansys was used as a pre-processor, and initially as the post-processor, because of previous experience with Ansys and LS-Prepost was used as the post-processor after difficulties were experienced with the size of the file in Ansys. Much thought was given to the material model to be used in the finite element analysis with the temperature and strain-rate sensitive Johnson-Cook model initially considered. Unfortunately, a large number of material parameters are needed to formulate this material model completely and the experimental facilities did not exist to obtain them. Instead the nonlinear kinematic hardening model was used (see table 4.2). This model has a bilinear stress-strain curve with a combination of isotropic and kinematic hardening. Material strain-rate sensitivity could be accounted for by the user using the Cowper-Symonds strain-rate model. Initial analyses were performed without these strain-rate parameters but accounting for strain-rate behaviour in the material improved the model's accuracy with regard to the experimental results.

The elements chosen for the simulation were 164 solid elements. Shells elements were considered but were rejected due to their inability to have contact on both sides of the element. This was not a concern with the simple plate but was necessary when higher assemblies with stringers were considered. The mesh density was seen to be an extremely important factor in the FE simulation. An investigation observed that four elements were needed through the thickness of the plate and 155 along each side to provide an accurate solution. This equated to elements less than 0.94mm^2 in area and only 0.25mm thick. The reason that such small elements were necessary was because of the failure mode. The shear bands that cause shear plugging have been observed to be in the region of 100-300μm [19].

The contact algorithm used in the model was the eroding surface to surface contact option. It was used so that through-thickness penetration could occur in the simulation. It was observed that the accuracy of this algorithm depended on the levels of sliding interface energy generated between the two surfaces. A positive value would lead to parts penetrating through each other without causing damage while too negative a value could lead to instability and an inaccurate solution. The sliding interface energy levels were controlled by the sliding interface penalty factor (SIPF) and it was seen that for the simple plate problem a value of 0.015 was ideal (see figure 4.9).

Overall the finite element solution gives good correlation to the experimental testing with the ballistic velocity for the plate predicted to within 10% and most of the deformation modes observed. The absence of a significant gap between the velocities needed to induced partial perforation with petalling and those needed for plugging may have been due to the simplistic material model and the fact that, due to the lack of temperature dependence, there could be no thermal softening. The height of the deformation at the point of impact was seen to match up well with the experimental results for two of the three deformation modes. For the plugging case the finite element model showed a decreasing deformation trend after the ballistic limit, something that was seen in previous research. The experimental tests showed an increase in this case, however, as already mentioned caused by the secondary petals. The inability of the eroding failure mechanism to reproduce cracks explains why this increase is not seen in the FE analysis and also explains the lack of petals with tearing.

7.2 Analysis of Impact to Riveted Sheet Metal Structures

An experimental analysis was again undertaking with the projectile launcher pictured in figure 4.1. Right-angled sections of aluminium were riveted to plate of the same material initially with pop-rivets, however as pop-rivets are not recognised as aircraft standard rivets, solid Al 2117 – T4 rivets were obtained and used. These rivets are commonly used for aircraft repairs and were chosen because they can be driven cold without any special preparation. The results of the tests showed similar plugging failure to that seen for the simple plate in section 4.2. The rivets were seen to fail by shear in most cases with rivets pulling out of the plates only where cracks reached the edge of the rivet hole. Full ballistic penetration of the plate and angle was observed for the pop-rivet assembly at approximately 300m/s but was not observed for the solid rivet assembly as too high a projectile velocity was required was too high. It is assumed that it would occur somewhere in the 350-400m/s range if the pattern seen in the pop-rivet case continued.

The finite element modelling of the riveted plate structure concentrated on the modelling of the rivets. A full 3D model was created to try to get an accurate model of the problem, however, this was not the case. The rivets failed through shear just as in the experimental tests but their failure occurred at a much lower projectile velocity. The rivets in this case were idealised and had not experienced any deformation or initial stresses as would be present in a real rivet. Thus it was decided to induce these effects in the rivet to see if it would behave closer to that observed in the experimental analysis. To this end a pretension was applied in the implicit solver Ansys which induced strains of 1×10^{-3} in the plate and rivets. These strains were then used as initial conditions in the explicit analysis where the assembly was impacted by the titanium projectile. Unfortunately the results were disappointing with the difference between the model with pretension and without being minuscule. The coarse mesh that resulted from a restriction on the number of elements allowable in Ansys may have had a significant effect on the results and it is also possible that pretension is not a good enough method to simulate the riveting process. The effects of the riveting process and the non-linear behaviour of rivet assemblies are still thought to be the factors causing the significant errors in the finite element results.

The second half of chapter 5 saw an investigation into 2D rivet approximations. Actually the models were 1D nodal constraints but since they were grouped together in a planar shape equal to the area of the rivet head they were known as 2D approximations. Two sets of 2D approximations were looks at; those with failure and those without. The rivet models with failure were based on the ultimate tensile and shear failure strengths of the rivet material. Initially two areas, equal to the cross-sectional area of the rivet, were constrained on the adjoining surfaces of the plate and angle. The results of this simulation saw the rivets fail much earlier than even the 3D rivet model. It was decided that if the rivet was assumed to create a solid component until failure that it could be modelled by constraining two regions at opposite sides of the plate and angle instead. This model, still based on the shear and tensile material behaviour, behaved much more like the 3D rivet model with deformations occurring at the same projectile velocities. The behaviour was still nothing like that observed in the experimental testing which was not a surprise as the failure mechanism based on two fixed values could not be expected to simulate the complex non-linear rivet behaviour. The second 2D model, however, did not try and predict the behaviour at all as it had no failure criterion. Instead it worked on the assumptions that rivet joints can fail by the riveting pulling out of the plate. Even though this did not occur in the experimental analysis presented it has been observed in other literature [10]. The same geometry as the previous 2D model was used with areas from opposite sides of the plate and angle being constrained. The results showed these rivet joints to more robust with failure occurring at similar projectile velocities to the pop-rivet assembly in the experimental testing. The mode of failure was validated with the plate failing by element erosion simulating the rivets pulling out of the plate. The ballistic velocity however was still underestimated by 25-30% when compared with the solid rivet assembly and this suggests that new rivet approximations are still necessary to model these nonlinear fasteners correctly and cheaply.

7.3 Design and Manufacture of Gas-powered Projectile Launcher

With the limitations of the old impact testing rig in mind a new gas-powered projectile launcher was designed and manufactured. Its capabilities included a barrel and sabot assembly that could fire projectiles of any size and shape up to 50mm in diameter. The reason for this was to allow projectiles other than cylinders or spheres to be fired. It also allows for tumbling projectiles with the right sabot design. The large diameter was so soft debris, like the tyre rubber in the Concorde case [5], could be fired in sufficient masses to investigate their effects on structures. The angling of the test plate was another capability of the new impact rig which was obviously designed with oblique impacts in mind. The sliding mechanism was included to enable the plate to be impacted at any point on its area and also to facilitate research into multiple impacts on plates where the residual stresses and strains of earlier impacts may affect a later one. Finally the idea behind the large test plate size was that a test plate with multiple stringers at the correct spacing could be accommodated and that if a smaller plate was required that a simple adaptor could be made so that it would fit.

Several other improvements to the new impact testing rig are possible given the time and budget. Obviously fixing the problem with the valve actuation should be top of the list. The valve itself operates perfectly and does not require too much torque to open and close. With that in mind it should not be difficult to find a solution. A stepper motor would be ideal if one could be found with sufficient torque. Another option would be a rotary pneumatic actuator. Its control values could be controlled electrically so that it could be tied into the safety switches on the doors. A solenoid switch might prove difficult to integrate with the present valve but if possible would definitely open the valve quickly enough to avoid restrictions on the flow.

One other improvement considered early on and investigated fully was that of a high speed camera. The camera would serve several functions, replacing the need for the laser velocity measurement system, checking the angle of attack of the projectile, obtaining images of the impact event itself and calculating the residual projectile velocity. Unfortunately the cost of the camera was prohibitive ruling it out for this project, however it should be considered in the future.

Measuring the residual velocity of the projectile was mentioned above and has been observed in literature [6-10] as a common parameter measured in ballistic plate impact testing. Even without the digital camera it should be possible to implement this although the laser system used for the initial velocity measurement would not be suitable as it would be difficult to predict the exact path or orientation of the projectile after impact. An alternative method observed in literature [e] has been to use two self inducting coils placed a known distance apart in the path of the projectile and observing the time between signals induced by the projectiles passage.

8. Conclusions and Recommendations

8.1 Conclusions

A finite element model was created to simulate the impact of a titanium projectile on a simple plate using the LS-DYNA explicit code. The model correlated well to results from experimental testing undertaken with regards to ballistic velocity of the plate, height of final deformation and deformation shapes. Small errors, in the region of 10%, were seen for the velocity needed to perforate and penetrate the plate. The finite elements prediction of the height of deformation was accurate except in the case of full penetration where the models inability to simulate the radial cracks at the hole resulted in it underestimating the deformation.

A more complex assembly which included a stringer and rivets was analysed experimentally and computationally. The experimental analysis was conducted using both pop-rivets and aircraft standard rivets. Two separate approaches were attempted for modelling the rivets using full 3D modelling and using 2D approximations. It was concluded that the 3D model failed to predict the rivet behaviour correctly even when the effects of the riveting process were taken into account. The 2D approximations that took rivet failure into account was also disappointing with similar behaviour to the 3D model, however some improvement was shown for the 2D approximation without rivet failure. This model proved to have behaviour closest to that observed during the experimental testing with good correlation to the pop-rivet assembly's behaviour. When compared with the solid rivets, however, the results were still poor with an error in the region of 30%.

Lastly, a new gas-powered projectile launcher was designed and manufactured. Innovations in this design included:

- the ability to test plates of up to 0.5m^2
- the ability to impact the plate at oblique angle up to 45°

- the ability to fire projectile of any shape or size up to 50mm in diameter
- and the ability to impact the plate at any point on its surface.

The manufacture of the new rig was completed successfully and the rig operated as expected with the only problems encountered being valve actuation and some slight sabot deformation.

8.2 Recommendations

One of the main difficulties encountered during this project has been the modelling of the rivets. Further work should be carried out to investigate their nonlinear behaviour and to develop an accurate, cost effective model to use in industry.

One aspect of the material model that was not investigated thoroughly but which may be significant was the failure strain. An average value was used due to the extensive material testing needed to properly determine the failure strain for the material and appeared to be quite accurate in the case of the simple plate. An investigation into the effects of varying this parameter should be undertaken.

With regard to impacts to plate structures this project only examined a tiny portion of the field. The new test rig was design so that further research could be carried out. Some suggestions as to the direction this work should take are:

- examination of the effects of different shape projectile
- examination of oblique and tumbling projectile impacts
- examination of the effects of multiple stringers on a plate
- examination of multiple impacts to a plate
- examinations of other materials such as composite and sandwich structure

Reference

1. Society of Automotive Engineers Committee on Engine Containment, Report on Engine Containment, SAE-AIR-4003, September 1987.
2. Federal Aviation Authority, Design considerations for minimizing hazards caused by uncontained turbine engine and auxiliary power unit failure. FAA Advisory Circular, No. 20-128A, 1997.
3. National Transportation Safety Board Aircraft Accident Report, Uncontained Engine Failure Delta Air Lines Flight 1288, McDonnell Douglas MD-88, N927DA, Pensacola, Florida, July 6, 1996
4. E. C. Cleary, R. A. Dolbeer, S. E. Wright, Wildlife strike to civil aircraft in the United States 1990-2002, FAA National Wildlife Strike Database Serial Report Number 9, June 2003.
5. Accident on 25 July 2000 at "La Patte d'Oie" in Gonesse (95) to the Concorde registered F-BTSC operated by Air France, Interim Report, Dec 2001.
6. K. Carney, M. Pereira, D. Revilock, P. Matheny, Jet Engine Fan Blade Containment using two different geometries, 4th European LS-DYNA Users Conference, Ulm, Germany 2003.
7. S. J. Lundin, Engine Debris Fuselage Penetration Testing, Phase I, FAA Report DOT/FAA/AR-01/27, 2001
8. C.E. Frankenberger, Large Engine Uncontained Debris Analysis, FAA Report DOT/FAA/AR-99/11, 1999
9. N. F. Knight Jr, N. Jaunky, R. E. Lawson, D. R. Ambur, Penetration simulation for uncontained engine debris impact on fuselage-like panels using LS-DYNA, Finite Elements in Analysis and Design Vol. 36,2000, 99-133
10. B. Langrand, E. Deletombe, E. Markiewicz, P. Drazeh, Riveted joint modelling for numerical analysis of airframe crashworthiness, Finite Elements in Analysis and Design Vol. 38, 2001, 21- 44.

11. G. G. Corbett, S. R. Reid, W. Johnson, Impact loading of plates and shells by free-flying projectiles: A review, International Journal of Impact Engineering Vol. 18, Issue 2, 1996, 141-230.
12. T. Borvik, M. Langseth, O.S. Hopperstad, K.A. Malo, Perforation of 12mm thick steel plates by 20mm diameter projectiles with flat, hemispherical and conical noses Part I: Experimental study, International Journal of Impact Engineering, Vol. 27, 2002, 19-35.
13. R. S. J. Corran, P. J. Shadbolt, C. Ruiz, Impact loading of plates - An experimental investigation, International Journal of Impact Engineering, Vol. 1, 1983, 3-22.
14. W. Q. Shen, N. O. Rieve and B. Baharun, A study on the failure of circular plates struck by masses. Part 1: experimental results, International Journal of Impact Engineering Vol. 27, 2002, 399–412.
15. W. Goldsmith, S. A. Finnegan, Penetration and perforation processes in metal targets at and above ballistic velocities, International Journal of Mechanical Science, Vol. 13, 1971, 843-866.
16. N. Levy, W. Goldsmith, Normal impact and perforation of thin plates by hemispherically-tipped projectiles – II. Experimental results, International Journal of Impact Engineering, Vol. 2, 1984, 299-324.
17. S. Deya, T. Børvika, O.S. Hopperstada, J.R. Leinumc, M. Langsetha, The effect of target strength on the perforation of steel plates using three different projectile nose shapes, International Journal of Impact Engineering Vol. 30, 2004, 1005-10038
18. T. Borvik,b, A. H. Clausena, O. S. Hopperstada, M. Langsetha, Perforation of AA5083-H116 aluminium plates with conical-nose steel projectiles—experimental study, International Journal of Impact Engineering Vol. 30, 2004, 367-384.
19. X.W. Chen, Q.M. Li, Shear plugging and perforation of ductile circular plates struck by a blunt projectile, International Journal of Impact Engineering Vol. 28, 2003, 513–536.
20. X. W. Chen, Q. M. Li and S. C. Fan, Initiation of adiabatic shear failure in a clamped circular plate struck by a blunt projectile, International Journal of Impact Engineering Vol. 31, 2005, 877–893.

21. S. Leppin, R. L. Woodward, Perforation mechanisms in thin titanium alloy targets, International Journal of Impact Engineering, Vol. 4, 1986, 107-115.

22. V. F. Nesterenko, W. Goldsmith, S. S. Indrakanti, YaBei Gu, Response of hot isostatically pressed Ti–6Al–4V targets to normal impact by conical and blunt projectiles, International Journal of Impact Engineering Vol. 28, 2003, 137-160.

23. M. Langseth and P. K. Larsen, Dropped objects' plugging capacity of steel plates: An experimental investigation, International Journal of Impact Engineering, Vol. 9, 1990, 289-316.

24. W. Goldsmith, S. A. Finnegan, Normal and oblique impact of cylindro-conical and cylindrical projectiles on metallic plates, International Journal of Impact Engineering, Vol. 4, 1986, 83-105.

25. K. Li and W. Goldsmith, A phenomenological model for perforation of moderately thick plates by tumbling projectiles, International Journal of Solids Structures Vol. 33, 1996, 3561-3575.

26. T. Børvik, O. S. Hopperstad, T. Berstad and M. Langseth, Numerical simulation of plugging in ballistic penetration, International Journal of Solids and Structures Vol. 38, 2001, 6241-6264.

27. T. Børvik O. S. Hopperstad, T. Berstad and M. Langseth, Perforation of 12 mm thick steel plates by 20 mm diameter projectiles with flat, hemispherical and conical noses Part II: numerical simulations, International Journal of Impact Engineering Vol. 27, 2002, 37-64.

28. G. Shi, J. Guo, C. Lu, Efficient modelling of panel-like targets in perforation simulation, 3rd LS-DYNA European users conference, Paris France, 2001.

29. D. C. Webb, K. Kormi, S. T. S. Al-Hassani, The influence of inertia and strain-rate on large deformation of plate-structures under impact loading, Computers and Structures Vol. 79, 2000, 1781-1797.

30. H. Kurtaran, M. Buyuk, A. Eskandarian, Ballistic impact simulation of GT model vehicle door using finite element method, Theoretical and Applied Fracture Mechanics Vol. 40, 2003, 113-121.

31. M. Park, J. Yoo , D. Chung, An optimization of a multi-layered plate under ballistic impact, International Journal of Solids and Structures, Vol. 42, 2005, 123–137.
32. R. P. Gogolowski and B. R. Morgan, FAA DOT/FAA/AR-01/21Ballistic Experiments With Titanium and Aluminium Targets, Report DOT/FAA/AR-01/21, 2001
33. D. Liu, W.J. Stronge, Ballistic limit of metal plates struck by blunt deformable missiles: experiments, International Journal of Solids and Structures, Vol. 37, 2000, 1403-1423.
34. R. D. Buehrle, G. A. Fleming, R. S. Pappa, F. W. Grosveld, Finite Element Model Development And Validation For Aircraft Fuselage Structures, 18th International Modal Analysis Conference, San Antonio, Texas, 2001
35. X. Teng and T. Wierzbicki, Numerical study on crack propagation in high velocity perforation, Computers and Structures, Vol. 83, 2005, 989–1004.
36. R.L. Veldman, J. Ari-Jur, C. Clum, J. Folkert, Effects of Pre-Pressurisation on plastic deformation of blast-loaded square aluminium plates, 8th International LS-DYNA Users Conference, Michigan, USA, 2004.
37. M. Anghileri, L. M. L. Castelletti, F. Invernizzi, M. Mascheroni, A survey of numerical models for hail impact analysis using explicit finite element codes, International Journal of Impact Engineering, Vol. 31, 2005, 929–944.
38. W. Johnson, Impact Strength of Materials, Edward Arnold, 1972.
39. N. Jones, Structural Impact, Cambridge Univeristy Press, 1989.
40. V. L. Kolmogorov, A method for calculating the stress-strain state in the general boundary value problem of metal forming: part 1, International Journal of Solids and Structures, Vol. 36, 1999, 1253-1262.
41. Prager, W., An introduction to plasticity, Addison-Wesley, 1959.
42. Subhash C. Anand, Frank E. Weisgerber, Usage of the Tresca yield condition in finite element plane strain analysis, International Journal of Solids Structures, Vol. 14, Issue 8, 1978, 625-637

43. E. H. Lee, and P. S. Symonds, Large Plastic deformations of beams under transverse impact, Journal of Applied Mechanics, Vol. 19, 1954, 308-335.
44. P. S. Symonds and T. Wierzbicki, Membrane mode solutions for impulsively loaded circular plates, Journal of Applied Mechanics, Vol. 46, Issue 1, 1979, 58-64.
45. M. Alves and N. Jones, Impact failure of beams using damage mechanics: Part II—Application, International Journal of Impact Engineering, vol 27 issue 8, 2002, 863-890.
46. X. Teng and T. Wierzbicki, Dynamic Shear Plugging of beams and plates with an advancing crack, International Journal of Impact Engineering, Vol. 31, Issue 6, 2005, 667-698.
47. Boeing Structural Repairs Manual, 1997.
48. A. M. S. Hamouda, A novel constitutive law for describing material behaviour at high strain rate and large deformation, PhD, Dublin City University, 1995.
49. R. D. Cook, D. S. Malkus, M. E. Plesha, Concepts and Applications of Finite Element Analysis – Third Edition, John Wiley & Sons, 1989.
50. D. A. Shockey, J. H. Giovanola, J. W. Simpson, D. C. Erlich, R. W. Kloop, S. R. Skaggs, Advanced Armor Technology: Application potential for engine fragment barriers for commercial aircraft, FAA Report DOT/FAA/AR-97/53, 1997.
51. J. Manchor and C. Frankenberger, Engine Debris Penetration Testing, FAA Report DOT/FAA/AR-99/19, 1999.
52. J. Spence and A.S. Tooth, Pressure Vessel Design – Concepts and Principles, E & FN Spon, 1994.

Appendix 1

Datasheets

Omal ART. 101 2-way full-bore threaded-ends brass ball valve

ART. 101

2-way full-bore threaded-ends brass ball valve

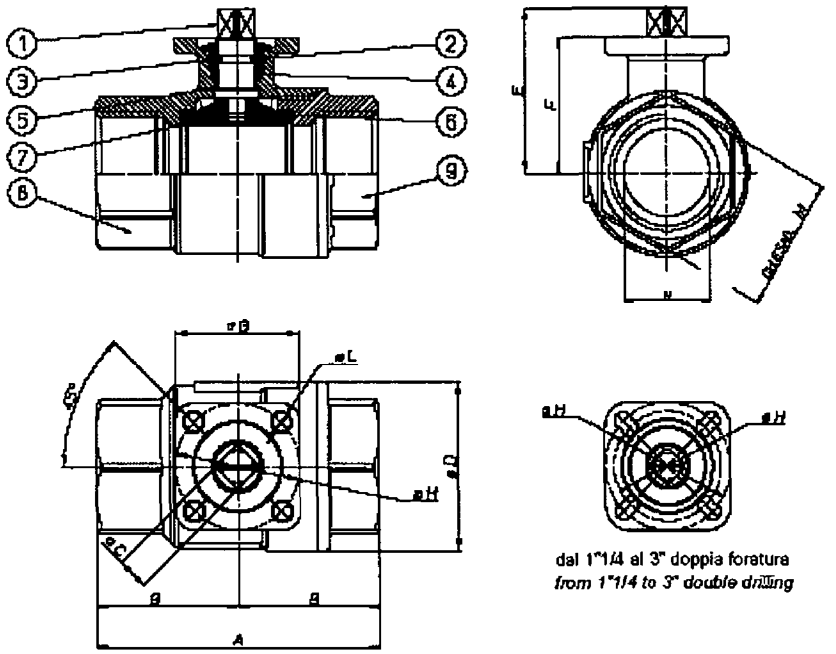

dal 1"1/4 al 3" doppia foratura
from 1"1/4 to 3" double drilling

MATERIALS		
1) Shaft	Brass	EN 12164 CW614N
2) O-Ring	FKM	
3) Gland nut	Brass	EN 12164 CW614N
4) Shaft seal	P.T.F.E.	
5) Antifriction rings	P.T.F.E.	
6) Seals	P.T.F.E	
7) Ball	Brass chromium plated	EN 12164 CW614N
8) Body	Brass	EN 12165 CW617N
9) Threaded ends	Brass	EN 12165 CW617N
Surface treatment: bright nickel plating		

DIMENSIONS

Size	A	B	C	oD	E	F	G	oH	oL	ch.M	N
3/8"	69	34,5	9	31,8	38,5	30,5	36	36	5,5	25	10
1/2"	69	34,5	9	31,8	38,5	30,5	36	36	5,5	25	15
3/4"	77	38,5	9	40	45,3	36,3	36	36	5,5	31	20
1"	89	44,5	9	48	49,2	40,2	36	36	5,5	38	25
1"1/4	103	51,5	9	60	60,5	51,5	42	36/42	5,5	47	32
1"1/2	114	57	9	70,6	67	58	42	36/42	5,5	54	40
2"	134	67	11	88,5	76,3	65,3	46	42/50	5,5/6,5	66	50
2"1/2	161	80,5	14	112	97	83	65	50/70	6,5/8,5	84	65
3"	185	92,5	14	138,4	108,5	94,5	65	50/70	6,5/8,5	98	80

Sabot Material: Ertalon 6PLA

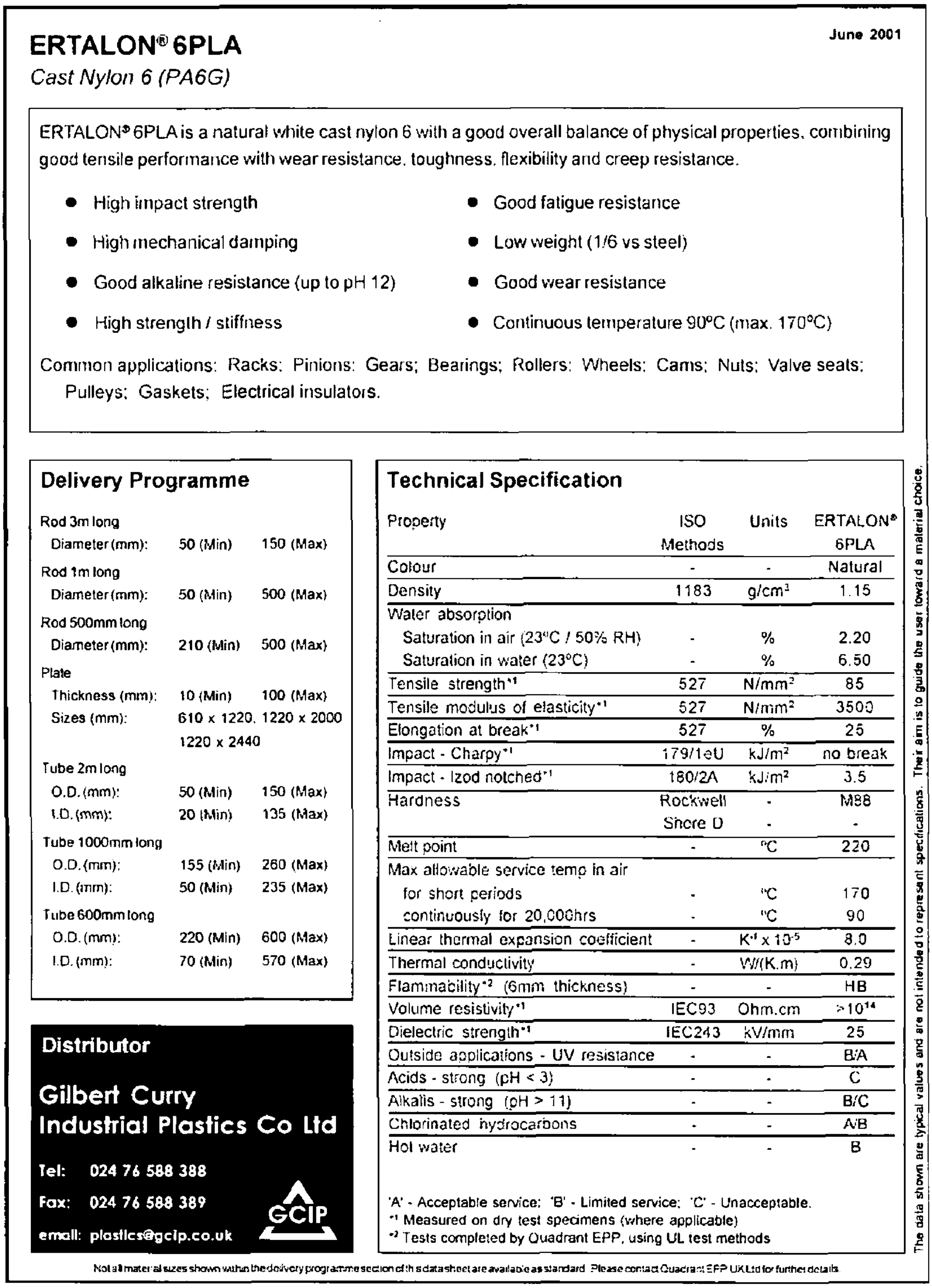

ERTALON® 6PLA

June 2001

Cast Nylon 6 (PA6G)

ERTALON® 6PLA is a natural white cast nylon 6 with a good overall balance of physical properties, combining good tensile performance with wear resistance, toughness, flexibility and creep resistance.

- High impact strength
- High mechanical damping
- Good alkaline resistance (up to pH 12)
- High strength / stiffness
- Good fatigue resistance
- Low weight (1/6 vs steel)
- Good wear resistance
- Continuous temperature 90°C (max. 170°C)

Common applications: Racks; Pinions; Gears; Bearings; Rollers; Wheels; Cams; Nuts; Valve seats; Pulleys; Gaskets; Electrical insulators.

Delivery Programme

Rod 3m long		
Diameter (mm):	50 (Min)	150 (Max)
Rod 1m long		
Diameter (mm):	50 (Min)	500 (Max)
Rod 500mm long		
Diameter (mm):	210 (Min)	500 (Max)
Plate		
Thickness (mm):	10 (Min)	100 (Max)
Sizes (mm):	610 x 1220, 1220 x 2000 1220 x 2440	
Tube 2m long		
O.D. (mm):	50 (Min)	150 (Max)
I.D. (mm):	20 (Min)	135 (Max)
Tube 1000mm long		
O.D. (mm):	155 (Min)	260 (Max)
I.D. (mm):	50 (Min)	235 (Max)
Tube 600mm long		
O.D. (mm):	220 (Min)	600 (Max)
I.D. (mm):	70 (Min)	570 (Max)

Distributor

Gilbert Curry Industrial Plastics Co Ltd

Tel: 024 76 588 388

Fax: 024 76 588 389

email: plastics@gcip.co.uk

Technical Specification

Property	ISO Methods	Units	ERTALON® 6PLA
Colour	-	-	Natural
Density	1183	g/cm^3	1.15
Water absorption			
Saturation in air (23°C / 50% RH)	-	%	2.20
Saturation in water (23°C)	-	%	6.50
Tensile strength^{*1}	527	N/mm^2	85
Tensile modulus of elasticity^{*1}	527	N/mm^2	3500
Elongation at break^{*1}	527	%	25
Impact - Charpy^{*1}	179/1eU	kJ/m^2	no break
Impact - Izod notched^{*1}	180/2A	kJ/m^2	3.5
Hardness	Rockwell	-	M88
	Shore D	-	-
Melt point	-	°C	220
Max allowable service temp in air			
for short periods	-	°C	170
continuously for 20,000hrs	-	°C	90
Linear thermal expansion coefficient	-	K^{-1} x 10^{-5}	8.0
Thermal conductivity	-	W/(K.m)	0.29
Flammability^{*2} (6mm thickness)	-	-	HB
Volume resistivity^{*1}	IEC93	Ohm.cm	>10^{14}
Dielectric strength^{*1}	IEC243	kV/mm	25
Outside applications - UV resistance	-	-	B/A
Acids - strong (pH < 3)	-	-	C
Alkalis - strong (pH > 11)	-	-	B/C
Chlorinated hydrocarbons	-	-	A/B
Hot water	-	-	B

'A' - Acceptable service; 'B' - Limited service; 'C' - Unacceptable.

^{*1} Measured on dry test specimens (where applicable)

^{*2} Tests completed by Quadrant EPP, using UL test methods

The data shown are typical values and are not intended to represent specifications. Their aim is to guide the user toward a material choice.

Not all material sizes shown within the delivery programme section of this datasheet are available as standard. Please contact Quadrant EPP UK Ltd for further details.

Laser for velocity measurement system

Self-Contained Helium-Neon Laser Systems 1500 Series | 2

Model 1500 Series Novette™ Self-Contained Helium-Neon Laser Systems

(Specifications in inches unless otherwise noted.)

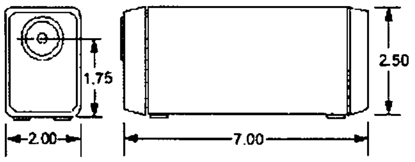

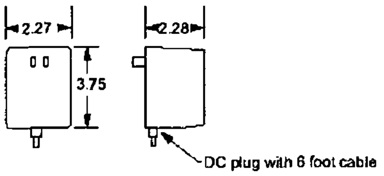

Specifications

Parameter	1507	1507P	1508	1508P
	Model 1500 Series Novette Laser Systems Model Number (note[1])			
Optical				
Minimum output power (TEM_{00}) 633 nm	0.8 mW	0.8 mW	0.5 mW	0.5 mW
Beam diameter ($1/e^2$ points, ±3%)	0.48 mm	0.48 mm	0.48 mm	0.48 mm
Beam divergence (±3%)	1.7 mrad	1.7 mrad	1.7 mrad	1.7 mrad
Minimum polarizaton ratio	N/A	500:1	N/A	500:1
Longitudinal mode spacing	1090 MHz	1090 MHz	1090 MHz	1090 MHz
Maximum noise (rms, 30 Hz to 10 MHz)	1.0%	1.0%	1.0%	1.0%
Maximum drift (note[2])	±2.5%	±2.5%	±2.5%	±2.5%
Maximum mode sweeping contribution	10%	10%	20%	20%
Maximum warm-up time (note[3])	10	10	10	10
CDRH class	IIIa	IIIa	II	II
Electrical				
Operating current				
AC at 120 V AC	150 mA	150 mA	150 mA	150 mA
AC at 220 V AC	82 mA	82 mA	82 mA	82 mA
AC at 100 V AC	N/A	N/A	N/A	N/A
Physical				
Weight	4.0 lbs.	4.0 lbs.	4.0 lbs.	4.0 lbs.

1. Add -1 for 120 V AC, -2 for 220 V AC, or -3 for 100 V AC operation. For example, 1507-2 will be configured for 220 V AC operation
2. Mean power measured over 8 hours
3. Minimum to 95% power

LINEAR

rino

AccuGlide™ T-Series™ Linear Ball Guides

AT-A - *A Style*

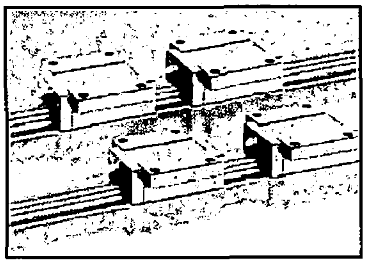

Material:

•Rail:	Aluminium with Steel strips
•Carriage:	Aluminium/Steel
•Speed:	Max. 3m/s acceleration 50m/s²
•Max. Temp:	80°C

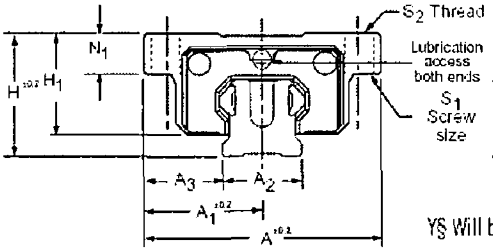

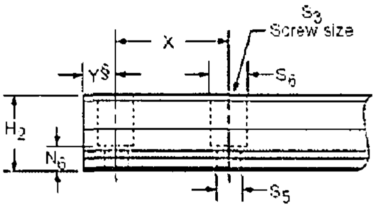

Y§ Will be equal on both ends, unless otherwise specified.

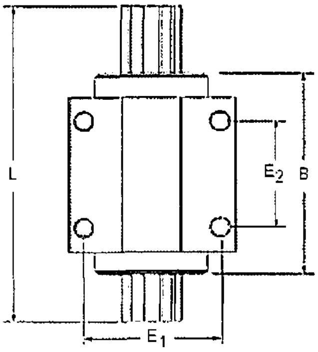

Ordering Information

When ordering a rail, please specify the number of carriages required (1,2,3, etc..) per rail.
for example: 1 x RT20AL1000 and 1 x AT20A

Please note: a minimum of 1 carriage must be ordered per rail. Carriages are dimensionally matched to rails during assembly.
Important - Carriages are not ball retained.

Type	Dimensions (mm)																			
	A	A_1	A_2	A_3	H	H_1	H_2	B	E_1	E_2	S_1	S_2	S_3	S_5	S_6	N_1	N_5	N_6	X	Max L
Series 20	63	31.5	20	21.5	30	25.0	18	76	53	40	M5	M6	M5	5.8	9.5	10.00	6.25	7.5	60	3000
Series 25	70	35.0	23	23.5	36	29.5	22	88	57	45	M6	M8	M6	7.0	10.7	12.00	8.00	10.0	60	3000
Series 35	100	50.0	34	33.0	48	40.0	29	117	82	62	M8	M10	M8	9.0	14.0	15.26	6.60	11.0	80	3000

Part Number		Load Ratings (at 100km)		Mass		Price 1 - 19 off	
Rail	Carriage	Dynamic (N) C	Static Co	Carriage kg	Rail kg/m	Rail per metre	Carriage
RT20AL1000	AT20A	9000	11000	0.22	0.79	£92.10	£40.99
RT25AL1000	AT25A	13000	15000	0.30	1.06	£100.40	£42.69
RT35AL1000	AT35A	25000	28000	0.74	2.27	£112.75	£80.52

A higher precision all steel version linear ball guide is also available. Please ask sales for details.

Modifications possible

Tel:+44 (0)1246 261300
Fax:+44 (0)1246 261688

Al 2014 –T4 Material

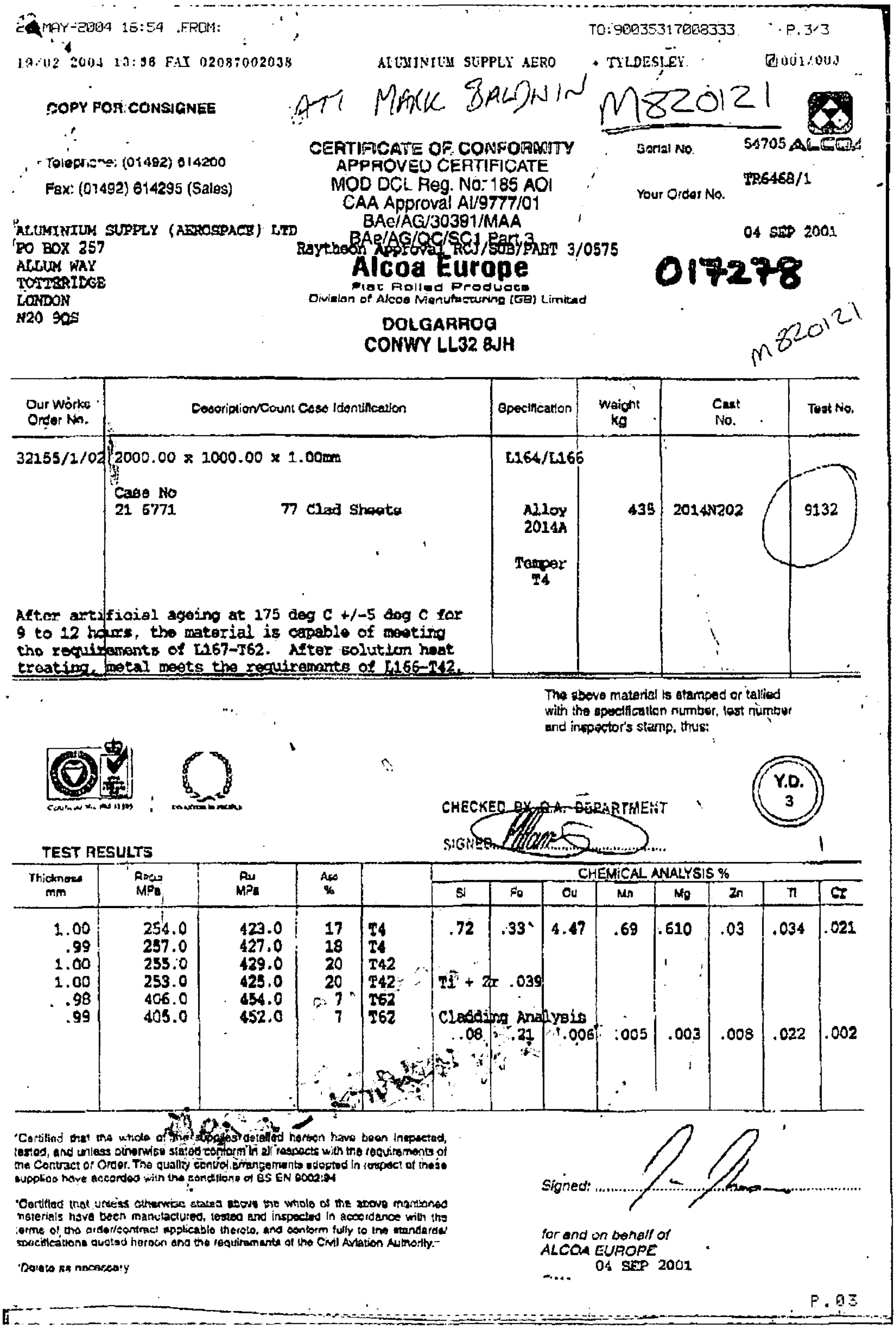

2 MAY-2004 16:54 FROM: TO:90035317008333 P.3/3

19/02 2004 13:36 FAX 02087002038 ALUMINIUM SUPPLY AERO → TYLDESLEY 001/003

COPY FOR CONSIGNEE

ATT MARK BALDWIN M820121

CERTIFICATE OF CONFORMITY
APPROVED CERTIFICATE
MOD DCL Reg. No: 185 AOI
CAA Approval AI/9777/01
BAe/AG/30391/MAA
BAe/AG/QC/SC1 Part 3
Raytheon Approval RCJ/SUB/PART 3/0575

Alcoa Europe
Flat Rolled Products
Division of Alcoa Manufacturing (GB) Limited

DOLGARROG
CONWY LL32 8JH

Serial No. 54705 ALCOA

Your Order No. TR6468/1

04 SEP 2001

017278

M820121

Telephone: (01492) 614200
Fax: (01492) 614295 (Sales)

ALUMINIUM SUPPLY (AEROSPACE) LTD
PO BOX 257
ALLUM WAY
TOTTERIDGE
LONDON
N20 9QS

Our Works Order No.	Description/Count Case Identification	Specification	Weight kg	Cast No.	Test No.
32155/1/02	2000.00 x 1000.00 x 1.00mm Case No 21 5771 77 Clad Sheets	L164/L166 Alloy 2014A Temper T4	435	2014N202	9132

After artificial ageing at 175 deg C +/-5 deg C for 9 to 12 hours, the material is capable of meeting the requirements of L167-T62. After solution heat treating, metal meets the requirements of L166-T42.

The above material is stamped or tallied with the specification number, test number and inspector's stamp, thus:

Y.D. 3

CHECKED BY Q.A. DEPARTMENT

SIGNED

TEST RESULTS

Thickness mm	$R_{p0.2}$ MPa	R_m MPa	A_{50} %		CHEMICAL ANALYSIS % Si	Fe	Cu	Mn	Mg	Zn	Ti	Cr
1.00	254.0	423.0	17	T4	.72	.33	4.47	.69	.610	.03	.034	.021
.99	257.0	427.0	18	T4								
1.00	255.0	429.0	20	T42								
1.00	253.0	425.0	20	T42	Ti + Zr .039							
.98	406.0	454.0	7	T62								
.99	405.0	452.0	7	T62	Cladding Analysis							
					.08	.21	.006	.005	.003	.008	.022	.002

*Certified that the whole of the supplies detailed hereon have been inspected, tested, and unless otherwise stated conform in all respects with the requirements of the Contract or Order. The quality control arrangements adopted in respect of these supplies have accorded with the conditions of BS EN 9002:94

*Certified that unless otherwise stated above the whole of the above mentioned materials have been manufactured, tested and inspected in accordance with the terms of the order/contract applicable thereto, and conform fully to the standards/specifications quoted hereon and the requirements of the Civil Aviation Authority.

*Delete as necessary

Signed:

for and on behalf of
ALCOA EUROPE
04 SEP 2001

P.03

Appendix 2

Working Drawings for New Gas-powered Projectile Launcher

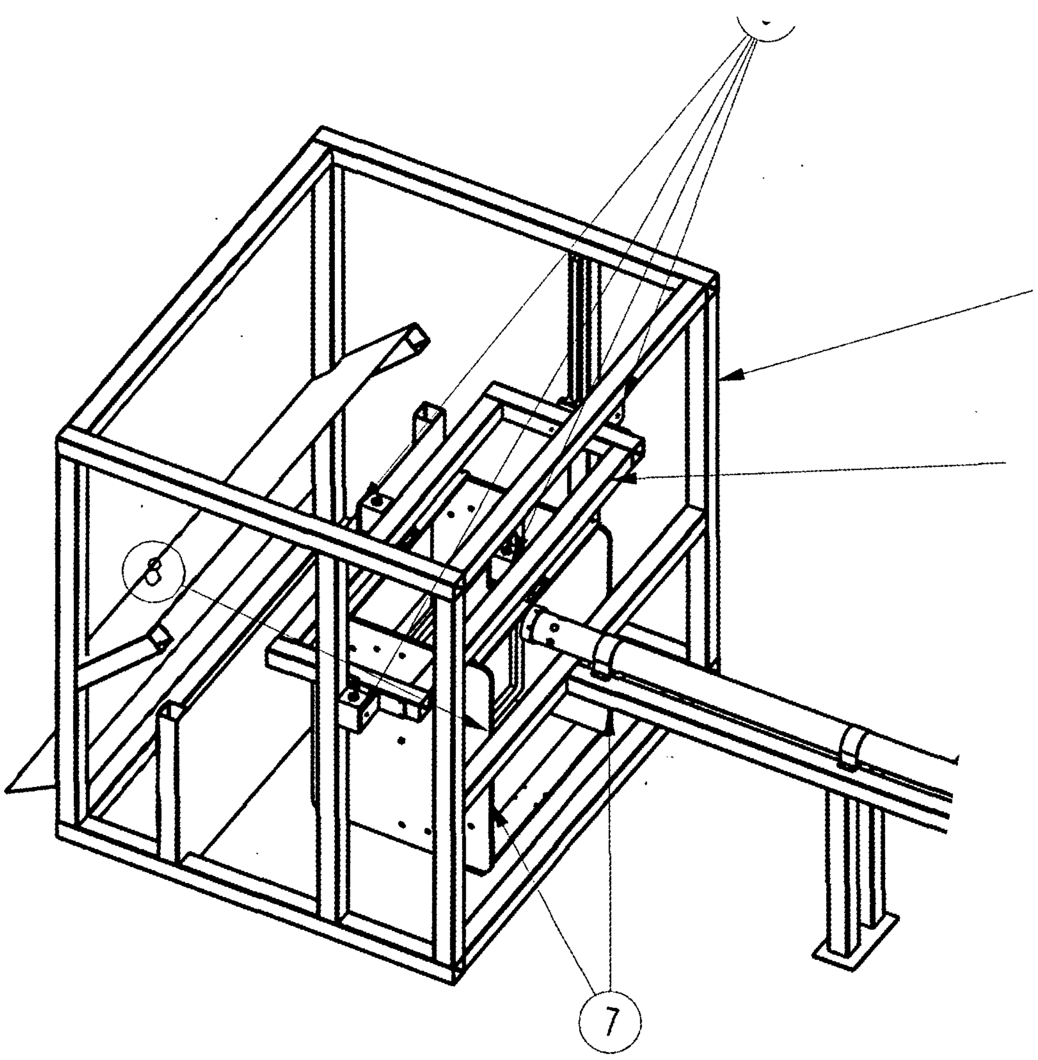
7

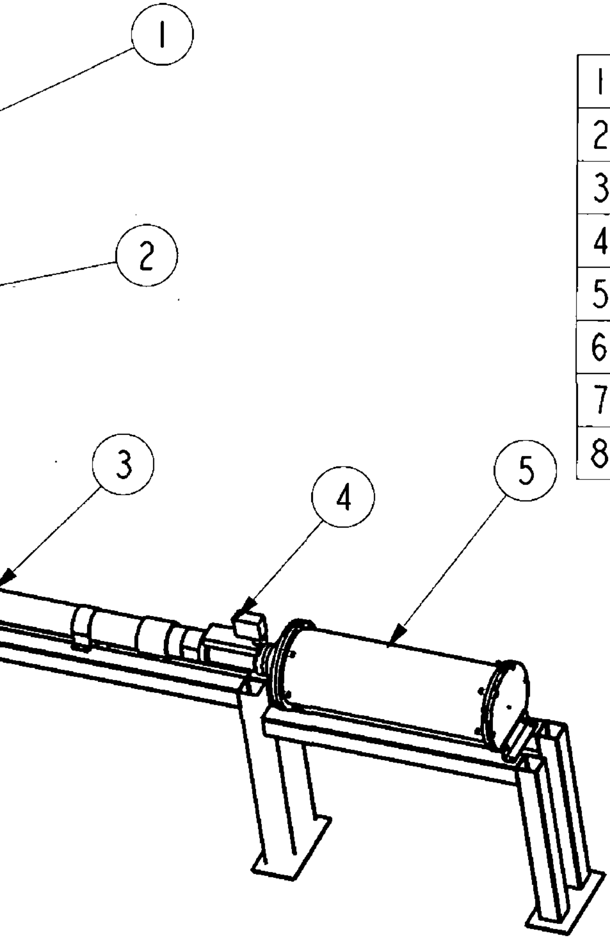

1	Main Frame
2	Slide Frame
3	Barrel
4	Solenoid Valve
5	Reservoir
6	Magnetic Clamps
7	Clamp Supports
8	Clamp

School of Mechanical and
Manufacturing Engineering

Name: Pierce Kennedy	Date: 15 March 2004
Part: Full Assembly	Notes:
Scale: 0.06	
Quantity: 1	

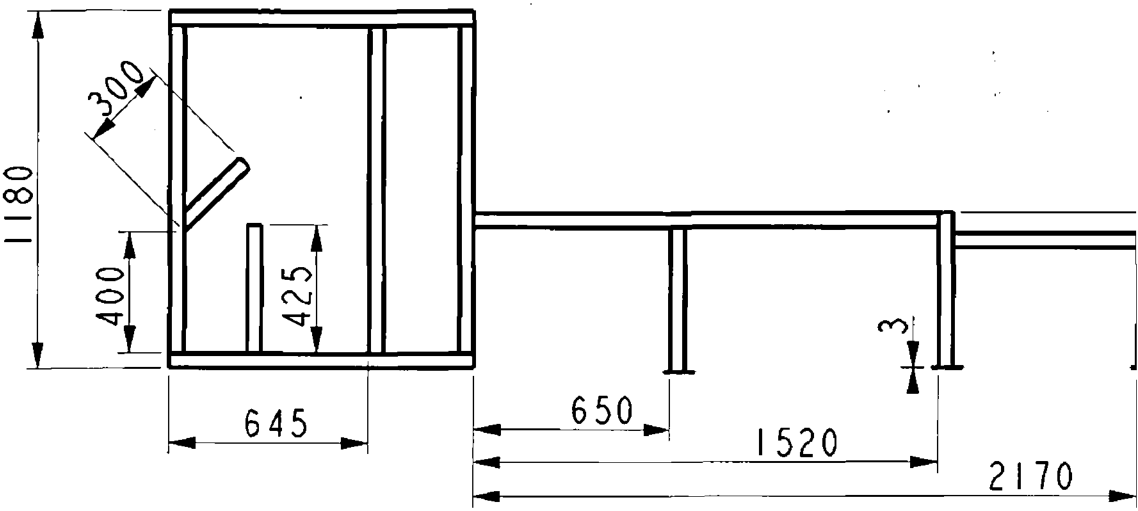
1180
300
400
425
645
650
1520
2170
3

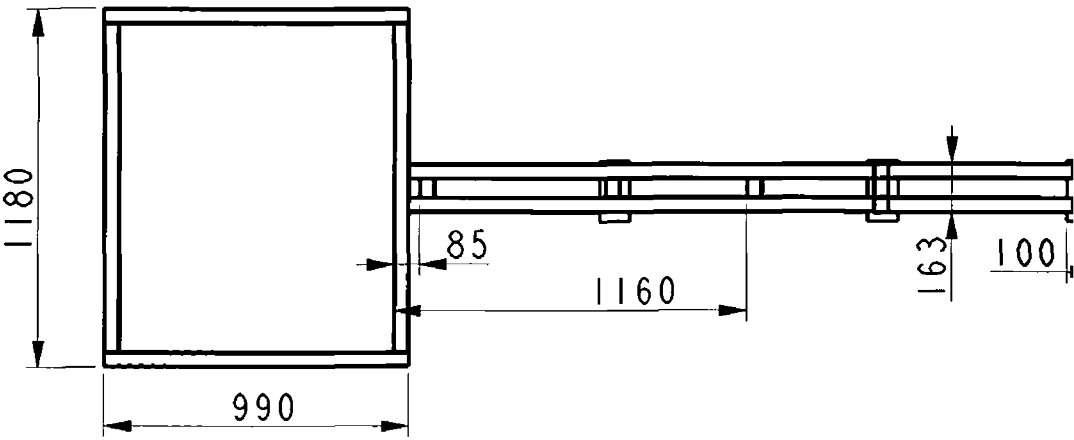
1180
85
1160
163
100
990

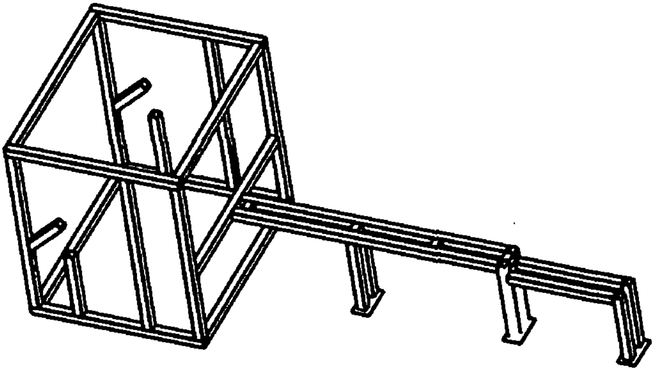

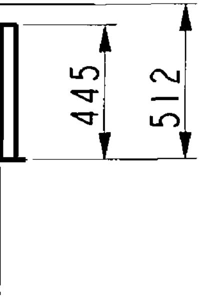

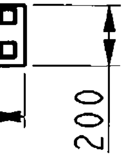

School of Mechanical and
Manufacturing Engineering

Name: Pierce Kennedy	Date: 5 April 2004
Part: Main Frame	Notes: All 50mm ☐ tubing. All dimensions in mm
Scale: 0.04	
Quantity: 1	

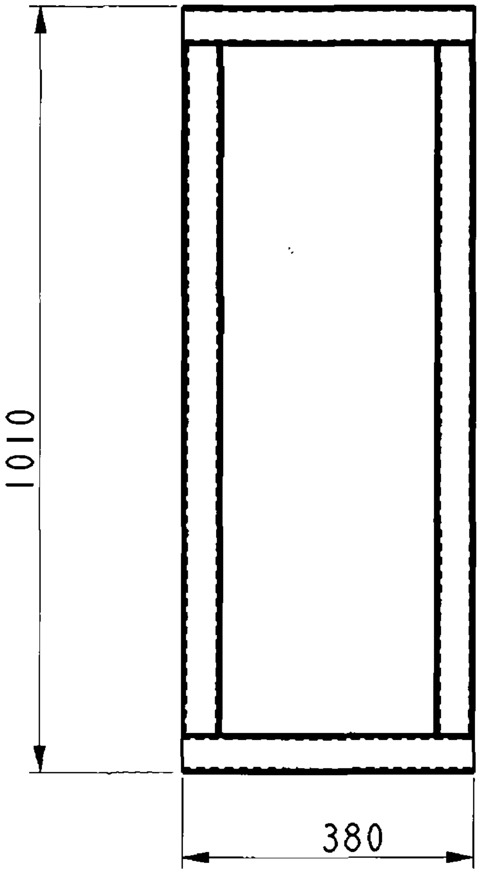
1010
380

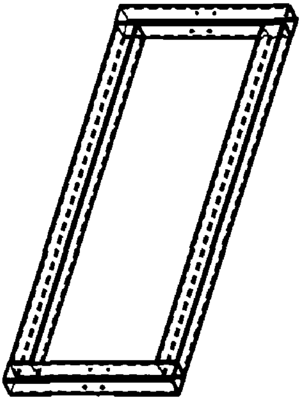

School of Mechanical and Manufacturing Engineering	
Name: Pierce Kennedy	Date: 9 March 2004
Part: Slide Frame	Notes: All tubing 50mm □ All dimensions in mm
Scale: 0.1	
Quantity: 1	

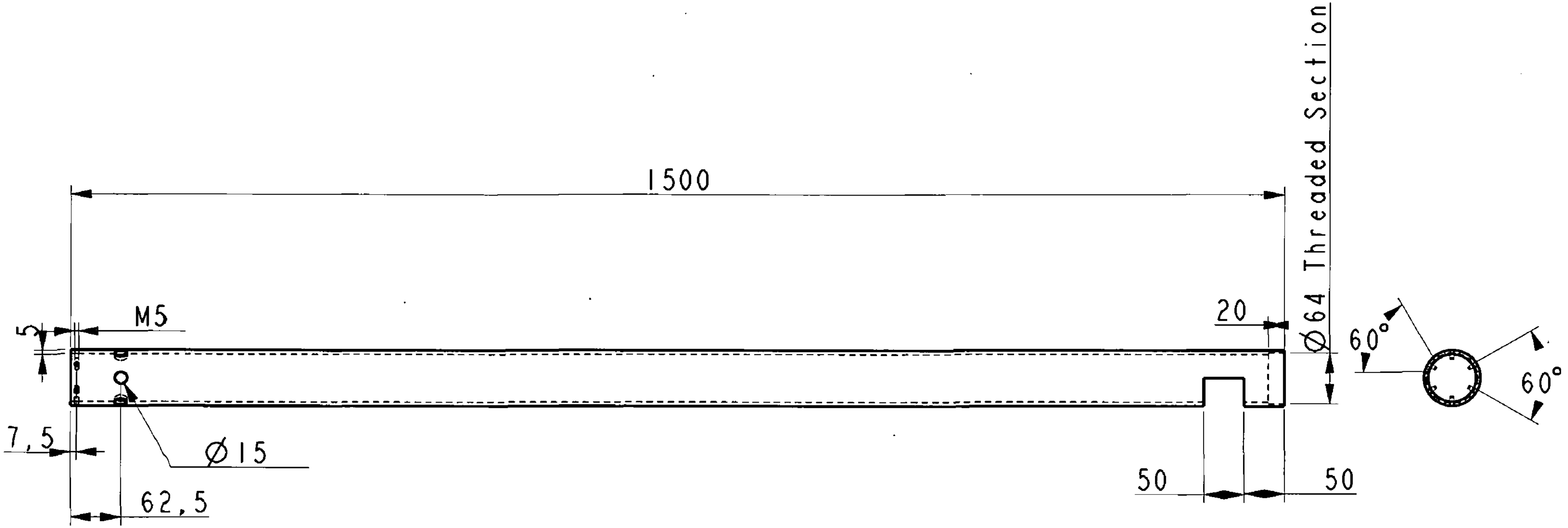

School of Mechanical and Manufacturing Engineering

Name: Pierce Kennedy

Date: 23 March 2004

Part: Barrel

Notes: All dimensions in mm

Scale: 0.04

Quantity: 1

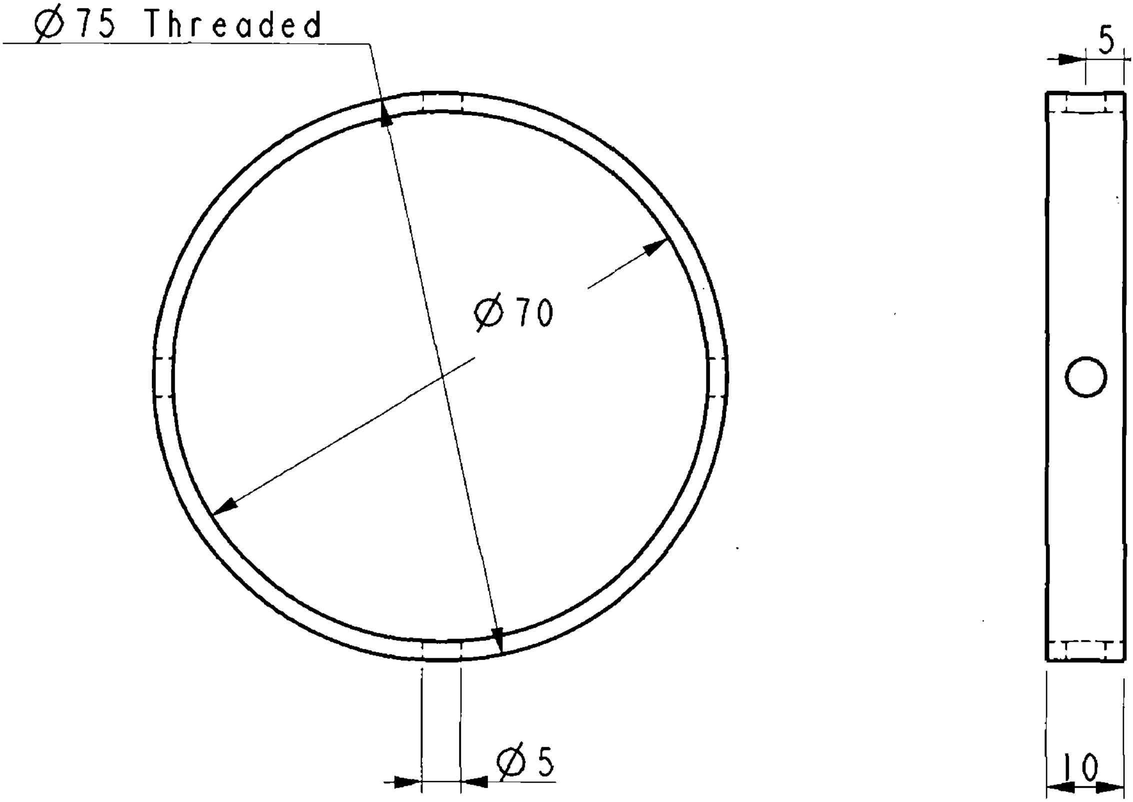
Ø75 Threaded
Ø70
Ø5
5
10

School of Mechanical and Manufacturing Engineering	
Name: Pierce Kennedy	Date: 23 March 2004
Part: Sleeve Fix	Notes: All Holes the same. All dimensions in mm
Scale: 1	
Quantity: 1	

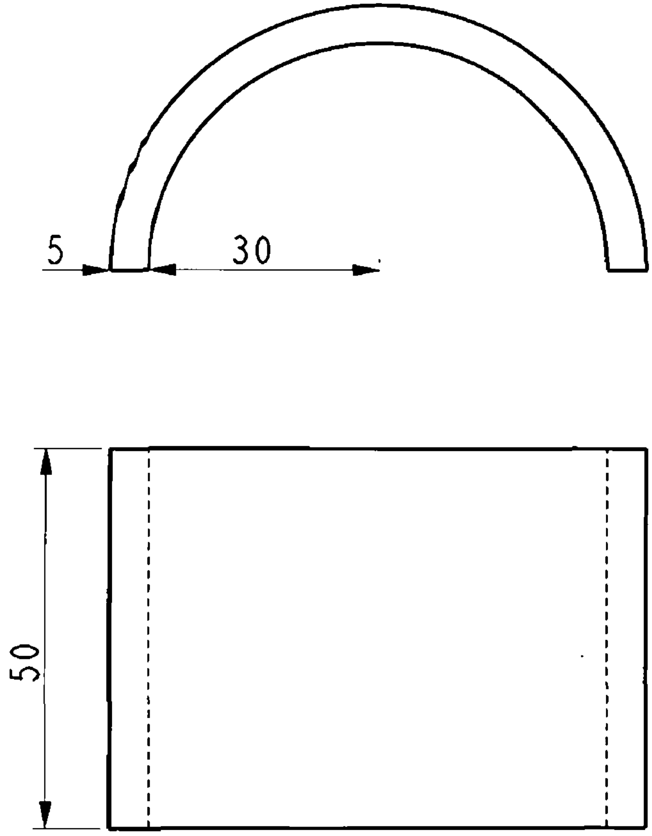
5
30
50

School of Mechanical and
Manufacturing Engineering

Name: Pierce Kennedy
Date: 23 March 2004
Part: Barrel Ope Cover
Notes: Both Holes the same. All dimensions in mm
Scale: 1
Quantity: 1

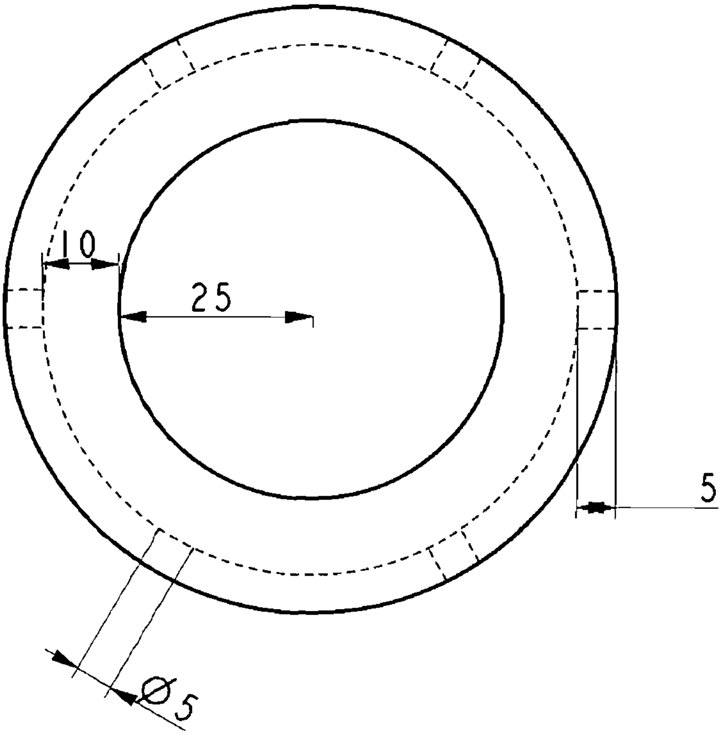
10
25
5
Ø5

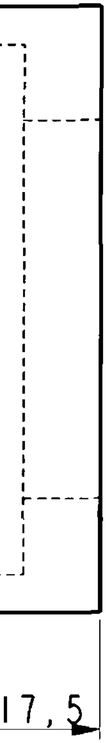

School of Mechanical and
Manufacturing Engineering

Name: Pierce Kennedy	Date: 15 March 2004
Part: Sabot Stop	Notes: All Holes the same. All dimensions in mm
Scale: 1	
Quantity: 1	

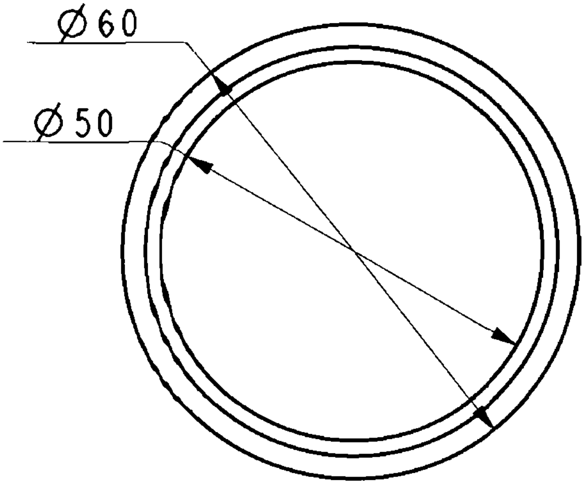
Ø60
Ø50

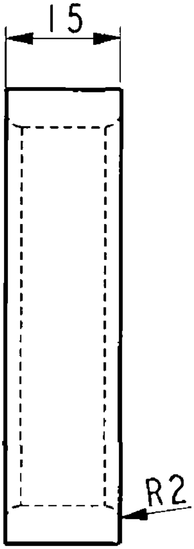

School of Mechanical and Manufacturing Engineering	
Name: Pierce Kennedy	Date: 9 March 2004
Part: Rubber Stop	Notes: All dimensions in mm Material: Rubber
Scale: 1	
Quantity: 1	

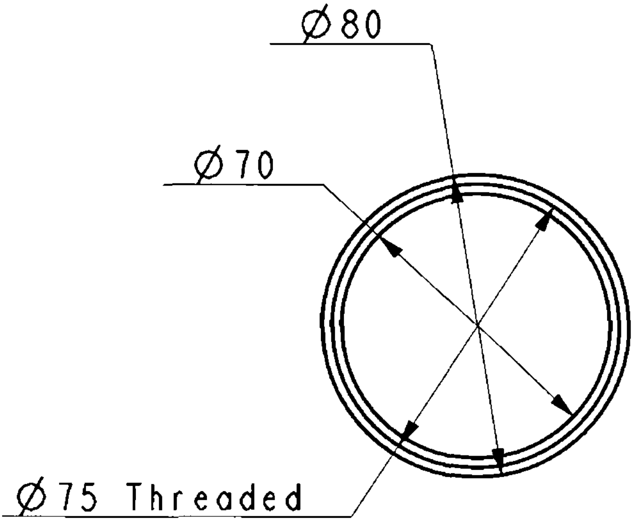
Ø80
Ø70
Ø75 Threaded

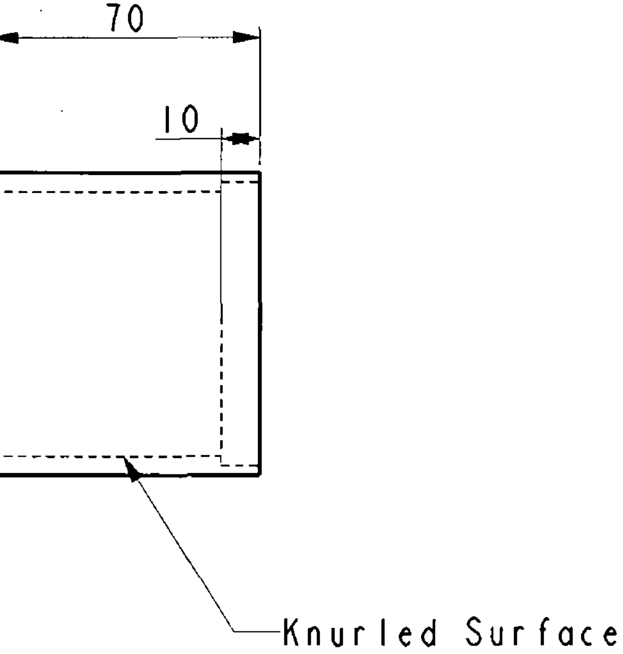

School of Mechanical and Manufacturing Engineering	
Name: Pierce Kennedy	Date: 23 March 2004
Part: Barrel Sleeve	Notes: All dimensions in mm
Scale: 0.5	
Quantity: 1	

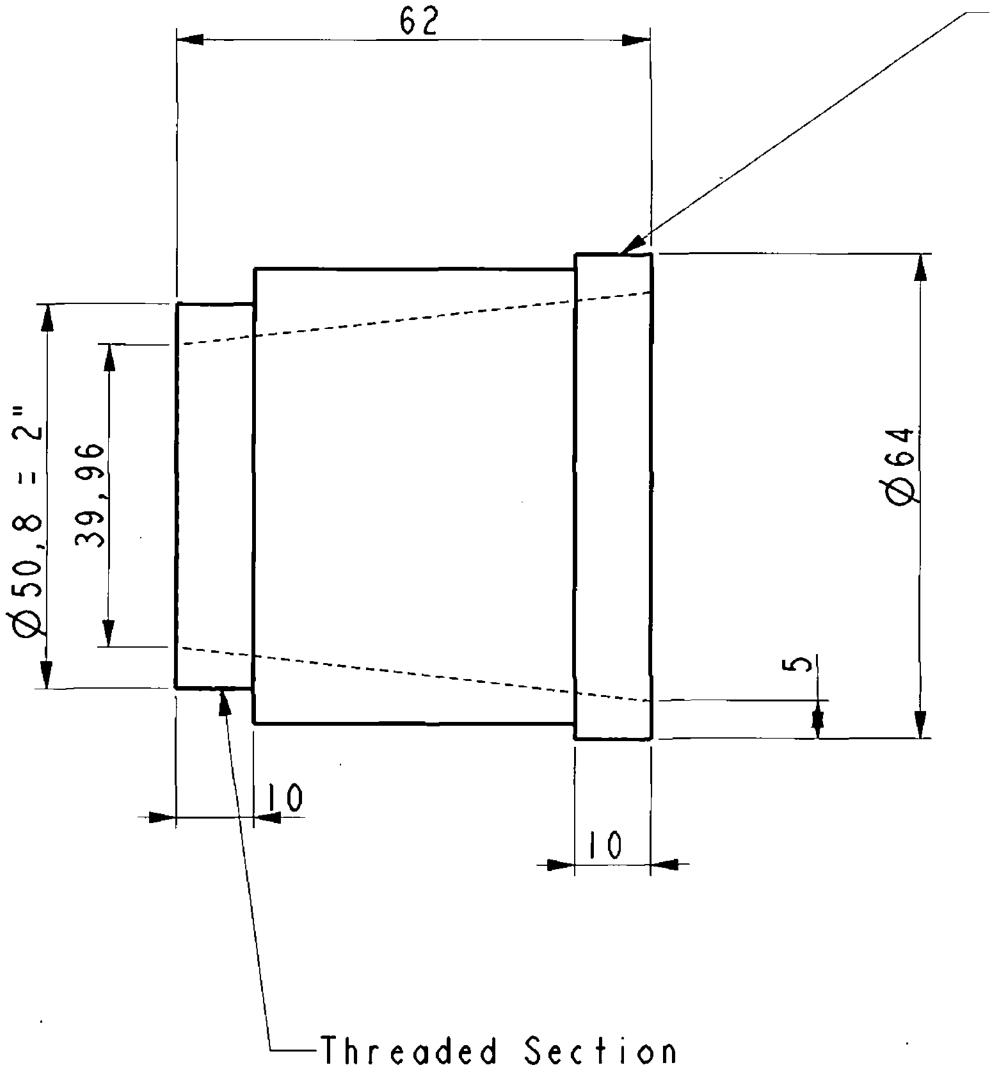
62
Ø50,8 = 2"
39,96
Ø64
5
10
10
Threaded Section

Threaded Section

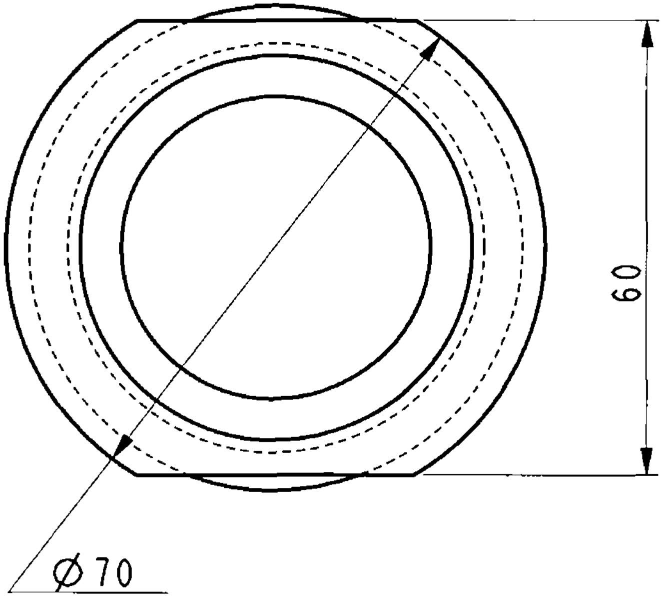

School of Mechanical and Manufacturing Engineering	
Name: Pierce Kennedy	Date: 23 March 2004
Part: Connector	Notes: All dimensions in mm
Scale: 1	
Quantity: 1	

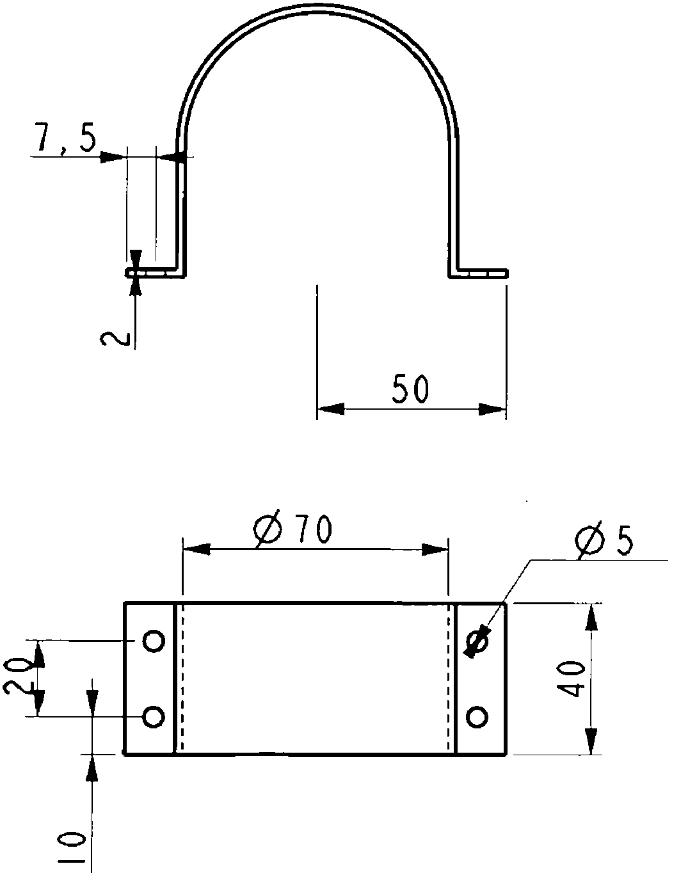
7,5
2
50
Ø70
Ø5
20
40
10

School of Mechanical and Manufacturing Engineering	
Name: Pierce Kennedy	Date: 09 March 2004
Part: Barrel Clamp	Notes: All dimensions in mm
Scale: 0.5	
Quantity: 3	

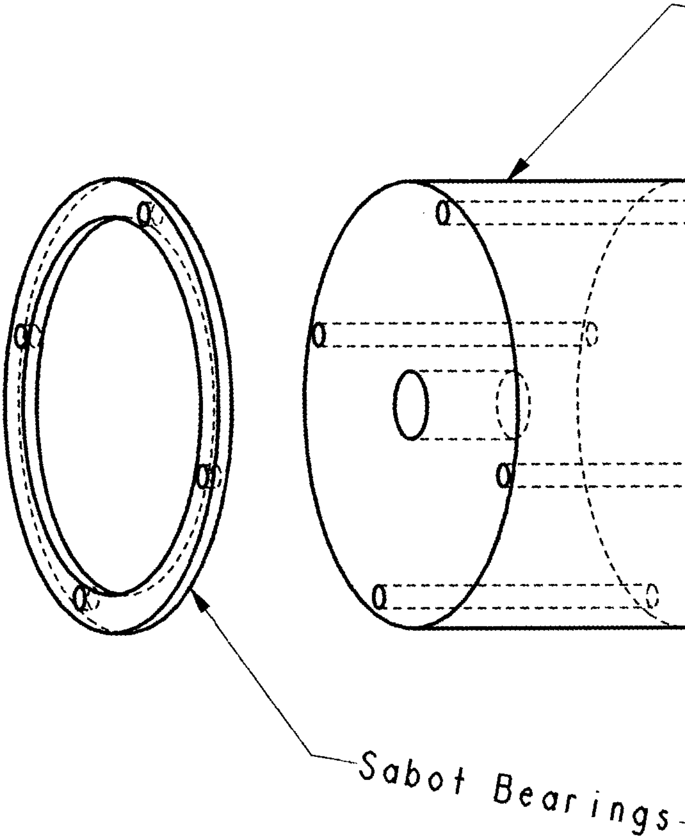
Sabot Bearings

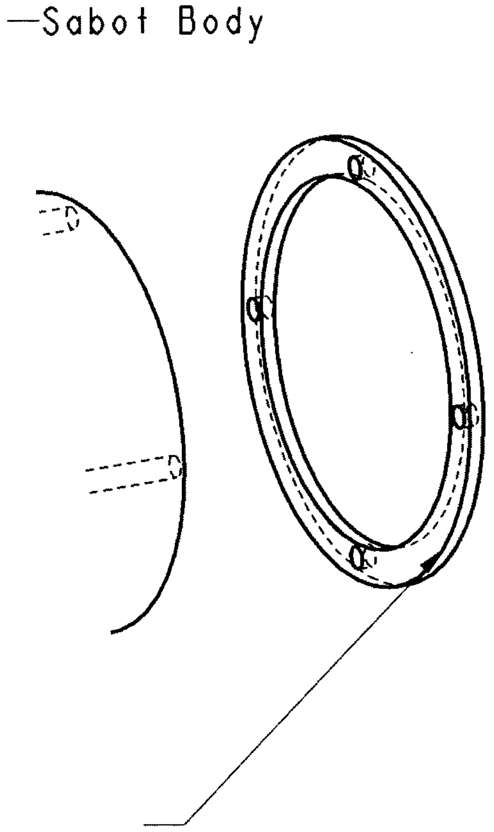

School of Mechanical and Manufacturing Engineering	
Name: Pierce Kennedy	Date: 15 March 2004
Part: Sabot Assembly	Notes:
Scale: 1	
Quantity: 1	

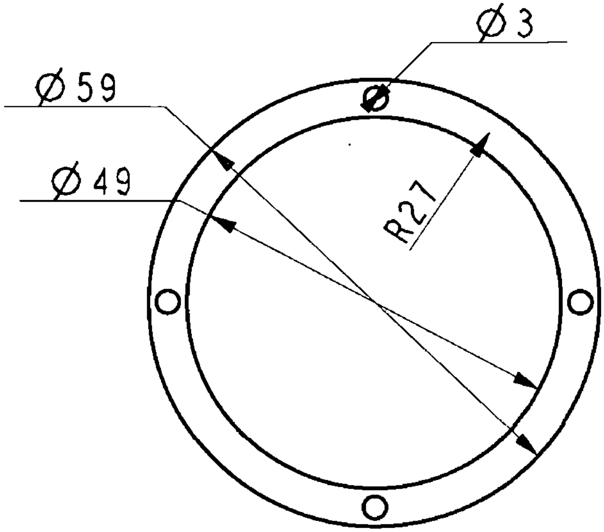
Ø3
Ø59
Ø49
R27

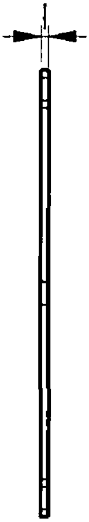

School of Mechanical and Manufacturing Engineering	
Name: Pierce Kennedy	Date: 9 March 2004
Part: Sabot Front Plate	Notes: All Holes the same. All dimensions in mm
Scale: 1	
Quantity: 1	

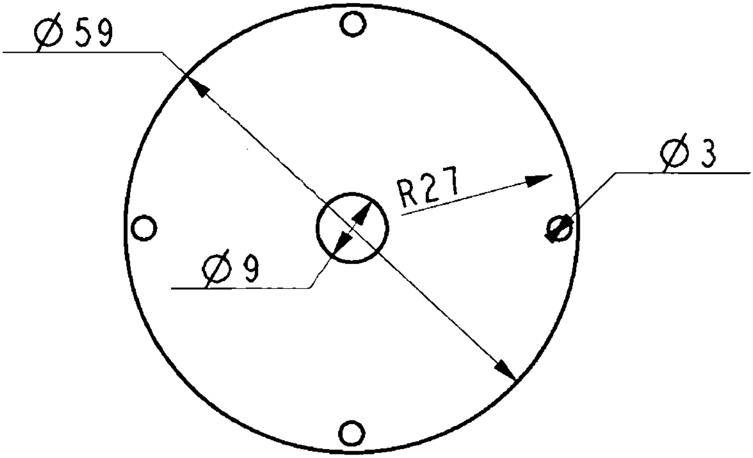
Ø59
R27
Ø3
Ø9

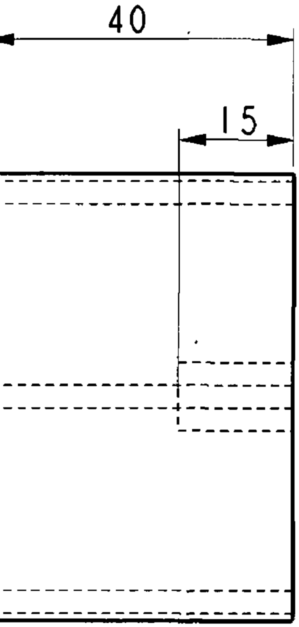

School of Mechanical and
Manufacturing Engineering

Name: Pierce Kennedy	Date: 9 March 2004
Part: Sabot Body	Notes: All Holes the same. All dimensions in mm Material: Rubber
Scale: 1	
Quantity: 1	

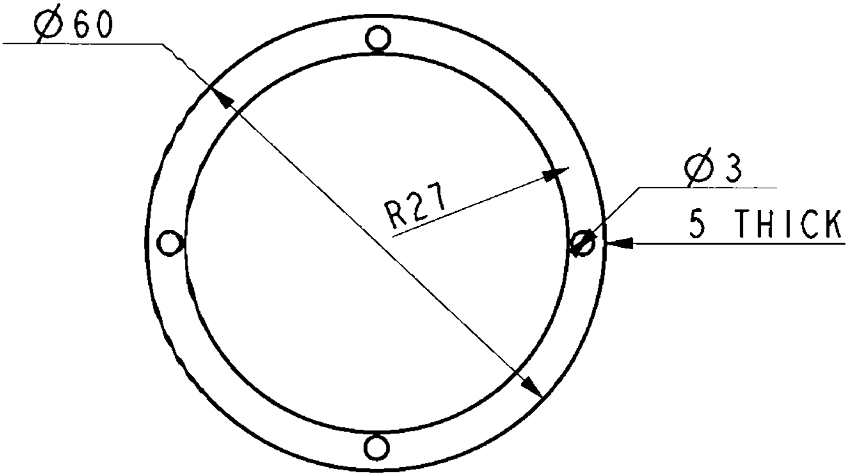
Ø60
R27
Ø3
5 THICK

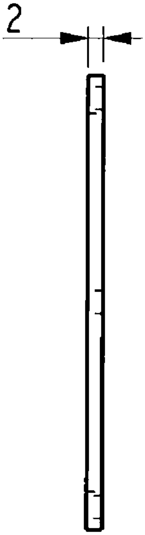

School of Mechanical and Manufacturing Engineering	
Name: Pierce Kennedy	Date: 9 March 2004
Part: Sabot slides	Notes: All Holes the same. All dimensions in mm. Material: Teflon
Scale: 1	
Quantity: 2	

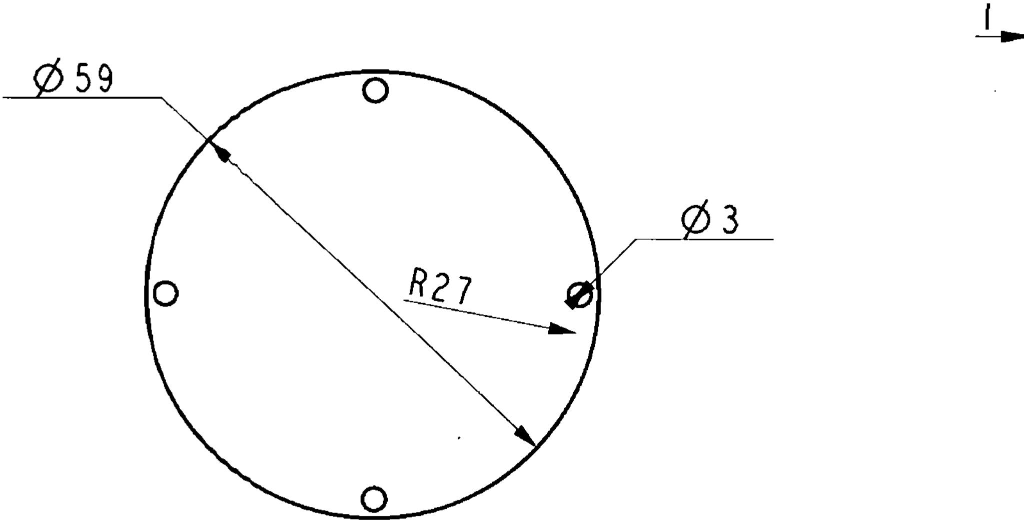
Ø59
Ø3
R27
I

School of Mechanical and Manufacturing Engineering	
Name: Pierce Kennedy	Date: 9 March 2004
Part: Sabot Back Plate	Notes: All Holes the same. All dimensions in mm
Scale: 1	
Quantity: 1	

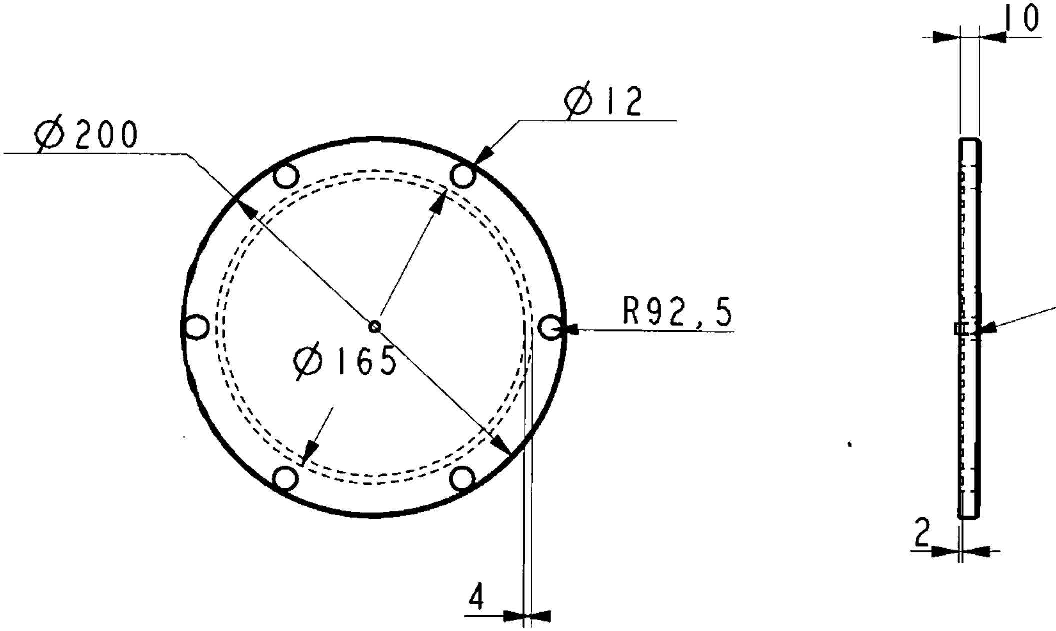

Ø200
Ø12
R92,5
Ø165
4
10
2

School of Mechanical and Manufacturing Engineering	
Name: Pierce Kennedy	Date: 15 March 2004
Part: Reservoir Endplate (2)	Notes: All Holes the same unless stated. All dimensions in mm
Scale: 0.25	
Quantity: 1	

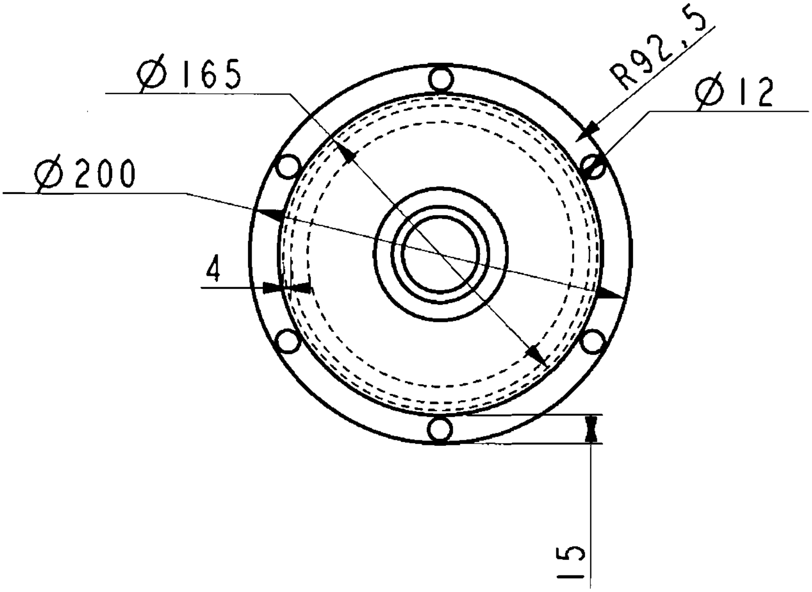
Ø165
R92,5
Ø12
Ø200
4
15

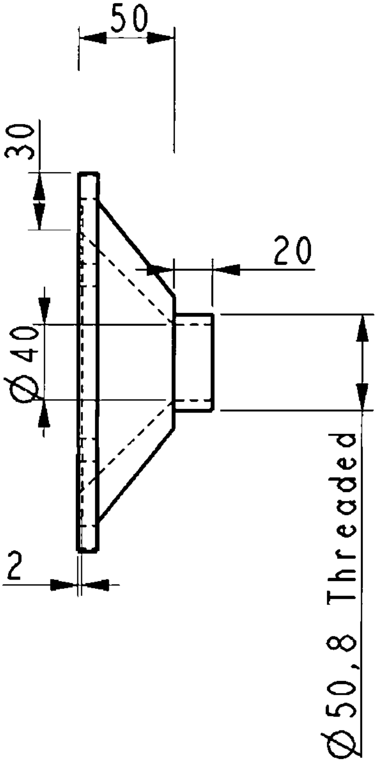

School of Mechanical and Manufacturing Engineering	
Name: Pierce Kennedy	Date: 23 March 2004
Part: Reservoir Endplate (1)	Notes: All Holes the same. All dimensions in mm
Scale: 0.25	
Quantity: 1	

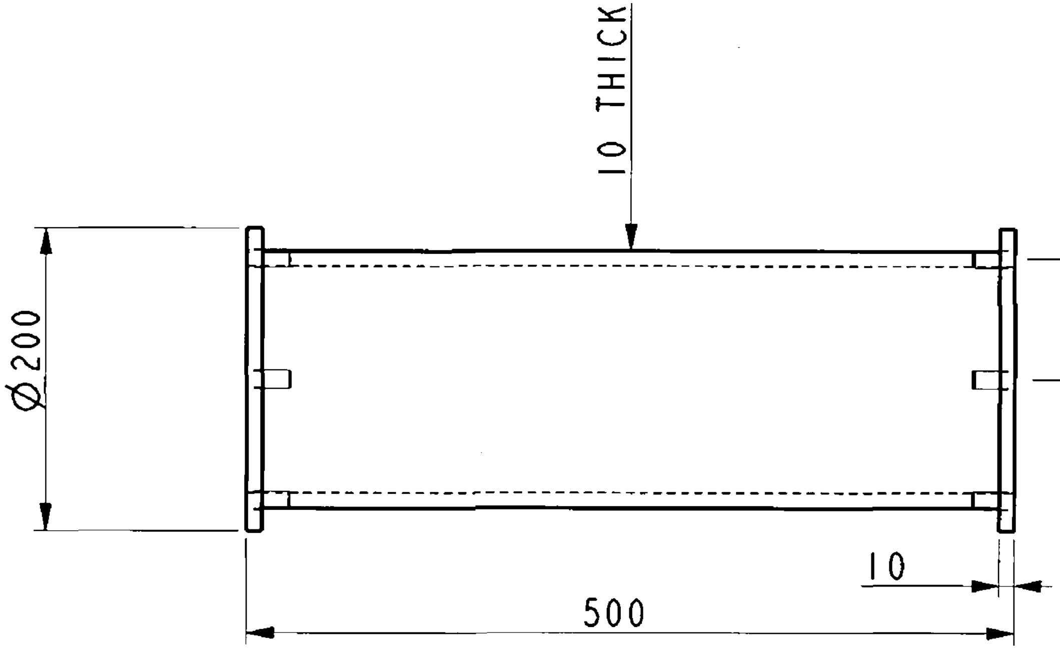
10 THICK
Ø200
10
500

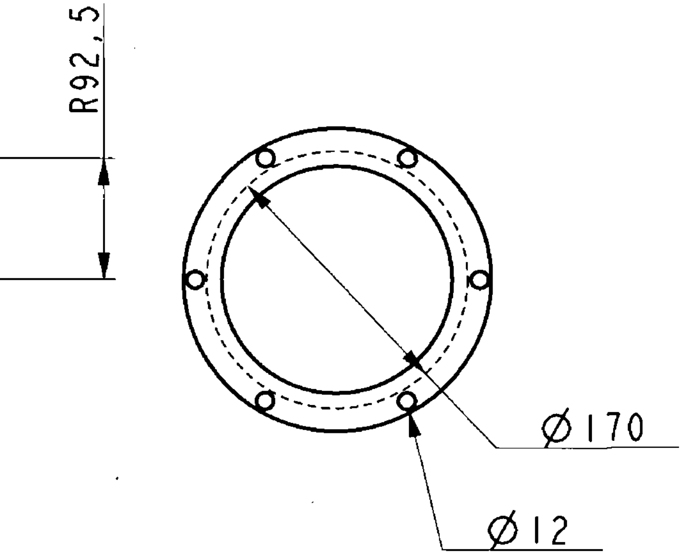

School of Mechanical and Manufacturing Engineering	
Name: Pierce Kennedy	Date: 15 March 2004
Part: Reservoir Body	Notes: All holes the same. All dimensions in mm
Scale: 0.2	
Quantity: 1	

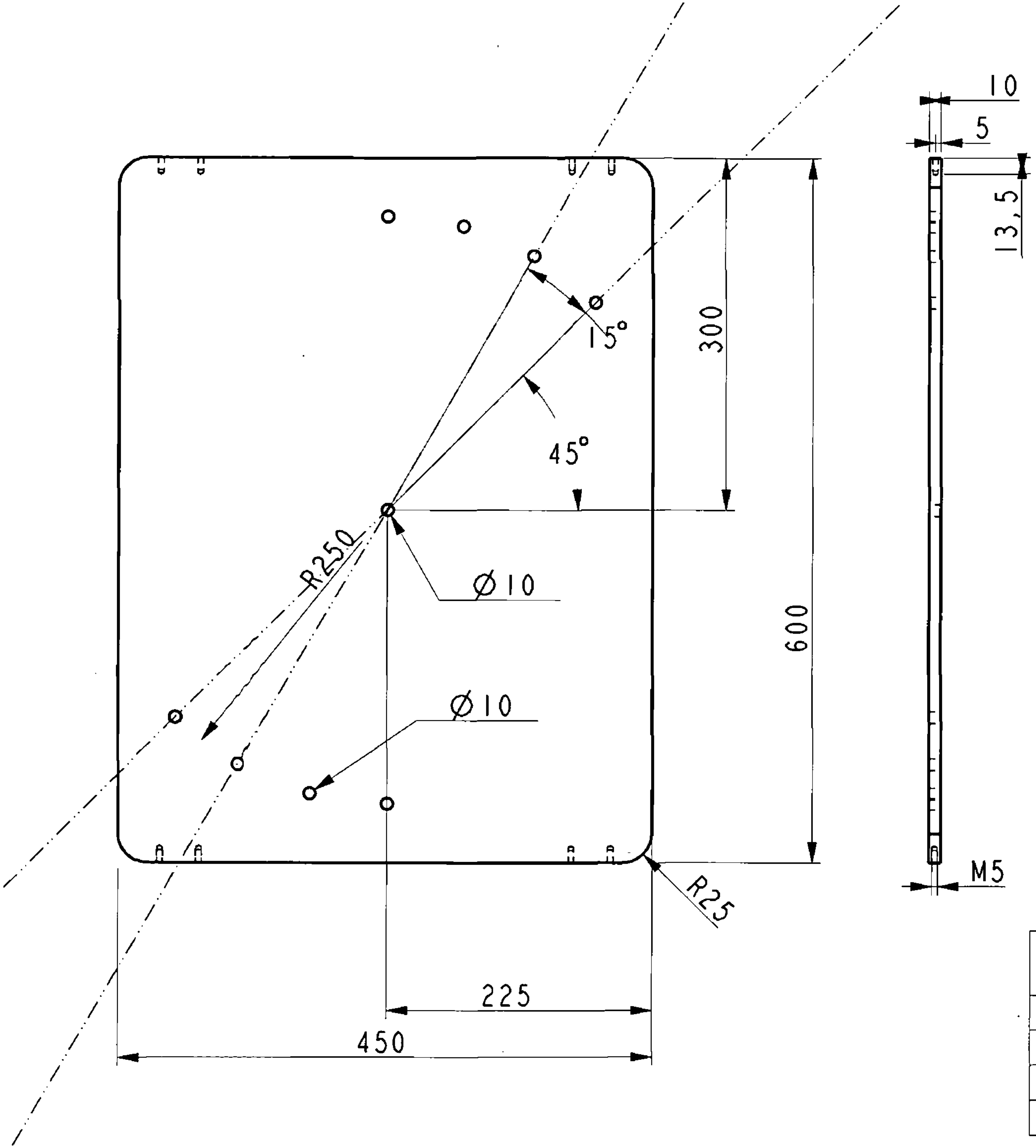

School of Mechanical and Manufacturing Engineering	
Name: Pierce Kennedy	Date: 9 March 2004
Part: Clamp Support	Notes: All holes the same unless specified All dimensions in mm
Scale: 0.2	
Quantity: 2	

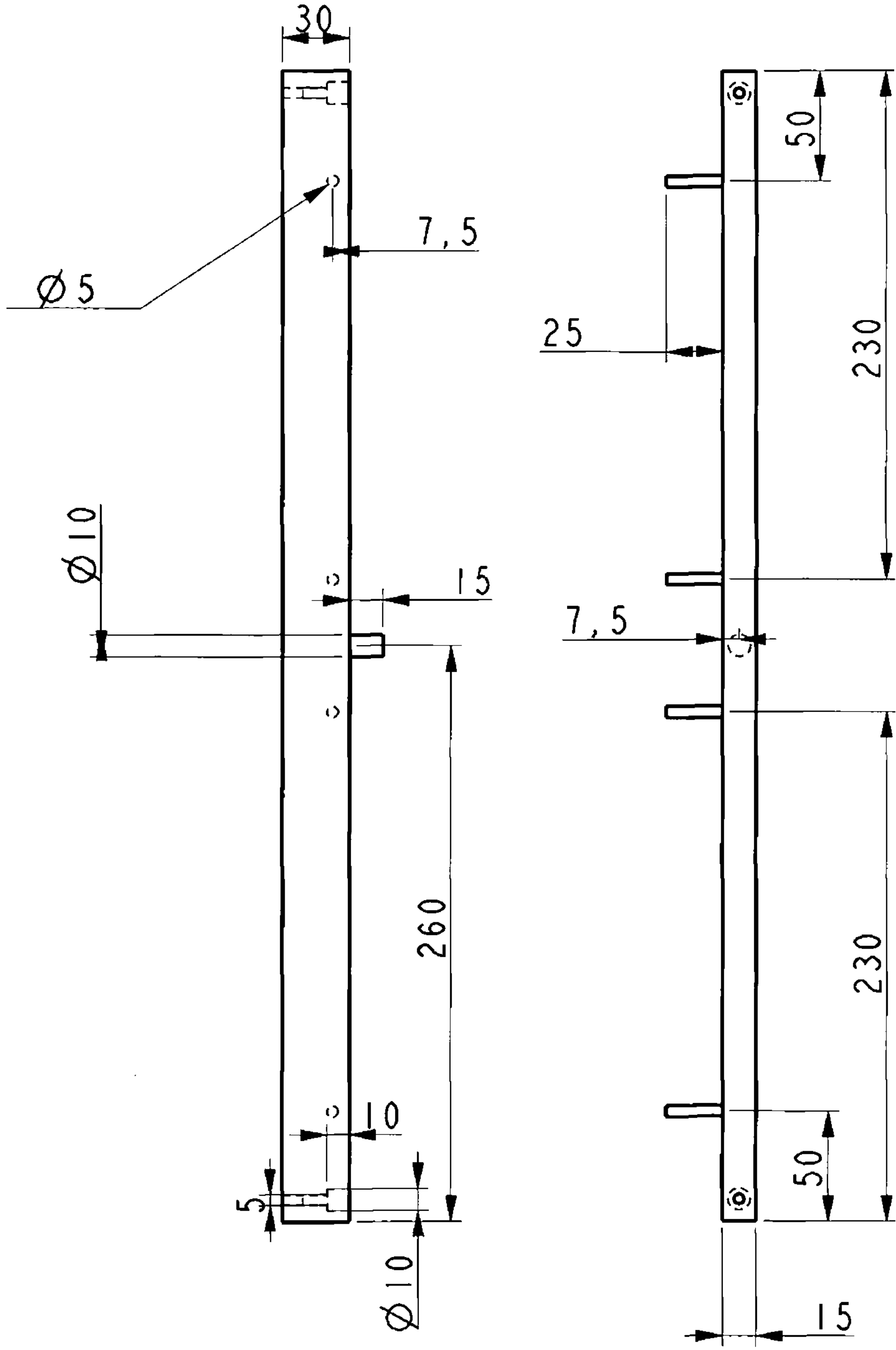
30
7,5
Ø5
Ø10
15
260
10
5
Ø10
50
25
230
7,5
230
50
15

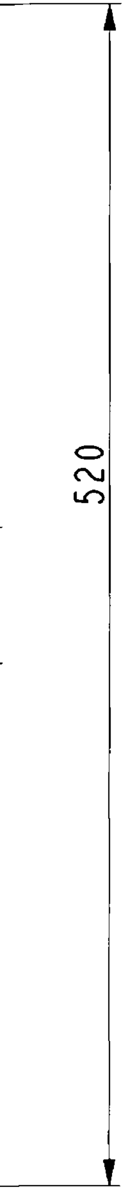

School of Mechanical and
Manufacturing Engineering

Name: Pierce Kennedy	Date: 9 March 2004
Part: Bottom Clamp (1)	Notes: Both Holes the same. All dimensions in mm
Scale: 0.3	
Quantity: 2	

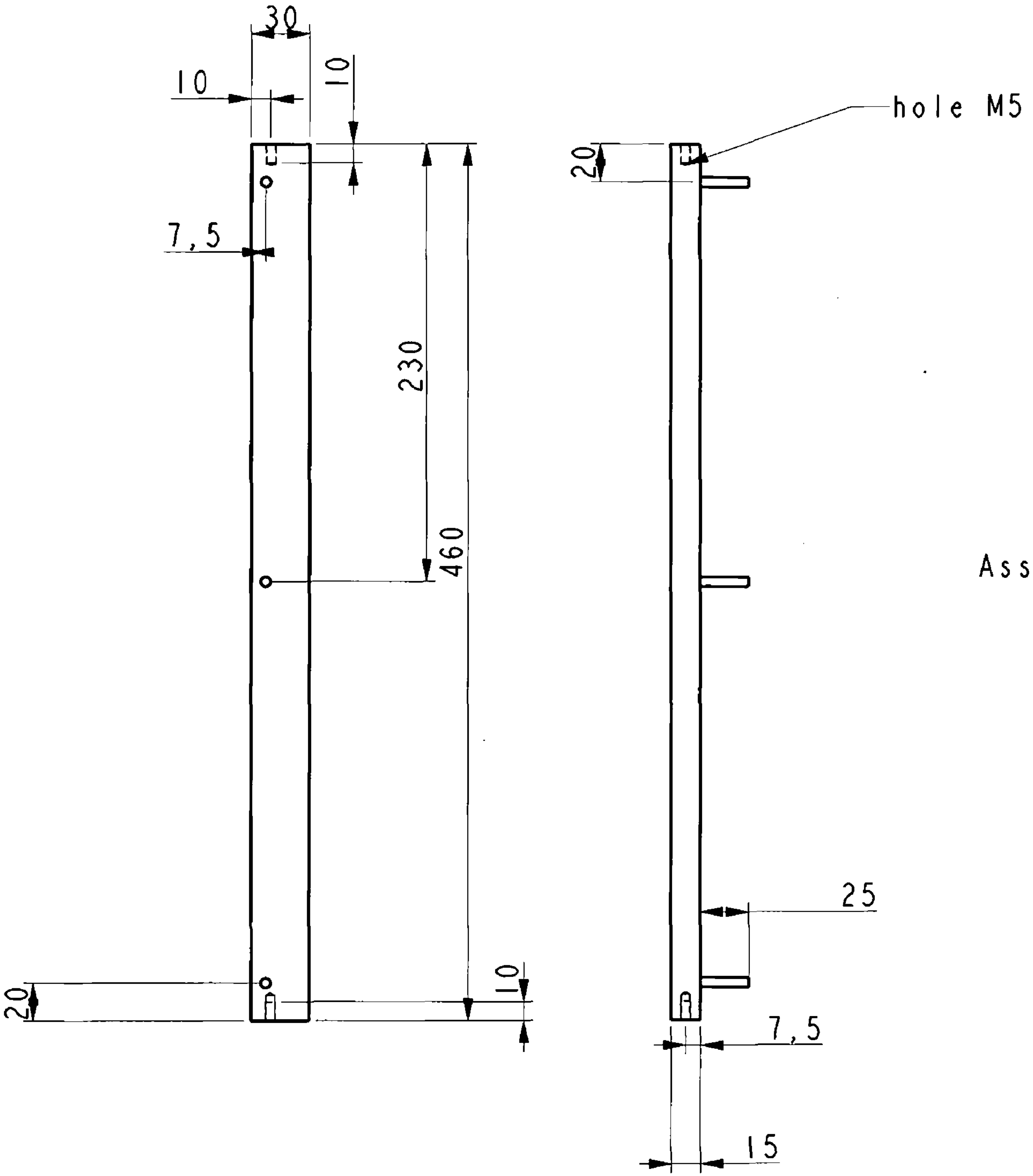

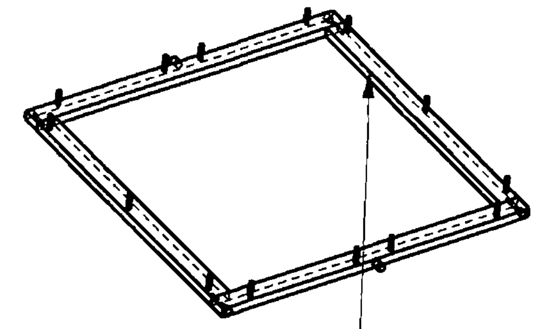

School of Mechanical and Manufacturing Engineering	
Name: Pierce Kennedy	Date: 9 March 2004
Part: Bottom Clamp (2)	Notes: Both Holes the same. All dimensions in mm
Scale: 0.3	
Quantity: 2	

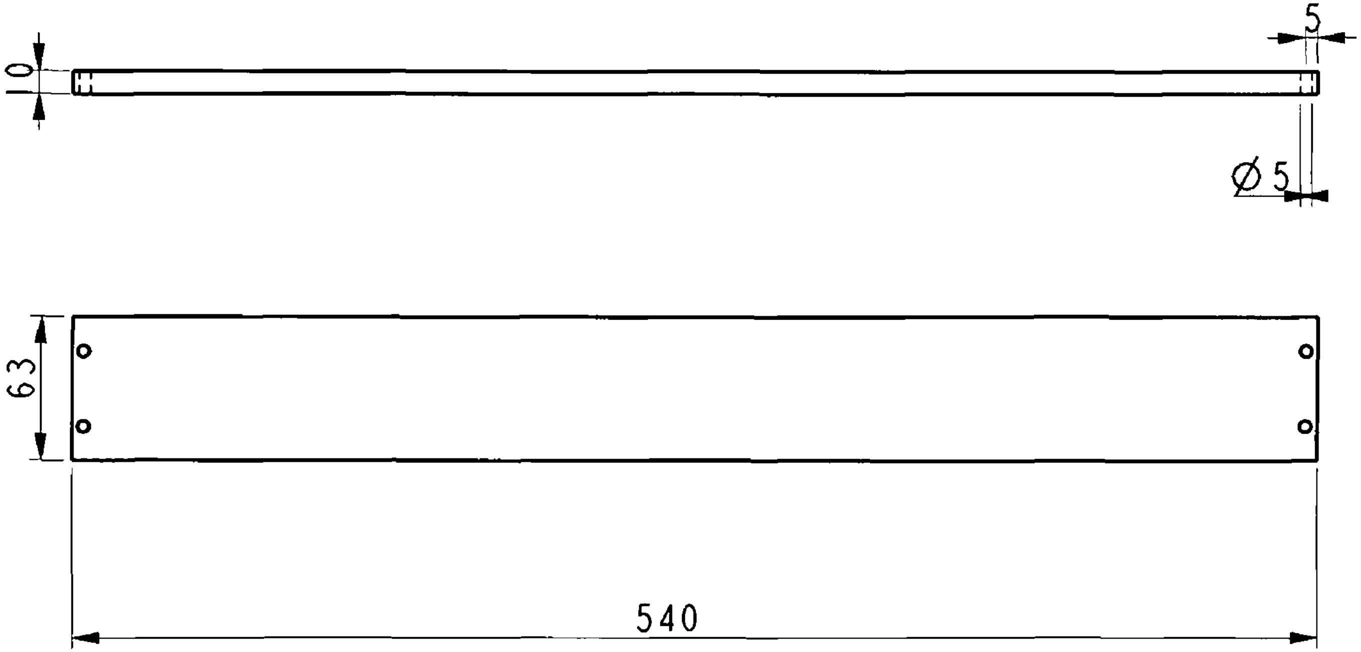

School of Mechanical and
Manufacturing Engineering

Name: Pierce Kennedy	Date: 15 March 2004
Part: Support Strut	Notes: AllHoles the same. All dimensions in mm
Scale: 0.3	
Quantity: 2	

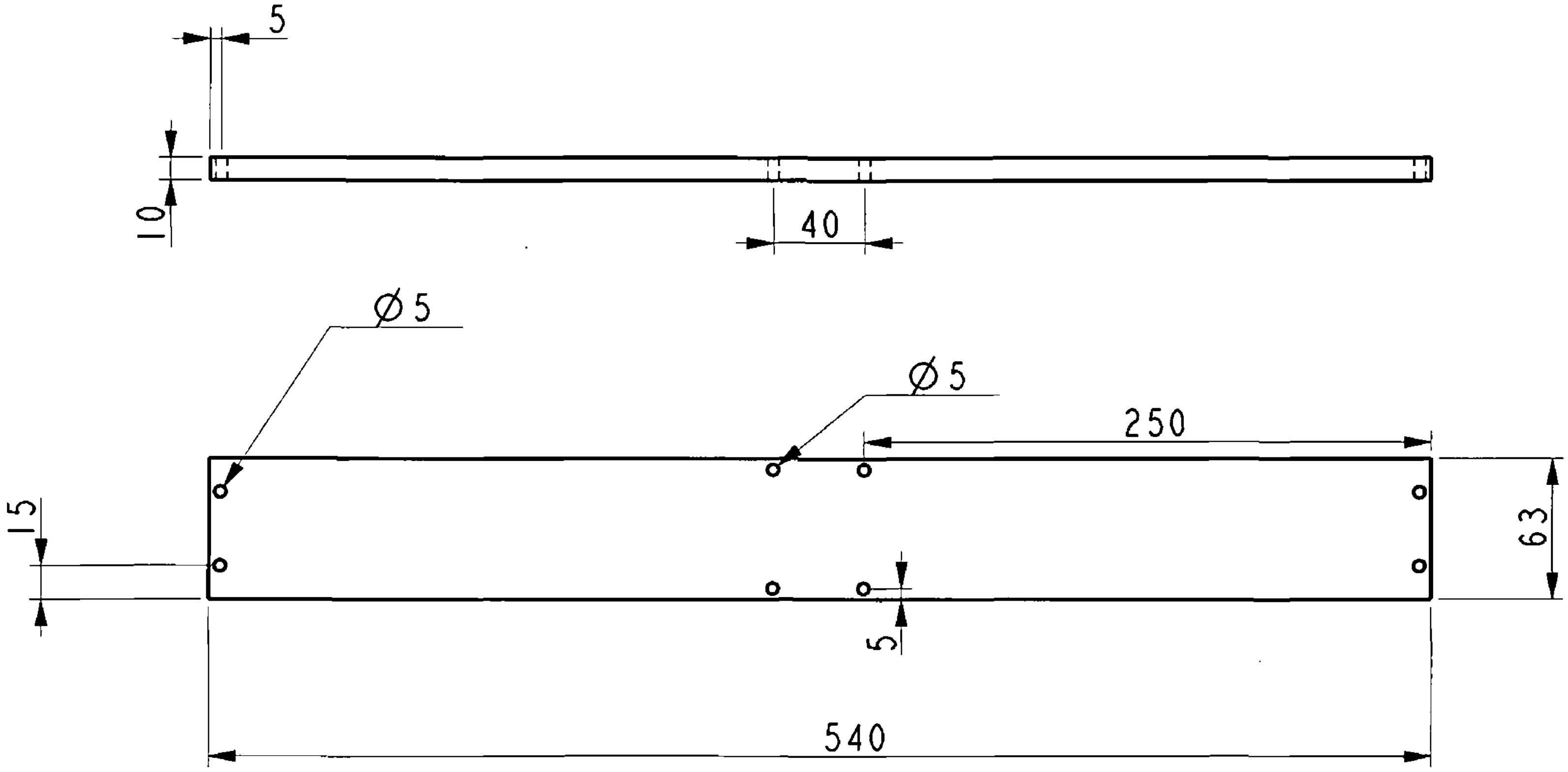

School of Mechanical and
Manufacturing Engineering

Name: Pierce Kennedy	Date: 15 March 2004
Part: Carriage Plate (1)	Notes: All dimensions in mm
Scale: 0.3	
Quantity: 2	

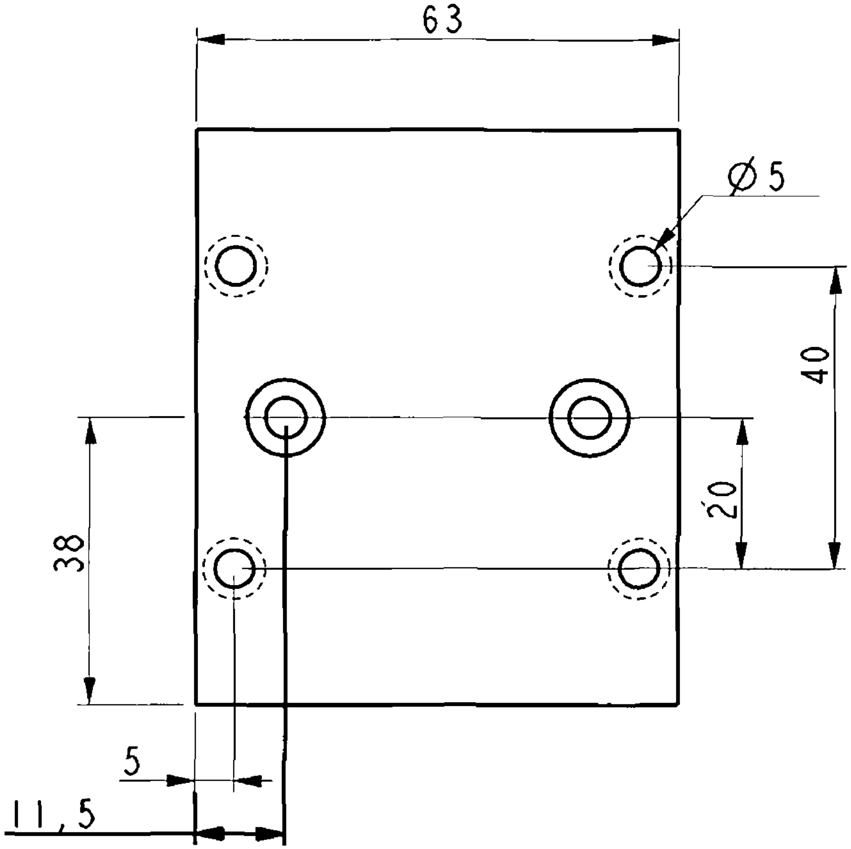
63
∅5
40
20
38
5
11,5

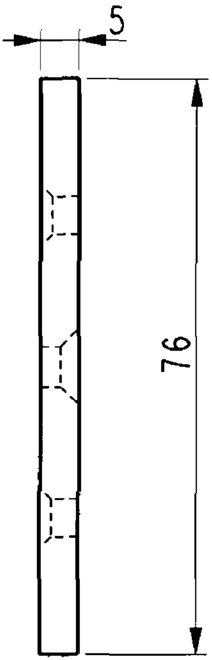

School of Mechanical and Manufacturing Engineering	
Name: Pierce Kennedy	Date: 9 March 2004
Part: Carriage Plate (2)	Notes: All dimensions in mm
Scale: 1	
Quantity: 2	

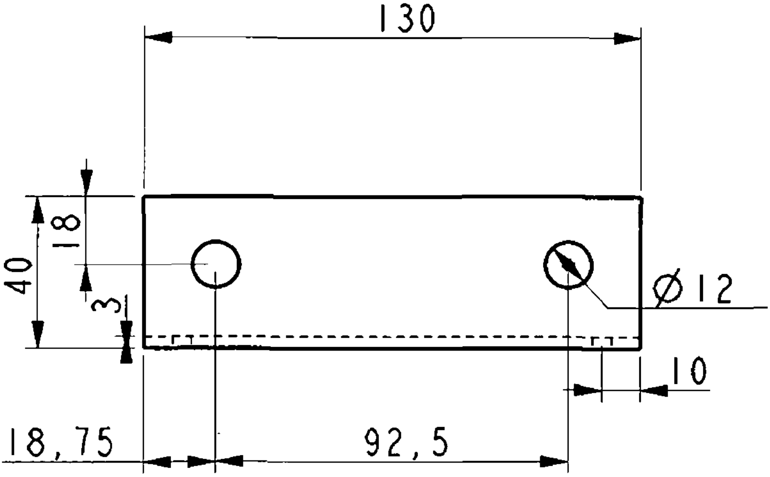
130
18
40
3
Ø12
10
18,75
92,5

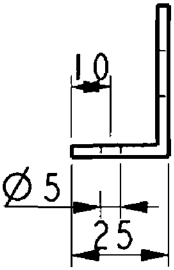

School of Mechanical and Manufacturing Engineering	
Name: Pierce Kennedy	Date: 15 March 2004
Part: Reservoir Bracket	Notes: All dimensions in mm
Scale: 0.5	
Quantity: 1	

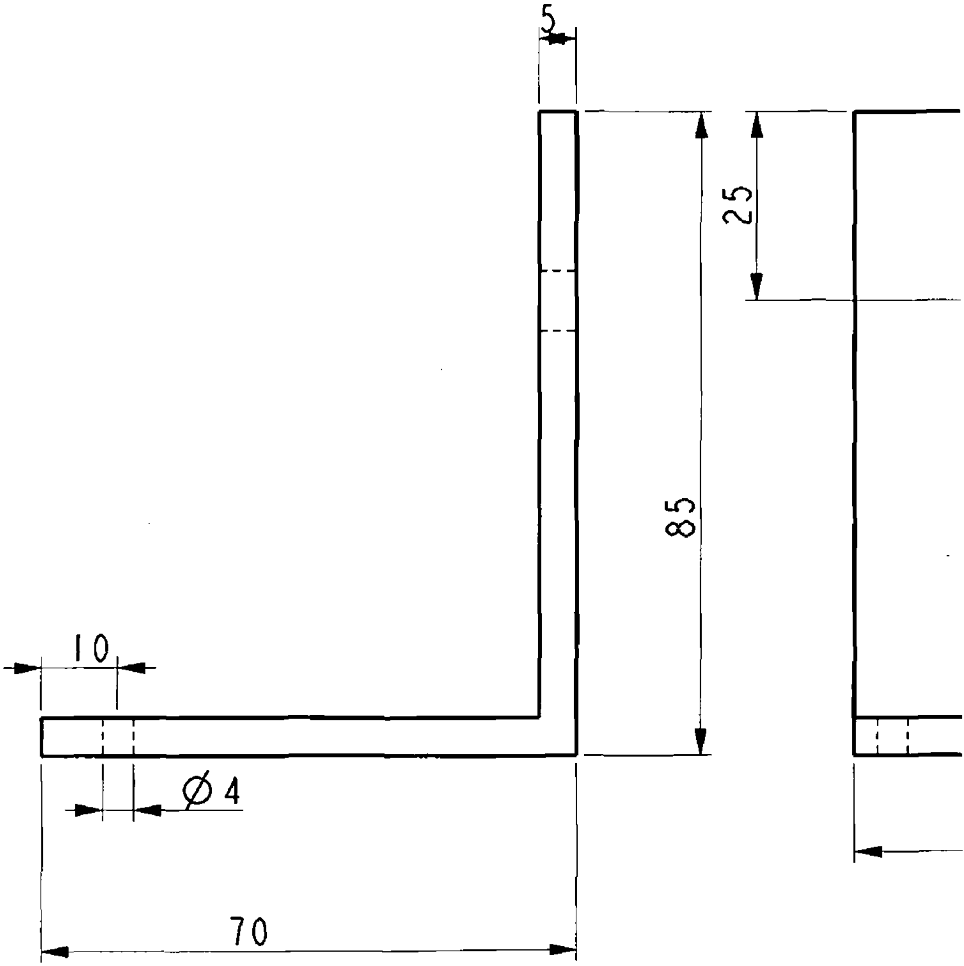
5
25
85
10
Ø 4
70

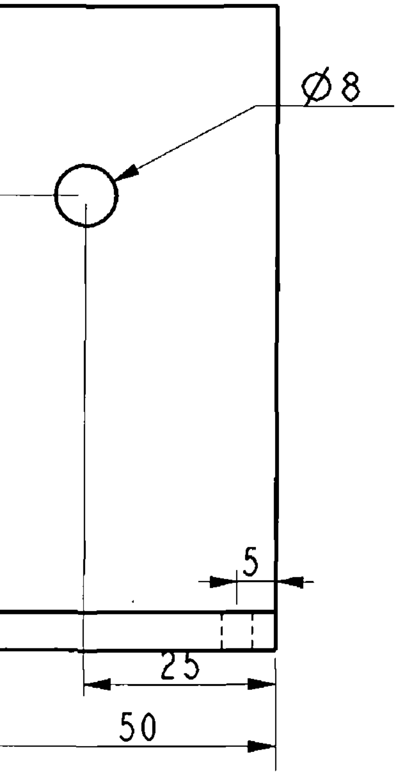

School of Mechanical and Manufacturing Engineering	
Name: Pierce Kennedy	Date: 5 April 2004
Part: Bottom Clamp (1)	Notes: Both Holes the same. All dimensions in mm
Scale: 1	
Quantity: 2	

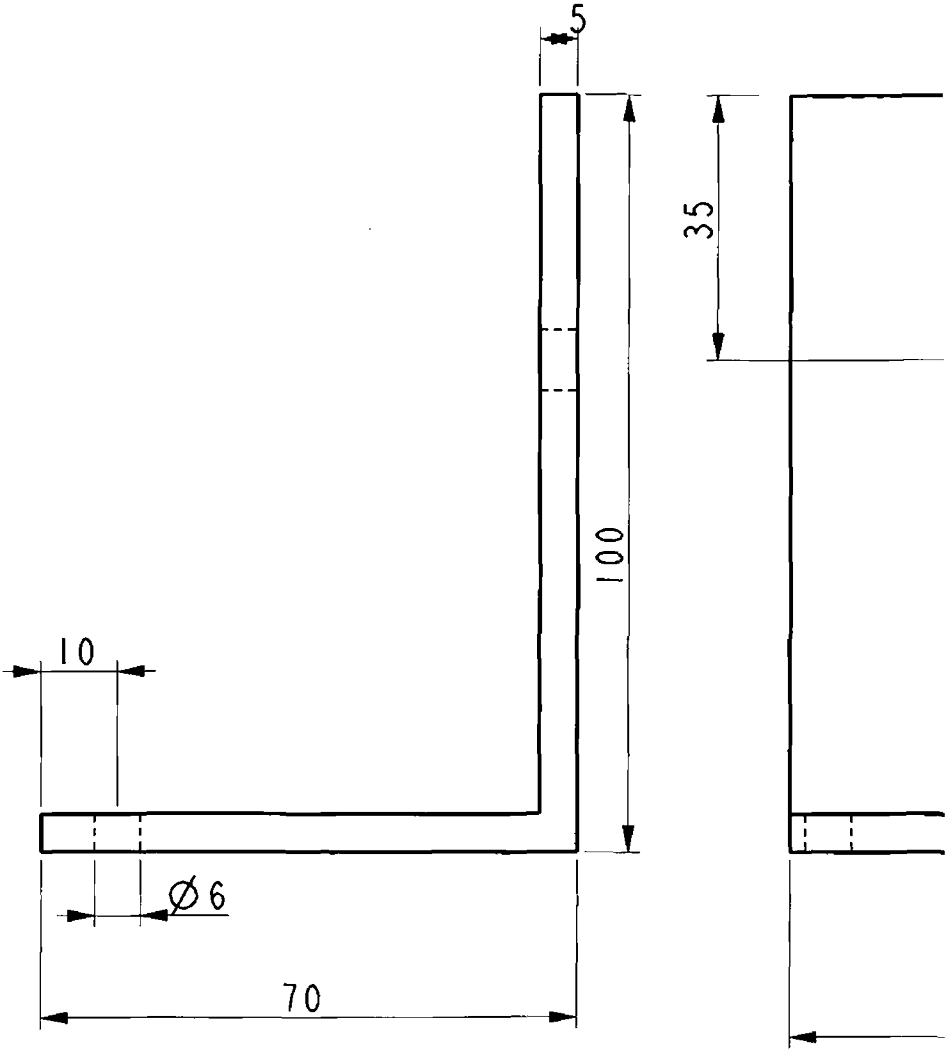
5
35
100
10
Ø6
70

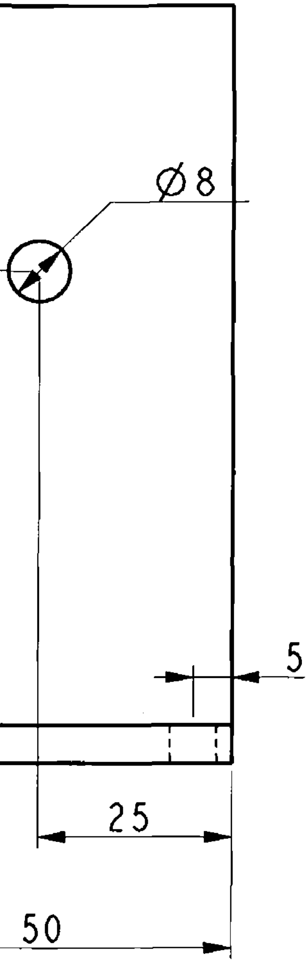

School of Mechanical and Manufacturing Engineering	
Name: Pierce Kennedy	Date: 9 March 2004
Part: Mag Clamp Bracket(1)	Notes: All dimensions in mm
Scale: 1	
Quantity: 2	